DOCTOR OF PHILOSOPHY

Photonic Tweezers for Optical Manipulation of Cells and Tissues

Ferro, Valentina

Award date:
2019

PHOTONIC TWEEZERS FOR OPTICAL MANIPULATION OF CELLS AND TISSUES

VALENTINA FERRO

2019

Dr. David McGloin

School of Science and Engineering

Division of Physics

Prof. Cornelius Weijer

School of Life Sciences

Division of Cell and Developmental Biology

A Thesis Submitted to University of Dundee, in Fulfilment of the Requirements for the Degree of Doctor of Philosophy (Ph.D.)

“If I had a world of my own,
everything would be
nonsense”

— Lewis Carroll,
Alice’s Adventures in Wonderland

ABSTRACT

Optical tweezers represent a powerful tool for studying forces in biological samples. In this thesis, I explored applications of optical tweezers that pushed the technique beyond its limitations. In fact I worked on extending the range of forces applicable by the tweezers and on applying optical tweezers for the study of cell-cell junctions in tissues.

Typical values for optical tweezers forces range between tenths to hundreds of pN, with only few examples of tweezers reaching nN forces. I synthesised photonically structured probes and obtained tweezers capable of nN forces. Furthermore, I optimised the probes to make them more suitable for biological experiments, I investigated alternative synthesis methods and conducted proof-of-concept studies for their application in cellular biology.

Regarding the application of tweezers in tissues, I demonstrated their use for the study of tension in developing chick embryos. At about 6h from the egg's deposition, the chick embryo initiates gastrulation: the embryo rearranges from a single layered structure into a multi-layered one. The process is regulated by the large-scale highly coordinated flows of the cells in the epiblast. There are evidences that contraction and preferential cells intercalation in the posterior area of the embryo drive the process. The contraction in the posterior area seems to be correlated with the presence of myosin II cables.

I optically manipulated cell-cell junctions in chick embryos while recording their deformation. I measured the difference response of junctions studied under different conditions. The results support the idea that junctions in the posterior area of embryos starting gastrulation (5h old) are under stronger tensions than junctions in younger embryo and junctions in the anterior area of the organism. Moreover, when embryos are treated with myosin I or myosin II inhibitors, tension in the junctions is reduced.

CONTENTS

LIST OF FIGURES

LIST OF TABLES

GLOSSARY

ACRONYMS

AFM atomic force microscopy

STM scanning tunnelling microscopy

SEM scanning electron microscopy

DNA deoxyribonucleic acid

QPD quadrant photodiodes

PSD power spectrum density

SiO_2 silicon dioxide

TiO_2 titanium dioxide

χTiO_2 anatase titanium dioxide, or crystalline titania

αTiO_2 nanoporous titanium dioxide, or amorphous titania

TBT titanium(IV) butoxide $Ti(OBu)_4$

$HOCH_2CH_2OH$ ethylene glycol

$Ti(OCH_2CH_2OH)_2$ titanium glycolate

$HOBu$ butyl alcohol

TTIP Titanium tetraisopropoxide

PFA perfluoroalkoxy alkanes

IPA isopropyl alcohol

ODA octadecylamine

PFTE polytetrafluoroethylene

IR infrared

PBS polarising beam splitter

MDCK Madin-Darby canine kidney

rcf round centrifugal force

CTAB cetyltrimethylamoniumbromide

TEOS tetraorthosilicate

ICAM-1 intercellular adhesion molecule 1

LFA-1 lymphocyte function-associated antigen 1

IL2 Interleukin 2

IL12 Interleukin 12

cAMP 3′-5′ cyclic adenosine monophosphate

Ax2 Axenic strain of Dictyostelium Discoideum

KK2 20 mM potassium phosphare buffer (pH = 6.8)

HL5 Axenic buffer

PDMS polydimethylsiloxane

TIR-Ph Total Internal Reflection microscopy with integrated Photonic tweezers

TIRF total internal reflection fluorescence

A/P anterior/posterior

FGF fibroblast growth factor

TGF transforming growth factor

PCP pentachloropseudilin

PBP pentabromopseudilin

FRET Förster resonance energy transfer

GFP green fluorescence protein

EC early chick

HW half wavelength

LED light emitting diode

DAQ data acquisition

FFT finite Fourier transform

SYMBOLS AND UNITS

u	energy of a photon
p	momentum
c	speed of light
h	Plank constant
λ	wavelength
P, P_i, P_r, P_t	power, incident power, reflected power, transmitted power
R	radius
ϑ_i, ϑ_r, ϑ_t	angle of an incident ray, angle of a reflected ray, angle of a transmitted ray
n_i, n_t	refractive index of the medium, refractive index of dielectric object
m	n_t/n_i, effective refractive index
t	time
x, y, z	position, displacement
x_{eq}, y_{eq}, z_{eq}	equilibrium position in the optical tweezers
F_{scat}	scattering force
F_{grad}	gradient force
F,F_x, F_y, F_z	force, force in x-, y-, z- direction
k, k_x, k_y, k_z	trap stiffness, trap stiffness in x-, y-, z- direction
F_{Stokes}	drag force

I, I_0	beam intensity
E	electric field
α	polarisability
k_B	Boltzmann constant
T	absolute temperature
$\mathcal{R}$	Reynolds number
ρ	density of the medium
η	dynamic viscosity
ζ	η/ρ, kinematic viscosity
v, v_e	velocity, escape velocity
γ	drag coefficient
D	$D = \frac{k_B T}{\gamma}$, diffusion coefficient
pN, nN, N	pico-, nano-, Newton
mW, W	milli-, Watt

ACKNOWLEDGEMENTS

I would like to express my sincere gratitude to my advisors Prof. Kees Weijer and Dr. David McGloin. They have been source of inspiration and safe port to reach for help.

I would like to thank Dr. Yuri Belotti, for the microfluidics chips; Dr. Gail Singer, for helping with the Dictyostelium; Dr. Laura Spinelli, for making the T-Cells samples; Dr. Manli Chuai, for providing the chick embryos and making it look easy, although it is not. I would like to thank also Wendy Phillips, whose emails were always welcome.

Thanks to Prof. Erik Schaeffer and everyone in the Nanoscience Research Group at University of Tuebingen. I learnt so much in such little time, thank to all the people that made me feel like family from the first day.

To all the new friends I have made. For all the experience we have enjoyed together, for all the times they have cheered me up and supported me, for all the beers and the coffees together. Thank you all, my *phoquers* friends! Especially Ty, Thomas and Piotr for the help in the lab and the troubleshooting and the hilarious lunch breaks, for the skeptical thinking and for the "mugagement" ring; Valerie for the outreaches and the energy and the penguins, Alessandra for the funny moments and the good food and the unicorns; Daniel for the warmest hugs, Ivo for the laughs and its ability to slow down and put everything in perspective.

A big "Thank you" goes to my terrific friends back in Italy, or around the world, who have never ceased to present in my life and to be supportive. To the "Gulp" girls, Greta, Marzia and Krizia, to Dario and Mico, to Peppe, to Giuseppe, to Giulia and Luca, to Jose', to Aurora, to Sanja, to Vincent, to Dennis! To my dearest Sebi, because the darkest day becomes bright thanks to him. Last but never the least, my beloved family. To my grandmother for loving me so much. To my sister, Valeria, and to my brother, Davide, who I miss both so much. To my parents for being immensely supportive in every choice I make. And of course, to my savior in my blue moments: my cat Po, who at time, I believe, he is very much smarter than I am.

DECLARATION

I declare that this thesis was composed by myself, that the work contained herein is my own except where explicitly stated otherwise in the text, and that this work has not been submitted for any other degree or processional qualification except as specified.

2019

Valentina Ferro, January 10th, 2019

PUBLICATIONS

Some ideas and figures have appeared previously in the following publications:

2018 Ferro, V., Chuai, M., McGloin, D., Weijer, C., "Measurement of junctional tension in epithelial cells at the onset of primitive streak formation in the chick embryo via non-destructive optical manipulation" – Submitted to Development, December 2018 (preprint available at https://www.biorxiv.org/content/early/2018/12/19/501775)

2016 Jannasch, A., Abdosamadi, M. K., Ramaiya, A., De, S., Ferro, V., Sonnberger, A., Schaffer, E., "Custom-Made Microspheres for Optical Tweezers." Book chapter in: Optical Tweezers: Methods and Protocols, Gennerich, A. Ed.,Springer New York, pp 137-155

2016 Ferro, V., Sonnberger, A., Abdosamadi, M. K., McDonald, C., Schaffer, E., McGloin, D., "Improved antireflection coated microspheres for biological applications of optical tweezers. '' in SPIE Nanoscience + Engineering 2016 (Conference Proceedings)

“ We must therefore not be discouraged by the difficulty of interpreting life by the ordinary laws of physics. For that is just what is to be expected from the knowledge we have gained of the structure of living matter. We must also be prepared to find a new type of physical law prevailing in it. Or are we to term it a non-physical, not to say a super-physical, law? ”

— E. Schrödinger, ‘What is life?’ —

PREFACE

Modern biophysics has flourished thanks to optical manipulation techniques. Recognising their importance, the 2018 Physics Nobel Prize was awarded to Sir Arthur Ashkin, the physicist who invented optical tweezers in 1986 [1]. For more than 30 years they have helped both physicists and biologists to understand a little bit more about life: from providing insights into light-matter interactions –through studies on light beam properties [2, 3], angular momentum [3–5], colloidal science [6, 7], optical matter [8–10] and even Bose-Einstein condansates [11]– to their applications to biological systems, from molecular to cellular biology. The attention to this technique has not faded since (As shown in Figure i.1).

The announcement of the Nobel Prize Award focused also on the applications of optical tweezers on biology, and their contribution to the advancement of biophysics. Today’s science is rediscovering the importance of multidisciplinary and interdisciplinary research [12], and optical trapping has been the tool of choice for many biologists thanks to their advantages over other techniques. In biological studies, genetic modification techniques allow experimentalists to modify the genetic code and observe changes in phenotype and behaviour. However, these obervations benefit to be complemented with studies on mechanical properties of biological subjects and of their environments. In light of interdisciplinary research, this means being able to modify, deform and displace biological matter at different size scales, from molecules to tissues [13–15].

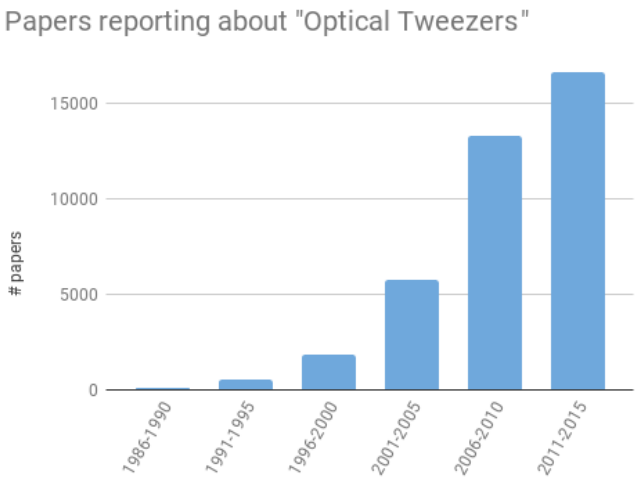

Figure i.1: **Optical tweezers interest through the years** – Reported number of papers including "Optical Tweezers" in their title as a result of Google Scholar search versus years.

Techniques for biological manipulation count scanning probes, direct contact manipulation, acoustic devices, microfluidics chip and, finally, electro-magnetic field traps [13, 14, 16]. The choice of the right manipulation tool is influenced by the size of the object to be manipulated, the forces required and the type of manipulation needed, e.g. whether 3D manipulation is important for the study [13].

Each technique has advantages and disadvantages. While scanning probes techniques, such as atomic force microscopy (AFM), operate at pN to hundred of nN forces and can been used at a wide range of size, from DNA to cells and tissues [13, 16], they are an intrusive contact tool and require the sample to be strongly attached to a surface. Direct contact techniques, such as manipulation through pipettes and micro-pipettes, offer forces in the nN to N regime and they are simple to use, but they cannot be employed for local interactions as the forces are applied on extended area in cell and tissues [17, 18]. Similarly, manipulation by acoustic forces cannot be used at sub-cellular level because their limitated resolution, despite being effective in sorting cells and particles [19–22] and convenient for handling the sample without contact. Microfluidics chips are versatile –because the forces generated by microfluidics devices are a results of different mechanical principles (e.g. hydrodynamic forces, wetting, capillary) [23]– and they are ideal in term of through-put, allowing to study and manipulate multiple objects at once or in the time frame of milliseconds, but they lack flexibility, limiting the experimental-

ists to use the devices specifically tailored to their goal, and forcing them to design a new chip for every new investigation.

Finally, under the umbrella of electromagnetic field gradient approaches, there are optical tweezers. Optical trapping has a resolution down to tenth of pN [16] while capable of forces of hundred of pN to few nN [16, 24, 25]. Optical trapping also provides a non-contact probe without special requirement for sample preparation. Compared to other techniques, optical tweezers offer great flexibility, both in term of force range and of sample size and, over the years, they have been employed to study very diverse types of samples (See Figure i.2.

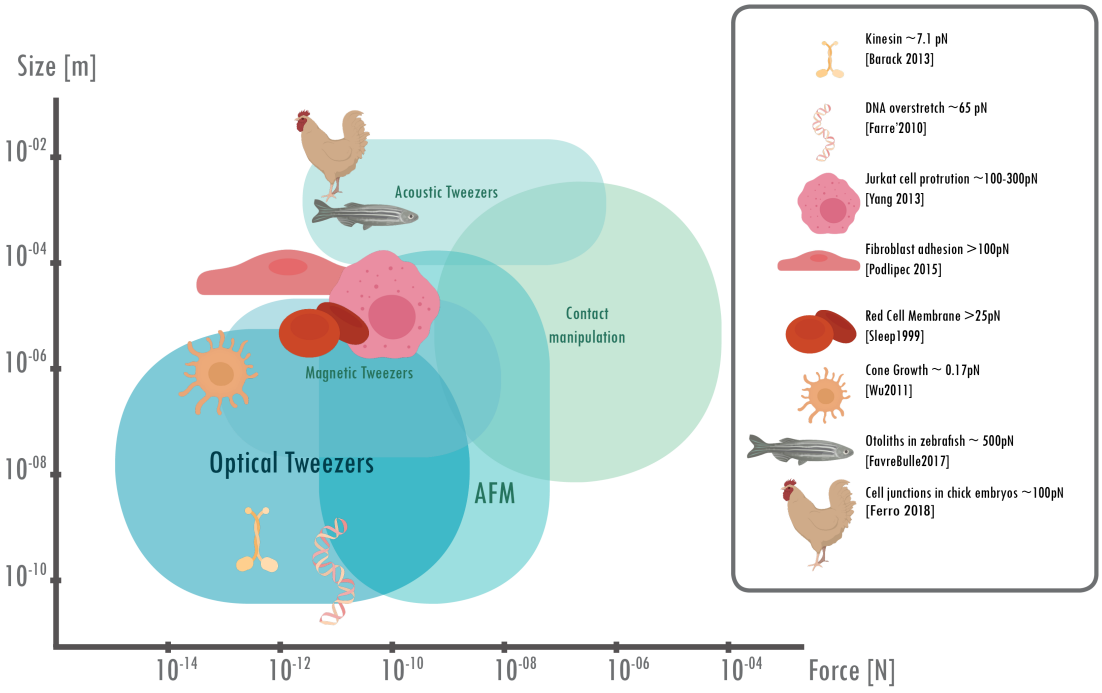

Figure i.2: **Overview of biological manipulation techniques** – Overview of major manipulation techniques for biological samples. Examples of biological forces as measured by optical tweezers are reported as cartoon markers. Notice that in the case of studies in living organism, as for zebrafish and chick embryos, optical tweezers were used to manipulate small components in the tissues and not the whole organisms.

OPTICAL TRAPPING AND THE ADVENT OF OPTICAL TWEEZERS

Every technique involving the manipulation of matter through light can be referred to as optical trapping, but *optical or photonic tweezers* specifically refer to three dimensions trapping by use of a single light beam.

Ashkin first reported optical trapping in 1970: he showed that two counter-propagating beams of light could hold a dielectric sphere trapped between them [26] and that a single beam could levitate particles against gravity [27] thanks to radiation pressure. It took more than 15 years for Ashkin to publish about optical tweezers in 1986 [1], but only one year after that, he started to envision tweezers' potentials in biology and set the pillars for their breakthrough in biophysics. In 1987, he used optical tweezers to trap and manipulate different types of cells [28], with more studies in biology following soon after [29, 30].

Optical tweezers applications for molecular biology are nowadays well established, including studies about molecular motors [29, 31–36], nucleic acids manipulation [15, 37, 38], phospholipid membranes [39], proteins folding and proteins interaction [24]. With regards to single cells, optical tweezers showed to be a powerful tool as well [14]. Optical tweezers allow the experimentalist to hold cells in specific positions [28, 40, 41], in both static and flow environments, to transport single cells to different locations in a sterile and not-contact condition [42–44], to assemble cells into new structures [2, 45–47], and finally to perform force measurements on cells [14, 48–56] and inside them [57–59]. Recently, the applications of optical tweezers have been extended to living organisms, with successful results [60, 61].

Despite the fact that optical tweezers are so widely used, biophysicists have been envisioning more and more applications in biology that require to push the boundary of the technique and to design custom-made solution for the specific study at hand. For example, many phenomena happening at the cell scale fall in the nN regime, e.g. aspects of cell motility, but they have seldom been studied locally because high strength optical tweezers are not commercially available, difficult to reproduce and challenging to use in biological enviroments. Similarly, the application of optical tweezers in living organism have been poorly characterised and still require intinsive studies to reach its full potential.

I have focused my studies in extending optical tweezers applications on these two fronts: from one side, I have worked on reproducing and optimising high strength tweezers capable of nN forces for application in cellular biology; from the other, I have designed and characterised optical tweezers for tissue biology. By studying these two aspects of trapping, I aim to show how optical tweezers can be further improved to increase their potential, and to present creative and novel applications in biology.

THESIS OUTLINE

The thesis is divided in two parts, tied together by an introductory chapter about the physics behing optical trapping (chapter 1) and a final chapter commenting on all the findings and results reported and their relevance (chapter 8).

HIGH STRENGTH PHOTONIC TWEEZERS Part one covers the experiments related to nN-capable tweezers and their application for single cells studies. I have introduced the literature review about high strength tweezers in Chapter 2, with a focus on the use of photonically structured probes; the same chapter reportd the method used to produce and optimise such probes. In Chapter 3, I have worked on characterising the probes and measure the forces generated by optical tweezers employing them. Finally, in Chapter 4, I presented the challenges related to use the probes for cellular biology studies, I showed how these probes can be functionalised and I reported proof of concept studies in biology where nN forces would be beneficial.

OPTICAL MANIPULATION OF CELL JUNCTIONS IN CHICK EMBRYOS In part two, the focus is shifted to the study of mechanical properties of tissues during developement. In particular, I have used optical tweezers for studying mechanical properties of chick embryos. In Chapter 5, I have highlighted the relevance of these experiments and discussed the current understanding of how forces in the tissues affect chick embryos development. After describing the novel methods I devised for such application, its limitation and its challenges in Chapter 6, I reported the results obtained and commented them in Chapter 7.

1

OPTICAL TRAPPING

Half a century has passed since Ashkin published the first evidence of optical manipulation of microscopic objects in 1970 [26]. While the techniques to produce optical traps have evolved considerably, we can use Ashkin's original reasoning to understand the principles behind optical trapping [1, 62].

Photons, the particles representing the quantum of light, carry energy that can be expressed as $u = pc$, in term of their momemtum $p = \frac{h}{\lambda}$, where h is the Plank constant, λ the light wavelength and c the speed of light [26, 63]. When photons are elastically scattered by an object, their momentum changes direction. Because of the momentum conservation law, the object experiences a recoil force in return. If the object is a perfect mirror, a light beam of power P reflected at 180 degrees undergoes a total change in momentum of $-2Np$, where $N = P/u$ is the number of photons in the beam. Therefore, the mirror is pushed with a recoil force [26, 63]

$$F_{refl} = \frac{2P}{c} \tag{1.1}$$

in the direction of propagation of the incident beam.

The force generated by a beam of considerable power, e.g. P=100 mW, is only hundreds of pN -too small to be experienced in everyday life. Howver, these forces become observable when working with microscopic particles. Moreover, when the light has a strong intensity gradient, an additional force is generated that allows to hold particles in place, obtaining 3D trapping.

1.1 RAY OPTICS AND DIPOLE APPROXIMATION

For a spherical dielectric particle, the forces generated by a beam of light can be computed analytically. It is convenient to differentiate between three different regimes according to the particle radius R: the *Rayleigh regime*, when the size of the particle is smaller than the wavelength, $R \ll \lambda$; the *geometrical optic regime*, when the size of the

particle is greater than the beam wavelength, $R \gg \lambda$; finally, the *Mie Scattering* regime when the size of the particle is of the same order of the wavelength, $R \simeq \lambda$.

GEOMETRICAL OPTICS REGIME $R \gg \lambda$

For dielectric particles that are bigger than the wavelength, $R \gg \lambda$, the electric field is uniform inside the particle. Therefore, we can use ray optics to determine what force a laser beam applies to the bead.

An object reflects a light ray at an angle ϑ_r equal to the angle of incidence ϑ_i:

$$\vartheta_r = \vartheta_i \tag{1.2}$$

The same ray is also refracted according to Snell's law by an angle ϑ_t given by:

$$n_i \sin \vartheta_i = n_t \sin \vartheta_t \tag{1.3}$$

Where n_i and n_t are the refractive indexes of the external medium and of the dielectric sphere, respectively.

For a ray hitting the sphere off centre, a small component of the ray power is reflected, while the rest is refracted inside the sphere. The ray will be reflected and refracted again every time it reaches the surface between the dielectric sphere and the external medium (see Figure 1.1).

Limiting our observation at the first two scattering events (first reflection and first trasmission of the ray), and considering Equation 1, the total recoil force acting on the sphere is [64]:

$$F = \frac{n_i P_i}{c} - \frac{n_i P_r}{c} - \frac{n_t P_t}{c} \tag{1.4}$$

Where P_i indicates the initial incident power, P_r the amount of power being reflected and P_t the one being transmitted.

We can split the final force vector into its two components: one is parallel to the incident ray, and it pushes the sphere away, the other is perpendicular and, assuming $n_t > n_i$, it pulls the sphere to align its centre towards the direction of the ray (Figure 1.1). We call the parallel component *scattering force* and the perpendicular one *gradient force*.

With a single ray, it is impossible to achieve stable 3D trapping, as the scattering component of the force always pushes the sphere away from the beam. However if we

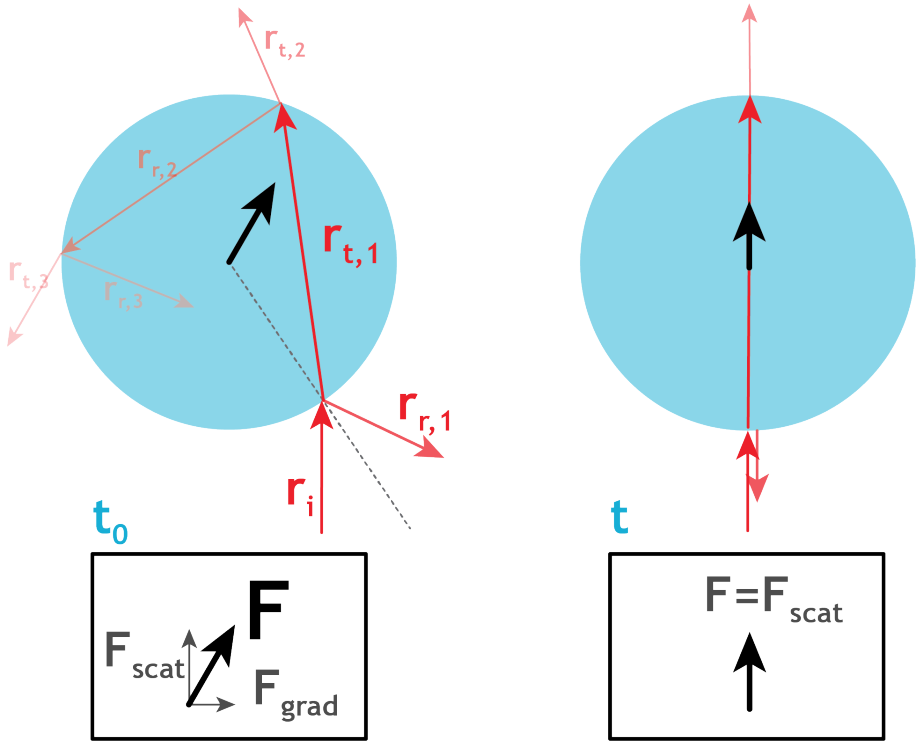

Figure 1.1: **Optical forces in geometrical optics** – Schematics of optical paths for a single ray hitting a sphere. At time t_0 the ray r_i incident on the sphere is both reflected ($r_{r,1}$) and refracted ($r_{t,1}$); it is further reflected and refracted at every interface ($r_{r,j}$,$r_{t,j}$). Considering only the first two scattering events, the net recoil force F acting on the sphere (black arrow) is composed by a component parallel to the original incident ray, the *scattering force* F_{scat}, and one perpendicular to it, the *gradient force*F_{grad}. The first component pushes the sphere away, while the second one pulls the sphere so that its centre is aligned with the incident ray. After enough time t, the sphere is aligned and the gradient force is null. The sphere is pushed away from the ray: with a single ray it is not possible to obtain 3D trapping.

uses gravity to balance the scattering force, we can built a type of trapping called *optical levitation* - it was optical levitation that Ashkin published first! With two rays hitting the sphere at a large angle, then the gradient force components of each ray generate a force pulling the sphere toward the focus (see Figure 1.2). Stable axial trapping is obtained when the gradient force overcomes the scattering force.

If the two rays have also different power, then the resulting gradient force not only pulls the sphere in the axial direction, but it also attracts it toward the stronger ray (see Figure 1.3).

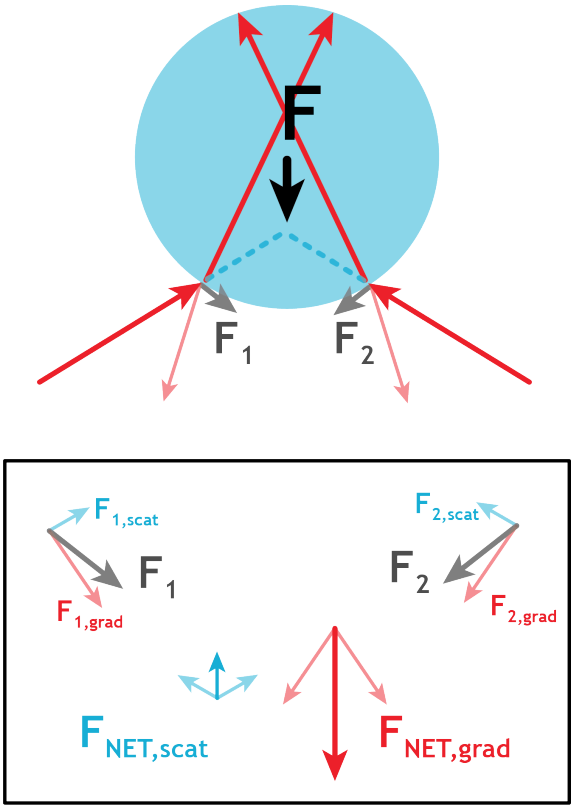

Figure 1.2: **Axial gradient force in geometrical optics** – When the rays of the light beam are focused to a tight spot, the net force acting on a sphere pull it toward the focus of the beam (dashed line). As shown in the bottom insert, the two forces F_1 and F_2 generated by two opposite rays are decomposed into their force components. The components add together into a net scattering force $F_{NET,scat}$ and a net gradient force $F_{NET,grad}$. The total net force on the sphere is the sum of $F_{NET,scat}$ and $F_{NET,grad}$. When the gradient force is greater than the scattering one, the sphere is pulled toward the focal spot of the beam.

A laser with a Gaussian intensity profile focused to tight spot at large angels (i.e. the ones obtained by a high numerical aperture lens) matches all the requirements to achieve trapping both in the axial and the lateral direction.

RAYLEIGH REGIME $R \ll \lambda$

For Rayleigh particles, ($R \ll \lambda$), we can consider the microscopic spheres as point dipoles. In this approximation we can also split the force into two components.

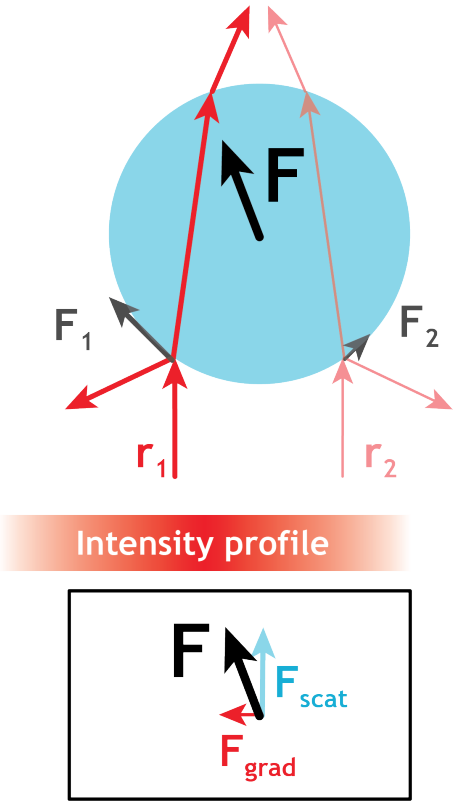

Figure 1.3: **Lateral gradient force in geometrical optics** – Two rays of different intensities, e.g. the ones generated by a beam with Gaussian intensity profile, generate a net force that pulls the sphere toward the strongest ray. In the insert at the bottom, it is shown that the net force has a component of gradient force pulling toward the centre of the beam.

The scattering force is generated by the dipole first absorbing and then re-emitting the radiation [24]. Considering the scattering cross section for a sphere [24]

$$\sigma = \frac{128\pi^5 R^6}{3\lambda^4}\left(\frac{(n_r/n_i)^2-1}{(n_r/n_i)^2+2}\right)^2 \tag{1.5}$$

the scattering force, directed along the axis of the incident beam, can be expressed as [1, 64]

$$F_{scat} = \frac{n_i P_r}{c} = \frac{I_0}{c}\frac{128\pi^5 R^6}{3\lambda^4}\left(\frac{m^2-1}{m^2+2}\right)^2 n_i \tag{1.6}$$

where I_0 is the intensity of the field and m is the *effective refractive index* $m = n_t/n_i$ [1, 24].

The second component, the gradient force, is due to the intensity gradient of the beam in the focal spot, and is given by [1, 27, 64]

$$F_{grad} = -\frac{n_i}{2}\alpha \bigtriangledown E^2 = -\frac{n_i^3 R^3}{2}\left(\frac{m^2-1}{m^2-2}\right) \bigtriangledown E^2 \tag{1.7}$$

where E is the electric field and α is the polarisability of the sphere. In term of the intensity, the gradient force is written as $F_{grad} = \frac{2\pi\alpha}{cn_i^2} \bigtriangledown I_0$ [24].

Even with using Reyleigh equations, it is necessary that the gradient force overcomes the scattering one.

MIE SCATTERING $R \sim \lambda$

For the majority of tweezers applications, the size of the trapped object is comparable the trapping laser wavelength. Trapping is still achieved, but the equations for the Rayleigh and the geometrical optics regime are not valid.

Mie Theory describes the equations for the scattering of a linerly polarised wave by a sphere thus providing a complete solution for the problem [65]. In solving Mie's equations, no assumptions are made on the sphere's size and refractive index, making them valid for every regime.

The description of Mie equations is beyond the scope of this thesis, and can be easily accessed in literature [64, 65]. Nevertheless, it is worth mentioning that the *T-Matrix* method [66, 67], a widely used numerical approach for the determination of optical forces also used in this work, is a generalisation of Mie theory.

1.2 OPTICAL FORCES: LOW REYNOLDS NUMBER AND BROWNIAN MOTION

During trapping, the trapped object is held slightly above the focus of the laser beam, and if it is displaced from its equilibrium position, a restoring force brings it back towards the focus.

In other words, the focused beam can be described as an attractive potential well. For small movements of the sphere, the attractive force is proportional to the displacement. Therefore, the trapping forces for optical tweezers can be expressed by *Hooke's Law*:

$$\begin{aligned} F_x &\approx -\kappa_x(x - x_{eq}) \\ F_y &\approx -\kappa_y(y - y_{eq}) \\ F_z &\approx -\kappa_z(z - z_{eq}) \end{aligned} \tag{1.8}$$

κ takes the name of *trap stiffness*, and it is equivalent to the elastic constant in an hookean spring.

So far, we have only discussed the optical properties of the particle trapped and the medium, neglecting other forces affecting a sphere immersed in a fluid, such as Brownian motion and drag forces.

BROWNIAN MOTION

A micrometric sphere immersed in a fluid undergoes a permanent motion, due to the collision with the molecules in the fluid. A sphere subjected to an optical trap is trapped when it is in dynamic equilibrium between the thermal motion that might push the sphere out of the trap and the optical forces pulling it toward the focus. Therefore, the potential well associated to optical tweezers must be a few $k_B T$ deep, with k_B indicating the Boltzmann's constant and T the temperature in Kelvin, to confine the particle.

REYNOLDS NUMBER

When a particle moves in a fluid, it experiences viscous forces. Even water represents a very viscous medium for particles of micrometric size, and inertial forces do not play a role in the particles movement [68, 69].

A characteristic parameter for systems immersed in fluids is defined by the ratio of inertial forces over viscous ones. This parameter is called *Reynolds number*, $\mathcal{R}$, and is equal to [68]:

$$\mathcal{R} = \frac{av\rho}{\eta} \tag{1.9}$$

where ρ is the density of the medium, η its dynamic viscosity, v is the relative velocity of particle and medium and a is a characteristic length for the specific system, e.g. the radius of the particle.

Typical conditions for optical tweezers experiments are characterised by low Reynolds numbers, $\mathcal{R} \ll 1$. The viscous force for a sphere is described by Stokes' law:

$$F_{Stokes} = -\gamma v \tag{1.10}$$

Where

$$\gamma = 6\pi\eta R \tag{1.11}$$

is the drag coefficient.

The Brownian motion of a particle is also affected by the presence of drag forces. This is reflected in the diffusion coefficient, as expressed by the Stokes-Einstein equation:

$$D = \frac{k_B T}{\gamma} \tag{1.12}$$

1.3 OPTICAL TWEEZERS SET-UPS

A typical set-up for optical tweezers is relatively simple to build [70, 71]. Figure 1.4 portrayes the minimal requirements for optical tweezers set-ups; additional optics can be added for specifics applications.

A laser with a Gaussian intensity profile is focused through a microscope objective with high numerical aperture. The objective performs two roles: from one side it acts as a focusing lens for trapping, from the other it images the sample into a camera, as per commercial microscopes. Typically, immersion oil objectives are preferred for trapping, because they can achieve higher numerical apertures.

To image the sample, bright field illumination can be used. Typically a *Köhler illumination* is employed because of its uniform light field and enhanced contrast compared to other illumination techniques.

A dichroic mirror is placed under the objective; this reflects only the trapping laser light, while transmitting the rest: the image of the sample without the one of the trapping laser is collected by the objective and directed to the camera.

To manipulate a trapped object relative to its environment, we could either move the sample with a stage while keeping the object in the trap or move the trapping laser, and with it the trapped object, with a steering mirror. Placing the steering mirror at the right distance from the condenser lens is fundamental if one wants to prevent aberrations and achieve true two-dimensional manipulation. In fact, if the angle of the beam is changed by a mirror without appropriate optics in between, the beam will be shifted at the back focal plane of the objective resulting in an asymmetric focal spot in the image plane. The

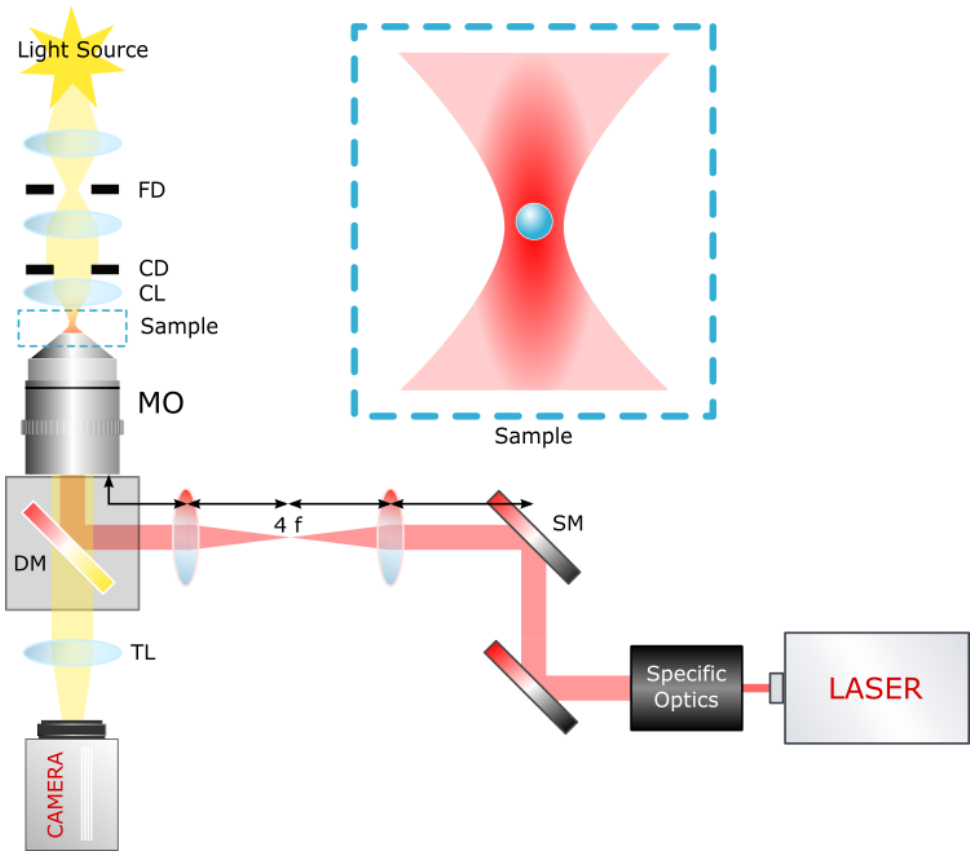

Figure 1.4: **Basic optical tweezers set-up** – Specific optics shapes a laser beam prior to reach the condenser lens; typically this includes a beam expander to obtain the desired filling-ratio, but additional optics can be used for specific applications. The beam is directed on the back focal plane of a microscope objective through a steering mirror (SM). The position of the laser focus in the sample plane is determined by changing the angle of the steering mirror; thanks to a 4f relay system of lenses (see Figure 1.5). A camera images the sample through the same objective and a tube lens (TL) of adequate focal length. A dichroic mirror (DM) reflects the laser light while transmitting the image to the camera. Kohler illumination is typically used to illuminate the sample: a light source is focused at a field diaphragm (FD) and then collected by a condenser lens (CL) passing through a condenser diaphragm (CD).

best practice for steering mirrors is to place a 4f imaging system between the mirror and the objective. A 4f imaging is composed of two lenses positioned at a distance equal to the sum of their focal length f_1 and f_2; the plane A_1 at distance f_1 from the first lens is conjugated to the plane A_2 at a distance f_2 from the second lens (see Figure 1.5), i.e. the intensity distribution at one of these planes is an image of the intensity distribution of the other [72]. Likewise the two planes that in Figure 1.5 are referred to as B_1 and B_2 are conjugated to each other. Using a 4f, an angular tilt at the mirror plane (A_1) modifies

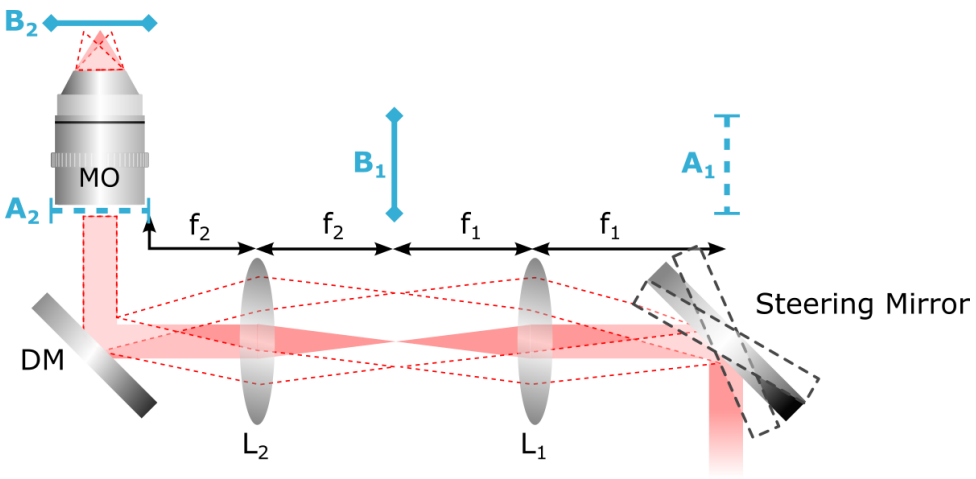

Figure 1.5: **Conjugate planes in 4f system** – A 4f system is composed by two lenses positioned at a distance equal to the sum of their focal length f_1 and f_2; the plane A_1 at the steering mirror is conjugated to the plane A_2 at the back focal plane of a microscope objective. Likewise, the plane B_1 is conjugated with the plane B_2 in the image plane. An angular tilt at the mirror plane (A_1) results in a shift at the image plane (B_2).

the position of the laser focus only in the image plane, without additional aberrations or tilting in the back focal plane of the objective.

FILLING RATIO AND NUMERICAL APERTURE

Both the geometrical optics and the Rayleigh theory help us determine the practical requirement for efficient trapping. These theories show that an increase in trap stability is obtained by using large angles to focus the laser beam, rather than by using more laser power. The numerical aperture of a lens, NA, determines the largest angle at which a light beam can be focused and it is defined as

$$NA = n \sin \varphi \tag{1.13}$$

where n is the refracting index of the medium (i.e. $n = 1.52$ when immersion oil objectives are used) and φ is the maximal angle at which a light ray can enter the lens.

In the geometrical optics theory, rays with larger converging angles have larger components of the gradient force pulling the object toward the laser focus: they help to overcome the scattering force pushing the object. Likewise, in the Rayleigh description, the scattering force scales with the intensity, while the gradient force increases with

the gradient of the intensity. An increase in the intensity gradient can be obtained by focusing through an high numerical aperture lens.

Another parameter that contributes to the trapping efficiency is the ratio between the beam waist and the aperture of the focusing lens [62], often referred to as *filling factor*. Often, to improve the stability of the trap, the aperture of the lens is slightly overfilled by the laser beam. It is worth mentioning, however, that there are circumstances in which under-filling is preferable, especially for really high numerical apertures (like the ones used for TIRFM [1] objectives) [73]. Most noticeably, the optimal filling ratio depends also on the particle size [73].

PARTICLES PROPERTIES

The characteristics of the trapped object also play a role in the trap quality. The equations in section 1.1 imply that the effective refractive index is a fundamental component to determine the trap stability. For instance, with a Gaussian beam, trapping is only possible when the effective refractive index $m > 1$.

More interestingly, the way scattering and gradient forces depend on the refractive index is different. From Equation 1.6, we can observe that the scattering force scales with the square of the refractive index difference $\Delta n = n_t - n_i$ [74]:

$$F_{scat} \propto \Delta n^2 \tag{1.14}$$

The gradient force, instead, is only proportional to Δn

$$F_{grad} \propto \Delta n \tag{1.15}$$

Same conclusions are obtained using the equations for the geometrical optics regime [74]. As a consequence, attempting to improve the trapping efficiency by increasing the effective refractive index fails. For example, for high refractive index particles immersed in water, i.e. with $n > 1.73$, the scattering force overcomes the gradient one and makes trapping impossible [75].

Furthermore, Equation 1.7 makes evident that the sphere size can also affect the quality of trapping. In fact, the polarisability α is proportional to the particle volume, and so the gradient force and the trap quality is proportional to the particle size [75, 76].

1 TIRF stands for Total Internal Reflection Microscopy.

1.4 FORCE MEASUREMENT AND CALIBRATION

Optical tweezers are often employed as force transducers, to exert and measure forces on a specimen. These forces can be quantified if the trap stiffness κ is known, i.e. if we have calibrated the tweezers. The extend of the Brownian motion of an optically trapped object directly correlates with the shape of the potential well generated by the trapping laser. Therefore, we can measure of the trajectory of the trapped object to evaluate the tweezers trap stiffness.

Interferometric techniques can provide precise measurements [35, 77] of the particles' trajectories, with sub-nanometre and megaheartz resolution. The light incoming towards the trapped object is partially scattered by the object itself and partially left un-scattered; the light field in the forward direction after the sample plane is the superposition of the un-scattered incoming beam and the scattered beam [78]. The intereference pattern of the forward light measured with a photodetector is proportional to the object movements.

FORWARD-SCATTERING BACK FOCAL PLANE INTERFEROMETRY

A condenser lens, usually another microscope objective, is used to collect all the forward-scattered light into a photosensitive device conjugated with the back focal plane of the objective. The light intensity at the back focal plane, and therefore at the detector, has a single-lobe angular distribution: the displacements of the lobe are proportional to particle lateral displacements [31, 64, 79]. However, at the detector these displacements are measured in volts. To convert the trajectory measured in volts to metre units, we need to estimate the *displacement sensitivity*: the volts signal as a function of the particle displacement. The displacement sensitivity depends on the the detector used and on the intensity distribution of the forward scattering light, that in turn is determined by the particle size and the specifics of the tweezers set-up.

The most common devices used for photodetection are quadrant photodiodes (QPD) and *position sensing detectors*. For QPD, the centre of the distribution is inferred by measuring the intensity difference between left and right quadrants and between top and bottom quadrants (see Figure 1.6). Position sensing detectors directly measure the posi-

tion of the centroid of the intensity distribution. Their performance is comparable when the intensity distribution is Gaussian (like in the case of single-lobed forward scattering) but position sensing detectors become more sensitive for non-Gaussian distributions [64].

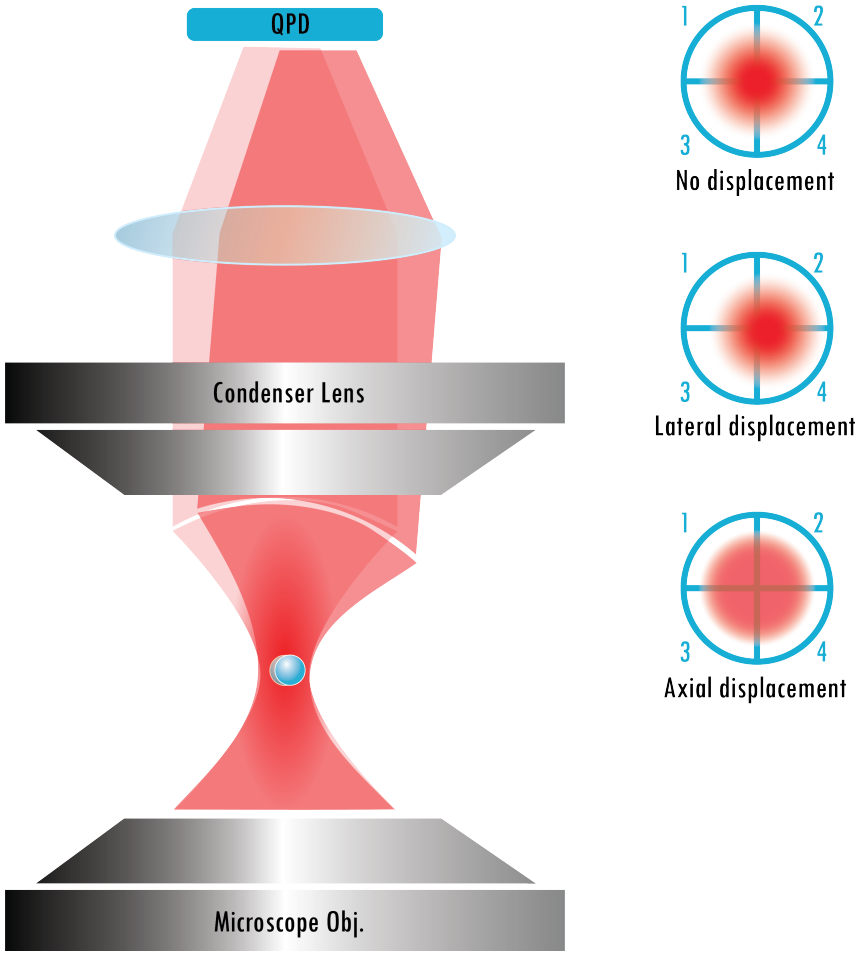

Figure 1.6: **Displacement detection by QPD** – A displacement of the trapped object scatters the laser light, collected then by a condenser lens. The image at the back focal plane of the condenser lens is conjugated to a QPD. Subtracting two by two the voltage measured in each quadrant of the QPD, it is possible to determine the centre of the light distribution at the detector and therefore the lateral displacement of the sphere. An axial displacement of the trapped object results in a difference in the total light collected by summing the signals from all four quadrant of the detector.

Axial movements of a trapped particle can also be measured by interferometric techniques: in fact, an axial displacement changes the relative phase difference between incoming un-scattered field and the scattered one [64], resulting in a different amounts of total light collected at the photodetectors.

BACKWARD-SCATTERING BACK FOCAL PLANE INTERFEROMETRY

Sometimes it is impossible to set-up a forward-scattering detection. Certain biological samples, for example, are highly scattering media where most of the light is scattered and absorbed by the sample itself, with little left to reach the photodetector. In these circumstances, backward scattering interferometric techniques might be used.

The detection principle is the same, but backward-scattering detection is more complex. The signal-to-noise ratio is typically lower than for forward-scattering interferometry and the shape of the interference pattern has multiple lobes for particle with diameter larger than $1\mu m$ [64, 80]. Theoretical descriptions of the backward-scattering back focal plane interferometry [64, 80] suggest that different filling-ratio and numerical apertures produce different outcomes when the particle size is kept constant, making the technique highly sensitive to the set-up used [81, 82]. Furthermore, because the size of the trapped object affect the interference pattern too, a small variance in size can also compromise the interpretation of these studies.

1.5 CALIBRATION TECHNIQUES

To measure forces in an optical trap, the Hooke's law equation $F = -\kappa x$ is used; to apply this equation experimenters need to calibrate the system to determine both the trap stiffness κ and the displacement sensitivity β of the detector.

DISPLACEMENT SENSITIVITY

The displacement sensitivity consists of the relationship between displacements of the trapped particle from its equilibrium and the signal collected at the detector (i.e. Volts in QPD).

The conversion factor from Volts to metre depends on the specifics of the system (e.g. numerical aperture of the microscope objective and the overfilling factor), but also on the characteristic of the trapped object. A common approach to obtain β is to fix the object we would like to trap onto a coverslip and scan it over the laser, while recording the QPD output voltage. Knowing the displacement applied to the stage, then we can plot a displacement sensitivity curve. When the objects to trap are commercial silica or

polystyrene spherical beads, their size variance is small enough that measuring β for a sample of beads provides a good estimate for the whole batch.

This method fails, however, to measure the displacement sensitivity for non-spherical objects or for custom made probes with high variance in size. Alternatively, an active calibration method can be used without any assumption on the particle's size section 1.6.

POWER SPECTRUM ANALYSIS TO DETERMINE TRAP STIFFNESS

The power spectrum density (PSD) analysis is the most common method when it comes to optical tweezers calibration. While other techniques consider the displacements distribution of the trapped object (i.e. equipartition and optical potential calibration techniques), the power spectrum analysis works in the frequency domain. This facilitates, for example, to clean the data from sources of noise, such as the noise due to the mains electricity, that in the PSD appear as well-defined peaks.

The PSD is calculated by taking the fourier transform of the equation for a trapped object [64]. The PSD is a Lorentzian curve that describes the thermal motion of the trapped object:

$$P_{th}(f) = \frac{D}{2\pi(f_c^2 + f^2)} \tag{1.16}$$

where we indicated the frequency with f and the diffusion coefficient in the medium with D. We have introduced the *corner frequency* $f_c = \dfrac{\kappa}{2\pi\gamma}$. To obtain the corner frequency we can fit the power spectrum with a Lorentzian curve. The corner frequency is then used to determine the trap stiffness, provided that the drag coefficient γ is known and the power spectrum is converted from $\frac{V^2}{Hz}$ to $\frac{m^2}{Hz}$ thanks to the displacement sensitivity β.

1.6 SELF-CALIBRATING BACK FOCAL PLANE INTERFEROMETRY

The PSD calibration technique relies on the knowledge of the displacement sensitivity and of the drag coefficient. But there are applications where these two quantities are difficult to determine. A self-calibrating technique solves this conundrum.

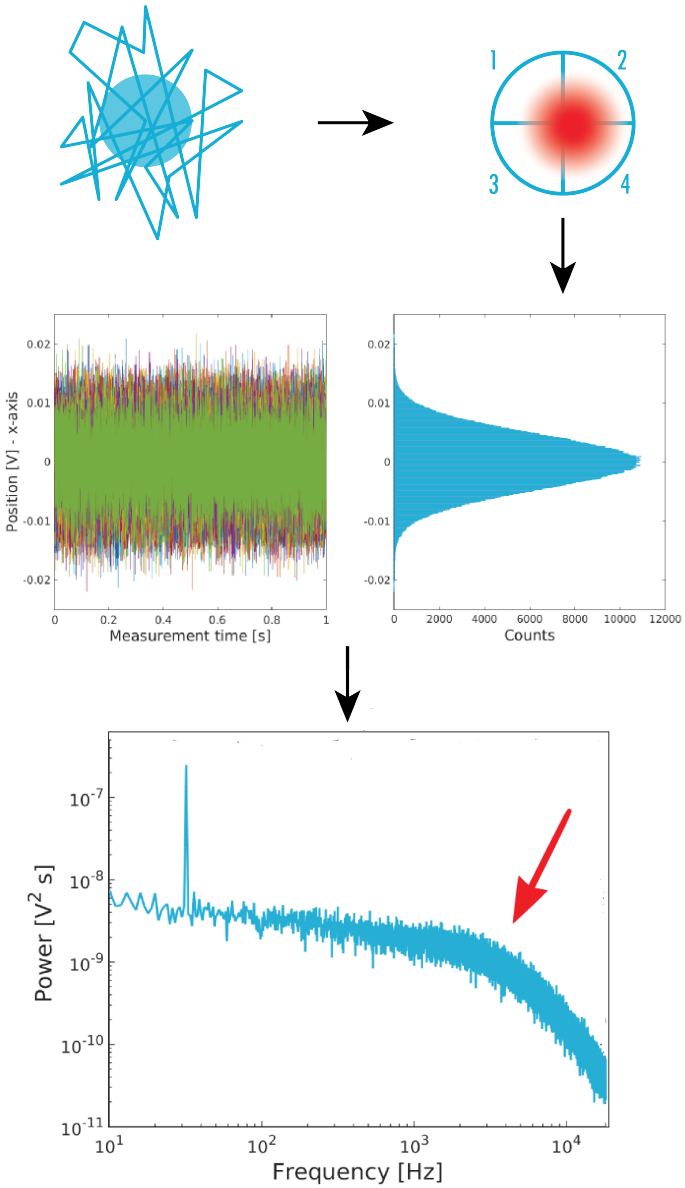

Figure 1.7: **Power Spectrum** – The displacements of the trapped objects are collected by a QPD. The different voltage values, corresponding to the sphere displacements, have a gaussian distribution, as predicted for the thermal motion of an object confined in a potential well. The power spectrum is calculated by taking the fourier transform of the gaussian distribution. The red arrow indicates the corner frequency used to determine the trap stiffness. Notice that the power spectrum reported is calculated through the method described in section 1.6.

As for the standard back focal plane interferometry, a QPD acquires the position of a trapped beads through back focal plane detection. A known periodic disturbance, e.g. a sine wave, is applied to the sample: when the trapped object oscillates with a sine wave

of amplitude A and frequency f_{drive}, the power spectrum acquired by the QPD is the sum of the thermal motion of the bead and its response to the sinusoidal motion [83].

The coupled power spectrum is given by

$$P(f) = P_{th}(f) + P_{response}(f) \tag{1.17}$$

Where $P_{th}(f)$ represents the spectrum of the Brownian motion of the bead (as per Equation 1.16).

The response to the sinusoidal motion is given by a delta function, where the amplitude depends on A (in metre), on the corner frequency f_c and on f_{drive}[83]:

$$P_{response}(f) = \frac{A^2}{2(1 + \frac{f_c^2}{f_{drive}^2})}\delta(f - f_{drive}) \tag{1.18}$$

The fitting of P_{th} provides a value for the diffusion coefficient D_V, expressed in volts, and the corner frequency f_c. The displacement sensitivity β can be obtained by knowing the corner frequency, as it used to calculate p_{res}:

$$\beta = \sqrt{\frac{p_{res}}{p_{ex}}} \tag{1.19}$$

Where p_{ex} is the value of the peak found at f_{drive} in the collected spectrum, measured in V^2, while p_{res} is the theoretical value obtained in m^2 from the integration of $P_{response}$

$$p_{res} = \frac{A^2}{2(1 + \frac{f_c^2}{f_{drive}^2})} \tag{1.20}$$

The trap stiffness is finally calculated from the definition of the corner frequency f_c and Einstein's relation for diffusion:

$$\kappa = 2\pi f_c \frac{k_B T}{D} = 2\pi f_c \frac{k_B T}{\beta^2 D_V} \tag{1.21}$$

Where β is used to convert D_V to D.

When using this technique the trap stiffness can be determined without prior knowledge on the properties of the probe, such as the diameter of the beads and the density of the material, or on the property of the medium, such us the drag coefficient.

1.7 CONCLUSIONS

By using simple geometrical optics and a few basic formulas on the dipole approximation, one can obtain all the fundamental information about optical tweezers. It is remarkable how even these *simple* physics equations resulted in a jolt in the field of biophysics. I will discuss in the following chapters applications of optical tweezers in cellular and developmental biology, and my effort to further push knowledge forward.

Optical tweezers, of course, can be more sofisticated than what I hereby described, but I wanted to present only notions needed to understand the experiments I conducted and that I present in this manuscript.

Part I

HIGH STRENGTH PHOTONIC TWEEZERS

2

PHOTONICALLY STRUCTURED MICROSPHERES FOR OPTICAL TRAPPING

The majority of optical tweezers used in literature operate in a range of forces of tenths to hundreds of piconewtons. While many studies, both in physics and in biology, have benefitted from this range of forces, the recent years have seen an increasing interest in extending this range. Specifically, certain biological applications might require higher forces, i.e. on the nanonewton scale for the study of highly motile cells like *Dictyostelium Discoideum*. Higher trap stiffness is also desirable to reduce damage in the biological samples, since stronger tweezers would achieve the same forces with lower laser power.

Despite the fact that nanonewton forces have been achieved by optical tweezers [25], it is still a difficult task to implement tweezers set-up to reproduce these results. Further reasearch is needed to make nanonewton tweezers an accessible resource in the portfolio of techniques for biologists and biophysicists.

In this section of the thesis, I will explore what techniques could be used to improve the efficiency of optical tweezers. I will discuss why the optimisation of the trapped probes is particularly attracting, in term of cost and implementation, and what I have done to improve the reproducibility issues with this specific type of high strenght tweezers.

2.1 HIGH STRENGTH OPTICAL TWEEZERS

Defining a *trapping efficiency* helps to evaluate and compare the efficiency of different optical tweezers. This is referred to as *Q-value* (indicated with Q) [62], a dimensionless quantity that represents how effectively the light momentum is transferred to the particle:

$$Q = \frac{c}{n_i P_i} F \tag{2.1}$$

where c is the speed of light, n_i is the refracting index of the medium, P_i is the power of the incoming beam and F is the measured optical forces. Theoretically, $Q = 2$ is the maximum Q-value possible and it is achieved in the case of complete reflection at normal incidence, i.e. the mirror example of Equation 1. Typical *Q-values* for tweezers lie around 0.1 and 0.04 for the transversal and axial direction respectively.

OPTIMISING OPTICAL TWEEZERS SET-UPS One approach to improve the quality of optical tweezers is to optimise the optical set-up. This can be done by reducing the spherical aberration of the trapping laser, e.g. with the use of an immersion oil of appropriate refractive index to compensate for them [84]. Alternatively, optimising the filling ratio would also enhance the optical trapping [73]. The general advice when building an optical tweezers set-up is to over-fill the back aperture of the microscope objective, but for certain sphere sizes underfilling the microscope objective would improve the trapping efficiency [73]. The maximum Q-value obtained by either of these approaches is 0.09 for the axial direction (and 0.19 for the lateral one). However these methods are not very versatile, as one would need to continuosly change the immersion oil or to optimise the filling ratio every time a new experiment with slighly different parameters is to be conducted.

OPTIMISING THE BEAM The intensity profile of the trapping laser also determine the efficiency of tweezers. Beam shaping can reduce the spherical aberrations [85] or can be used to manipulate the scattering force [86, 87]. Donut-shaped lasers, especially, help increasing the tweezers' quality by reducing the scattering force in the axial direction, in favour of the gradient force [86, 88]. In an interesting approach, the scattered light is redirected and used for further enhancement by shaping the laser beam in a way that the trapped object acts as a beam splitter [87]. This latter method improved the corner frequency by a factor of 30, but only in one direction. Shaping the beam can provide impressive Q-values>0.3, but only for particles of larger sizes ($> 3\mu m$).

OPTIMISING THE PROBES Finally, the scattering force can also be reduced by using destructive interference at the trapped spheres. Bormuth *et al.* showed that polystyrine

spheres with a diameter of $\sim 800nm$ have a maximum in the trap stiffness and measured a *Q-value* larger than 0.2. Because the size of the sphere coincided with the wavelength of their laser in water ($\lambda = 1070nm$, so that $\lambda_{water} = \lambda / n_{water} \sim 800nm$), the dielectric sphere behaved as anti-reflection element. In fact, there is a phase shift of $(\ell + \frac{1}{2})\lambda$ (ℓ is an integer) of the rays reflected from the top and the bottom of the sphere, leading to destructive interference when the size of the sphere matched the wavelength.

Thus, Bormuth and co-authors used anti-reflecting coating to reproduce the same destructive interference effects on spheres of different sizes [74]. By coating polystyrine with a quarter-wave thick shell of SiO_2, they obtained a trap more than 2 times stiffer compared with uniform polystyrine or SiO_2 spheres of the same size. The choice of SiO_2 for the coating material is justified by its refractive index, $n_{SiO2} = 1.45$, that is close to the geometric mean between the refractive index of water (the medium where the spheres were suspended) and the refractive index of polystyrine.

These results were supported by Hu *et al.* [75]. They simulated spheres with an antireflection coating of refractive index $n_{shell} = \sqrt{n_i n_t}$ and thickness $\lambda_{shell}/4$, obtaining a 3-fold increase in the axial direction. Exploring different thicknesses for the coating, they found that maxima in the trap stiffness do not occur exactly at $\lambda_{shell}/4 + \ell$. For example, the first peak is centred at $0.375\lambda_{shell}$ and the second at $0.9\lambda_{shell}$.

Coated polystyrene spheres are an interesting option for enhanced trapping. For example, Jannasch *et al.* reported nanonewton forces by adding an antireflection coating to spheres of high refractive index materials [25].

I focused my studies on this antireflection coating technique: compared to other literature methods of tweezers enhancement, the optimisaton of the probes makes for a versatile technique with a very high Q-value; moreover, once the probes are produced, they can be used in every optical tweezers set-up with the same workflow as commercial probes -in other words, they are a cost-effective and practical solution. However, the synthesis of coated high refractive index beads is still challenging and difficult to reproduce.

2.2 NANONEWTON FORCES WITH PHOTONICALLY STRUCTURED PROBES

Optical forces depend on the difference between the refractive index of the probe and that of the surrounding medium. But increasing the refractive index of the probes in order to achieve higher forces is not an option, because the scattering force eventually overcomes the gradient force leading to an unstable trap. For example, particles with a refractive index of 1.73 cannot be trapped in water [75]. Therefore, to trap a bead of titanium dioxide (TiO_2) in the anatase phase, with refractive index 2.3, one would need to reduce the scattering force by adding an antireflection coating [89]. Such coating need a refractive index of 1.75, equal to the geometric mean between the refractive index of TiO_2 and the one of water. A refractive index of ~ 1.78 can be obtained by using TiO_2 in a nanoporous amorphous form [89]. Through simulations, Jannasch *et al.* showed that the highest trap stiffness, $4pNnm^{-1}W^{-1}$ and $1.1pNnm^{-1}W^{-1}$ for lateral and axial trapping respectively, would be obtained for a anatase TiO_2 core of $500nm$ coated in a shell of amorphous $TiO_2 \sim 200nm$ thick.

The authors also confirmed these results experimentally: custom-made anatase TiO_2 cores coated in amorphous TiO_2 generated a trap stiffness of $3.8pNnm^{-1}W^{-1}$ and 0.9 $pNnm^{-1}W^{-1}$ for the lateral and axial trap stiffness. They measured a maximum force of 1.20 nN, for a *Q-value* of 0.25 –This is the highest *Q-value* ever reported for particles of comparable size.

While polystyrene spheres coated in SiO_2 can be trapped independently of their size [75], high refractive index probes can be trapped only for specific combinations of core-shell size. Unless these custom-made spheres are synthesised with low variance for both the size of the core and the thickness of shell, it is unlikely that all of them could be trapped. The fact that very few studies have repeated the synthesis and use of these beads, despite their desirable advantage in term of tweezers stiffness enhancement, suggests that there are also reproducibility issues.

I will demonstrate in the following sections, how I contributed to increase reproducibity of the chemical reactions, how the trappability issue can be compensated by using an additional coating layer and how I proposed alternative chemical reactions with higher yieald and more flexibility.

2.3 METHODS: SYNTHESIS OF PHOTONICALLY STRUCTURED PROBES

Jannasch *et al.* proved they could achieve nN forces using photonically structured probes [25]. However, employing titanium dioxide (TiO_2) core-shell particles for biological experiments is a difficult task. Tweezers using these probes are limited by a tight tolerance on the probes size: only microspheres in a small region of sizes can be stably trapped by optical tweezers.

For the optimal case of cores of 500nm in diameter with a 200nm thick shell, a 10% change of the shell size would be sufficient for the scattering force to exceed the gradient force, destabilizing the trap [25]. Microspheres samples produced by using the reported chemical synthesis protocols [25, 89] have a variance higher than 10%.

The method is also particularly sensitive to the characteristics of the tweezers set-up: the efficiency of trapping varies considerably using different filling factors and numerical apertures. As a result, beads that have been optimised for a certain optical set-up may not be trappable with another.

One way to overcome these isssues is to add an additional antireflection coating on the core-shell TiO_2 spheres reported in literature. I collaborated with the Nanoscience research group at the University of Tuebingen to achieve this result.

2.3.1 OPTICAL SIMULATIONS

To determine the optical forces acting on a coated microsphere, I simulated the system with the Matlab *Optical Tweezers Computational Toolbox* [67]. I chose anatase TiO_2, indicated as χTiO_2, for the core of the bead (refractive index $n_{core} = 2.3$) and nanoporous TiO_2, indicated as αTiO_2 for amorphous titania, (refractive index of $n_{shell} = 1.75$) for the shell. The simulation shows that the highest forces were obtained when a 500 nm core is coated with a shell $\sim 200nm$ thick, for a $\sim 900nm$ total size of the beads (Figure 2.1). The simulation agrees with that reported by Jannasch *et al.* [25].

Figure 2.1 shows that for several combinations of core-shell sizes the structured beads would not be trapped (white regions in the graph). This observation confirms that monodispersity within 10% is a strict requirement for the synthesis of custom made probes.

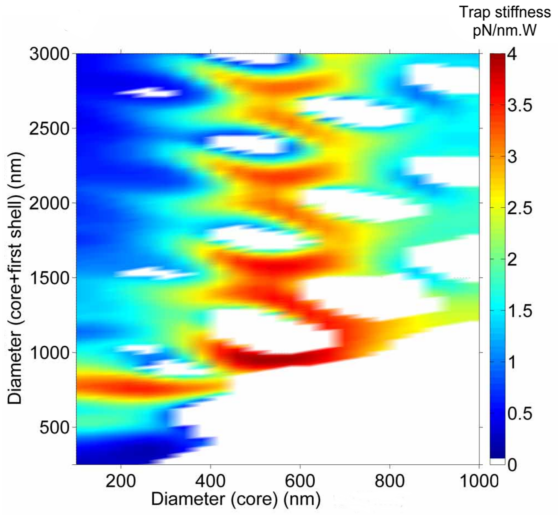

Figure 2.1: **Optical simulation of anti-reflective coated microspheres** – Simulated values for trap stiffness (in the y direction of bead motion) varying core sizes (x-axis) versus amorphous titania shell thickness (y-axis). The white regions represent sizes for which the beads will not be trappable.

Because the monodispersity for the αTiO_2 shells is difficult to improve, I ran a new simulation to investigate if an additional antireflective coating would solve the trappability issue.

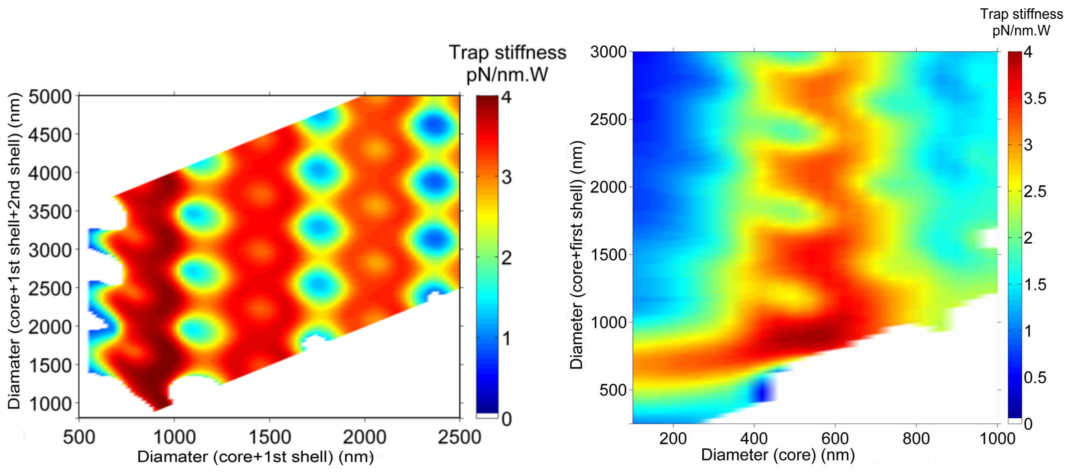

(a) (b)

Figure 2.2: **Optical simulation of anti-reflective SiO_2 coated microspheres** – Simulated values for trap stiffness (in the y direction of bead motion): (a) Fixing the core size at 500nm, while varying the first shell thickness (x-axis) versus total size (y-axis). The trap stiffness is highest for a 250nm thick silica shell. (b) Fixing the silica shell at 250nm, while varying core size (x-axis) versus core + titania shell size.

I chose SiO_2 for the second layer material, because its refractive index is close to the geometric mean between the refractive index of water and the one of amorphous titania used for the shell. The simulation showed that a silica layer $\sim 200 - 250nm$ thick would make beads of every size to be trappable (there are no more white regions in Figure 2.2) [90]. A variability in the titania or silica shell only results in lower trap stiffness.

The introduction of silica would provide additional advantages, as experimenters could use on these custom beads the same functionalisation techniques known for commercial silica probes [90].

2.3.2 SYNTHESIS BY BATCH REACTION

The synthesis of core-shell-shell titania-silica particles was carried out in three steps: the synthesis of anatase titania cores [89, 91, 92], the growth of amorphous titania shell on the cores [89, 92], finally the diffusion of silica in the titania shell and the contemporary growth of silica on top [89, 92] (see Figure 2.3).

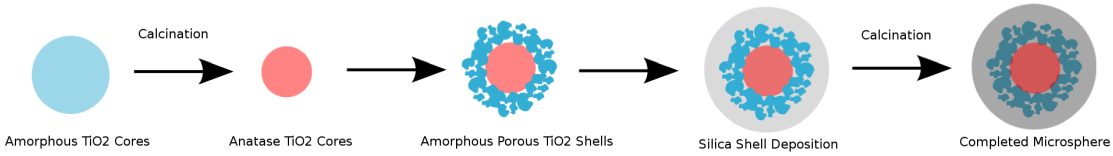

Figure 2.3: **Drawing of the batch reaction steps** – TiO_2 cores are synthesised. The particles are cured at 500 °C: the material is subject of a transition phase into anatase titania (χTiO_2). The same cores are used as nucleation centres for the growth of αTiO_2. The shelled spheres are then coated in SiO_2. Finally the core-shell-shell particles are cured again to strengthen the silica shell, but the transition of titania to the anatase phase is prevented by the presence of silica.

CORES SYNTHESIS Titanium dioxide can be obtained by the reaction of titanium(IV) butoxide $Ti(OBu)_4$ (TBT) with water. The reaction takes place in two phases: the nucleation of small grains of titanium dioxide, and the following growth of the nucleation sites to form the colloids. TBT is highly reactive, and this would result in a sample of titania beads with high variance in size [89]. To control the reaction, the nucleation phase needs to be separated from the growth phase. By reacting TBT first with ethylene

glycol ($HOCH_2CH_2OH$), titanium glycolate ($Ti(OCH_2CH_2OH)_2$), a more stable reactant, is obtained (with the waste of butyl alcohol ($HOBu$)):

$$Ti(OBu)_4 + HOCH_2CH_2OH \longrightarrow Ti(OCH_2CH_2OH)(OBu)_2 + 2\,HOBu$$

$$Ti(OBu)_4 + 2\,HOCH_2CH_2OH \longrightarrow Ti(OCH_2CH_2OH)_2 + 4\,HOBu$$

The $Ti(OCH_2CH_2OH)_2$ then reacts with water and the titania microspheres are produced:

$$Ti(OCH_2CH_2OH)_2 + 4\,H_2O \longrightarrow Ti(OH)_4 + 2\,HOCH_2CH_2OH$$

$$Ti(OH)_4 \longrightarrow TiO_2 \cdot xH_2O + (2-x)H_2O$$

For two batches of titania cores of 450-500 nm in size, I used two solutions:

A 200g of ethylene glycol (Merk) and 920μl of TBT (Sigma-Aldrich) were mixed on a shaking plate for one day. The obtained solution could be stored for about a week.

B 900ml of analytical acetone (Merk) was mixed with 900μl of milli-Q water and 2055 μl of Tween20 (Sigma-Aldrich). Tween20 is a surfactant that regulates the shape and the size of the titania beads.

I used two round bottom flasks [1], each filled with 40 ml of solution A and 400ml of solution B. The flasks were shaken harshly until the reaction fluids look clear. Already after a few minutes, the mixture became turbid and white, indicating the synthesis of the titanium dioxide. I left the flasks to react for 13 hours at room temperature. To interrupt the reaction and prevent further growth, after 13 h the mixture was centrifugated for 10 minutes at 3000 round centrifugal force (rcf); the supernatant fluid was removed and the pellet was resuspended in ethanol and sonicated for 10 minutes. The centrifugation was repeated and the pellet was resuspended in just 2 ml of ethanol and sonicated. Finally, to obtain anatase titania beads, I evaporated the ethanol at 100° C and calcinated the beads for 1 hour at 500° C. After the calcination, the beads were re-suspended in 8ml ethanol in glass bottle, sealed with Parafilm and stored. I performed 6 reactions for the core mixture, all with successful outcomes.

1 Round bottom flasks help the sedimentation of the beads

TITANIA SHELL SYNTHESIS The titania shell grows on the anatase cores by seeded growth: the cores behave as nucleation centres for the titania precursor (in this case pure TBT). The reaction is fast and the size and the shape of the products is regulated by the use of a surfactant, LutensolON50. LutensolON50 enhances the porosity of the amorphous titania [93], which is important to control the refractive index of the material and to later diffuse silica in the shell.

I found that the reported procedure for the growth of the titania shell [89, 92] failed to produce consistent results. For most of the samples it was impossible to obtain a shell thicker than 50-70nm. The samples with a shell thickness of more than 200nm were characterised by the presence of second nucleations and clusters. Only 2 samples, out of the 25 synthesised in the 12 months period preceding my collaboration with the Nanoscience Research Group at University of Tuebingen, presented shell growth of the desired thickness [94].

I modified the reported reaction [89] as follows.

- A 20ml glass bottle was half filled with: 8.92ml ethanol, 80μl diluted Lutensol (0.4 ml of LutensolON50 in 10ml of water), 1ml of resuspended cores.
- The reactants were introduced in the bottle in the order I presented above. I found that it is important to inject slowly the cores in the solution (2-3 minutes for the injection of 1 ml of cores mixture) to allows the surfactant to adhere better to the cores.
- The mixture was tip-sonicated for 2 minutes in an ice bath (the ice bath prevented local heating due to sonication).
- The bottle was brought to room temperature under magnetic stirring and 10 ml of TBT solution was added (0.2 ml TBT in ethanol).
- The bottle was left to react for 1h during magnetic stirring.
- Finally, the reactants were cleaned by centrifugation (5 minutes at 3000 rcf), while the beads were resuspended in ethanol and sonicated. This was repeated twice before storing the final products, like the cores mixture.

The parameters that affect the reaction include the temperature, the relative concentration of the reagents (TBT, water, LutensolON50 and Lutensol Solution, initial core solution), the methodology employed for the injection of the TBT into the core solution, the injection of the core mixture, the age of the Lutensol solution and the methods of mixing and sonication. Figure 2.4 summarises the average sizes of the synthesised beads when these parameters were explored. The procedure I described above refers to the samples indicated as *Protocol* in Figure 2.4

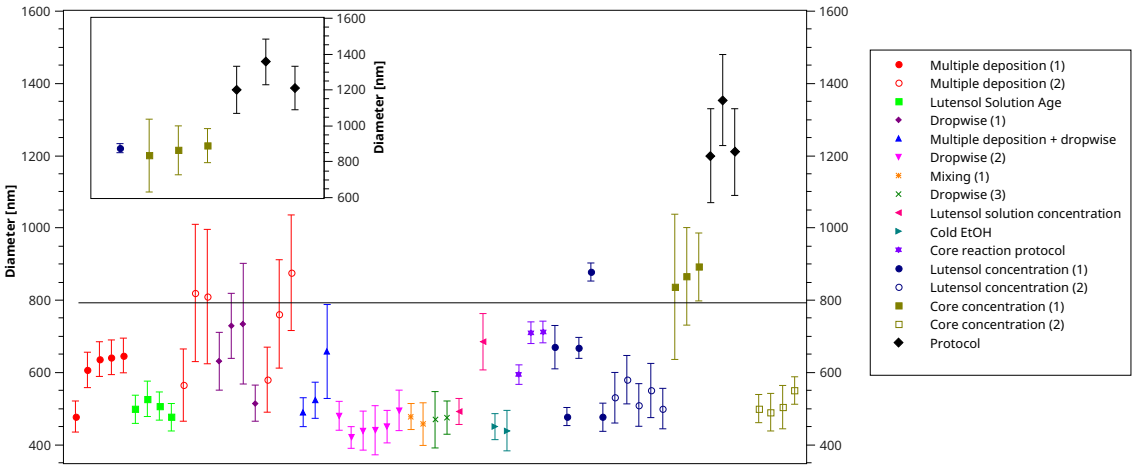

Figure 2.4: **Titania core-shell bead sizes** – Diameters of core+shell for the beads synthesised, as measured by SEM. The horizontal line highlights the threshold for acceptable beads, at about 800nm. The inset zooms on the successful samples that were used for the silica shell growth.

I obtained shells thicker than 70nm using a 3 steps multiple deposition, a drop-wise injection and low concentration cores. But in all these cases the results were not reproducible. Moreover, these samples presented clusters and second nucleations. Only by using the protocol reported above, I was able to achieve a consistent and reproducible growth of $\sim 1\mu m$ particles.

I identified two major reasons for the success of the reaction:

- the use of 10ml of Lutensol solution. In fact, in the original paper from Demirors *et al.* [89] a 1ml solution was suggested, but we observed that using a small amount of solution introduced an indetermination in the Lutensol-water ration. The relative error is bigger when pipetting 0.04 ml in 1 ml of water than it is when larger quantities are used;

- the slow injection of cores. This enables the surfactant to create a favourable surface for the growth of the titania shell on the anatase titania.

I performed a total of 60 reactions for the growth of the titania shell, and obtained 6 samples with target shell size and few second nucleations and clusters. Despite the low success rate overall, it is worth noting that of 3 out of 3 samples were successfull when using the described protocol at the end of the collaboration in Tuebingen.

SILICA SHELL SYNTHESIS The standard recipe for growing silica microsphere was set by Stöber [95] in 1968, and the same principles were here applied to grow silica shells.

I dispersed 0.25 ml of titania core-shell beads in a solution of water (600μl), ethanol (40 μl) and ammonia (50 μl of amonium hydroxide 30% from Sigma-Aldrich). After 30 minutes in bath sonication at 11° C , I added 97μl of surfactant solution. The surfactant solution consists of 80mg of cetyltrimethylamoniumbromide (CTAB) from Sigma-Aldrich in 0.6ml of ethanol and 1.34ml of milli-Q water. I left the mixture with the cores and the surfactant for 30 minutes in bath sonication at 11° C . After the sonication, I added 2μl of silica precursor, tetraorthosilicate (TEOS) from Sigma-Aldrich, to the mixture and left it for 4 hours while being magnetically steered.

At the end of the reaction time, I cleaned the beads by centrifugation (5 minutes 3000 rcf). I washed the pellet in a solution of 1.5g ammonium nitrate (Sigma-Aldrich) and 100 ml of ethanol, and centrifugated two more times. The washing solution broke the ammonia bonds cleaning the beads from the reagents. After the second centrifugation, I washed the beads in ethanol to remove the ammonium nitrate. Finally, I dried the beads in a furnace at 100° C and calcinated them for 1 hour at 500° C . During calcination, the silica diffuses into the titania shell, preventing the transition to the anatase phase.

I performed 12 reactions for the growth of the silica shell. Only 1 sample showed a successful growth of silica, indicating that this reaction still requires improvements. Limited time during the collaboration in Tuebingen prevented me from performing more reactions.

2.3.3 MORPHOLOGICAL CHARACTERISATION

Each sample was morphologically characterised by use of a Scanning Electron Microscope Hitachi S-800 with Back Scattering detector. To prepare the sample for scanning electron microscopy (SEM) microscopy, I deposited the beads on a metallic place, and once the ethanol was evaporated, I coated the plate with a thin film of 20-25 nm of gold by sputtering.

The particles size was calculated by applying a binary map to the SEM images, followed by segmentation (to separate clusters of beads). The particles analysis tool in *Fiji* software returned the area of the identified beads. From the area, I calculated the diameter, aggregated the data and calculated the statistics with the software *qtiplot*.

All the reactions for the core synthesis were successful. In Figure 2.5, a representative SEM picture is shown. Figure 2.6, instead, provides a representative picture of titania-shell beads samples. Finally, Figure 2.7 shows the successful sample with χTiO_2-αTiO_2-SiO_2 core-shell-shell beads.

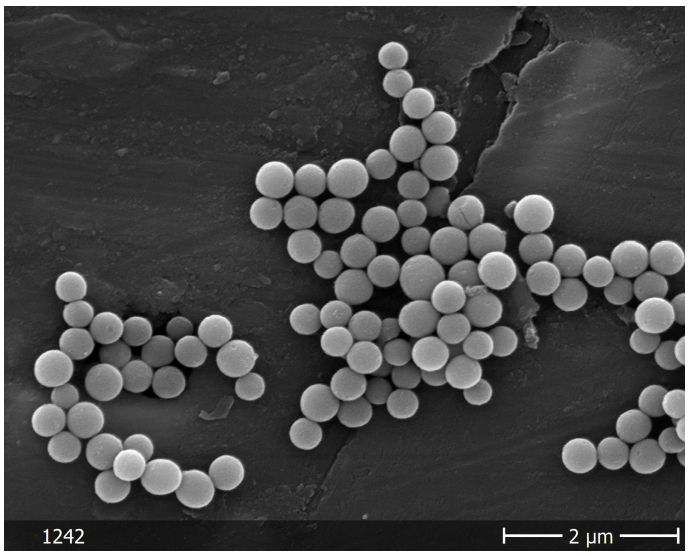

Figure 2.5: TiO_2 **cores** – SEM picture of titania cores as synthesised

More interestingly, I have found some SEM images where microspheres had broken shells, Figure 2.6(b), where the core-structure of the final titania core-shell bead could be observed. It is also worth noticing that the spheres have a rough surface: this property helps the diffusion of silica in the shell for the growth of the outer anti-reflective coating.

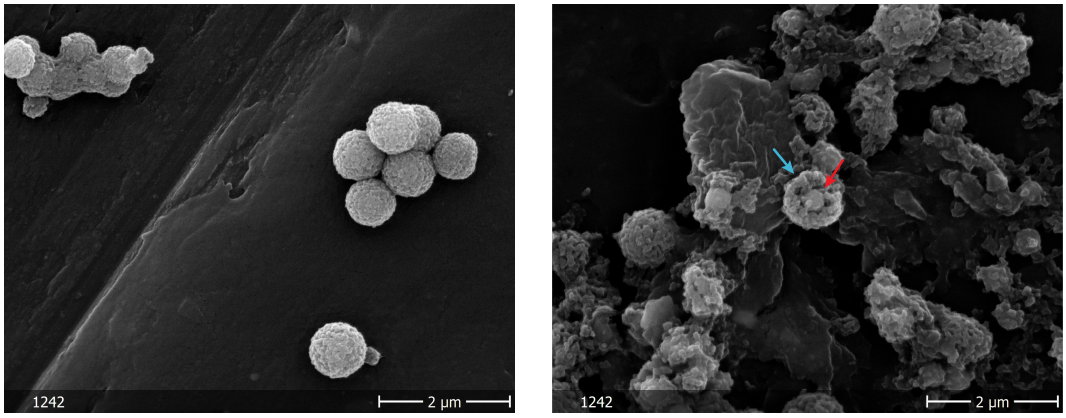

(a) (b)

Figure 2.6: χTiO_2-αTiO_2 **core-shell beads** – (a) SEM picture of a sample with a successful growth of αTiO_2 shell. (b) Another image of αTiO_2 core-shell beads, where a broken shell showd the anatase titania core inside.

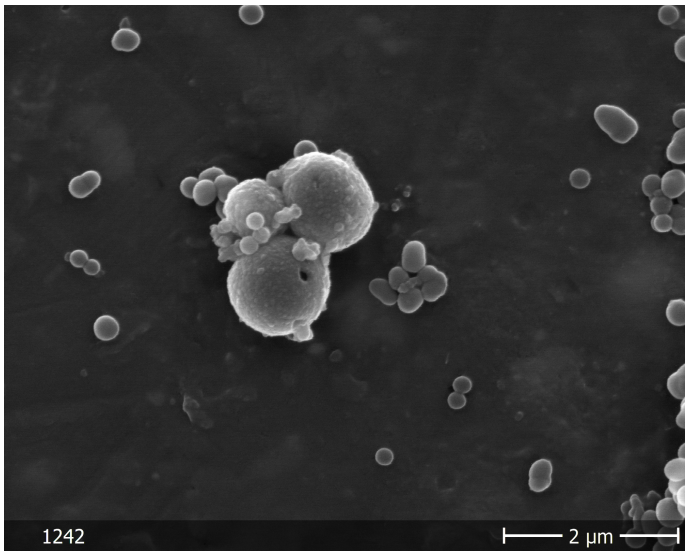

Figure 2.7: χTiO_2-αTiO_2-SiO_2 **core-shell-shell beads** – SEM image of titania-silica core-shell-shell microbeads. The small irregular particles visible are identified as silica second nucleations.

2.4 METHODS: SYNTHESIS OF TITANIA BEADS BY M-FLUIDICS

Key to a successful reaction for the production of titanium dioxide was controlling the size and the aggregation of the grains of titanium dioxide (TiO_2) that were nucleated at the beginning of the reaction.

With the batch reaction reported in subsection 2.3.2, this was achieved by using titanium glycolate as precursor, since titanium glycolate has a slower reaction time than TBT.

Nevertheless, the TiO_2 used the faster reactant TBT, limiting the control on the reactions for the shell growth and leading to the reproducibility issues.

By studying TiO_2 colloids synthesis techniques [91, 93, 96–112], I designed a new synthesis procedure with the aim to obtain a more controlled reaction. I based my new procedure on the work of Shiba *et al.* [109, 110]: they used a milli-fluidics approach to achieve full control of the reaction. Similarly, I designed a reaction using a rudimentary and cheap milli-fluidic device.

Titanium tetraisopropoxide (TTIP) (0.183ml from Sigma Aldrich), another precursor for TiO_2, was diluted with 4.813ml isopropyl alcohol (IPA) (99% grade from Merk), and then mixed with an acqueous 5ml IPA solution (0.031ml water in 4.969ml IPA) by use of syringes pumps. The two solutions were flowed each in one arm of a Y-type junction with a volumetric flow of 9ml/min and then flushed in a 70cm long perfluoroalkoxy alkanes (PFA) tube of 2mm internal diameter. Thanks to the laminar flow in the tube, TTIP reacted with water only at the interface between the two reactants, where nanometric titania grains were formed and soon separated from each other by the flow. The reactants were poured from the tube to a 20ml IPA solution with additional 0.12ml water and 0.03 grams of octadecylamine (ODA) (from Sigma Aldrich), a surfactant to control the final shape of the beads. The mixture was left to react for 24h at room temperature under magnetic stirring; this allowed the grains of titania to aggregate into particles of desired size.

At the end of the reactions, I collected the colloids by vacuum filtration with a polytetrafluoroethylene (PFTE) membrane of pore size $200\mu m$, and then washed them with IPA. To remove the ODA on the microspheres, I further washed them in hydrochloric acid-ethanol solution (30% from Merk) under magnetic stirring for 1h. Finally, I vacuum filtered, washed and resuspended them in IPA.

The product of this first reaction are TiO_2 cores in an amorphous phase. To induce transition to the anatase phase, I cured them at 500 $^\circ$C in a furnace for 1h. After the calcination, I resuspended them in 10ml IPA and stored

SHELL COATING BY MILLI-FLUIDICS APPROACH The main advantage of the millifluidic approach is that the reaction for the titania shell is identical to the reaction for the

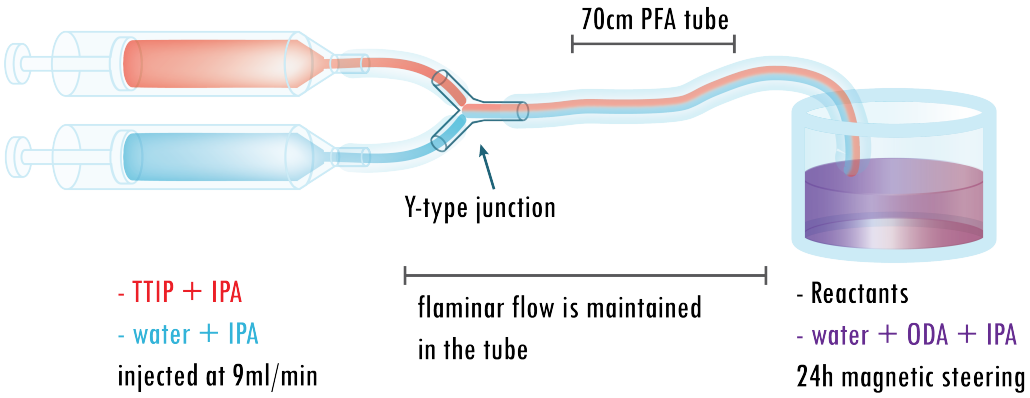

Figure 2.8: **Drawing of milli-fluidics TiO_2 reaction device** – Two mixtures with the reactants, titania precursor TTIP and water, are injected at a volumetric flow of 9ml/min into a y-type junction. They enter a 70cm long tube, where laminar flow is maintained. The laminar flow controls the output of the reaction: TTIP reacts with water producing nanometric titania grains that are soon separated from each other by the flow. The grains aggregate in the batch solution of ODA and water in IPA, where the reactant mixtures are poured in. The final solution is left to react for 24h under magnetic stirring.

cores. I used the same reactant and the same flow conditions, with the only difference that the IPA solution for the 24h reaction contains 5ml of anatase titania cores suspended in IPA.

2.4.1 MORPHOLOGICAL CHARACTERISATION

I morphologically characterised the samples with a Scanning Electron Microscope JEOL 6310 with back scattering detector. To prepare the sample, I deposited the beads on a carbon conductive tape attached on top of a SEM holder and, once the IPA was evaporated, I coated them with a thin film of 20-25 nm of gold-platinum by sputtering.

The reaction of TiO_2 cores was successful, with a diameter size of $586nm$ (Figure 2.9). The size of the cores reduced after calcination and the microbeads reached the target size of $450nm$, with variance smaller than 5%.

The core-shell spheres were less monodisperse than the cores. In fact, I measured three distinct sizes: almost non-coated calcinated cores ($460nm$), coated beads with shell thickness of ∼200 nm and coated beads with shell thickness of ∼800 nm (Figure 2.10).

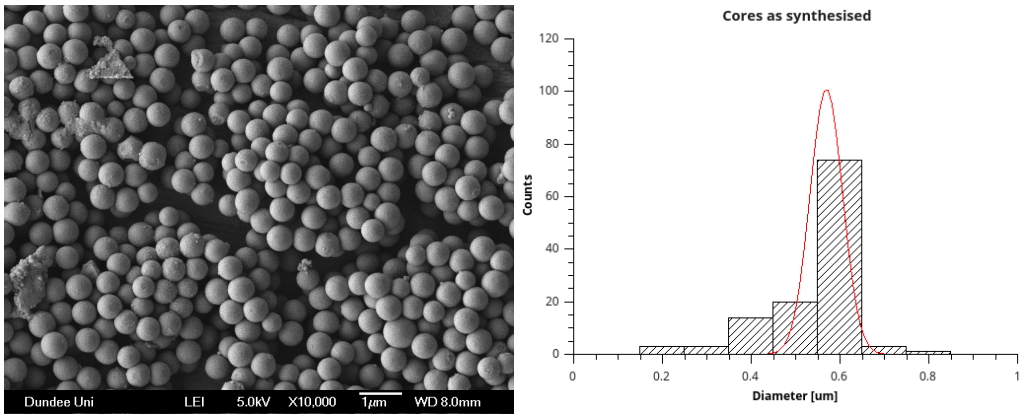

(a) (b)

Figure 2.9: χTiO_2 **microspheres synthesised by m-fluidic, before calcination** – (a) Example SEM image of the titania core. (b) Size evaluation of the SEM images shows that the produced cores match the target size.

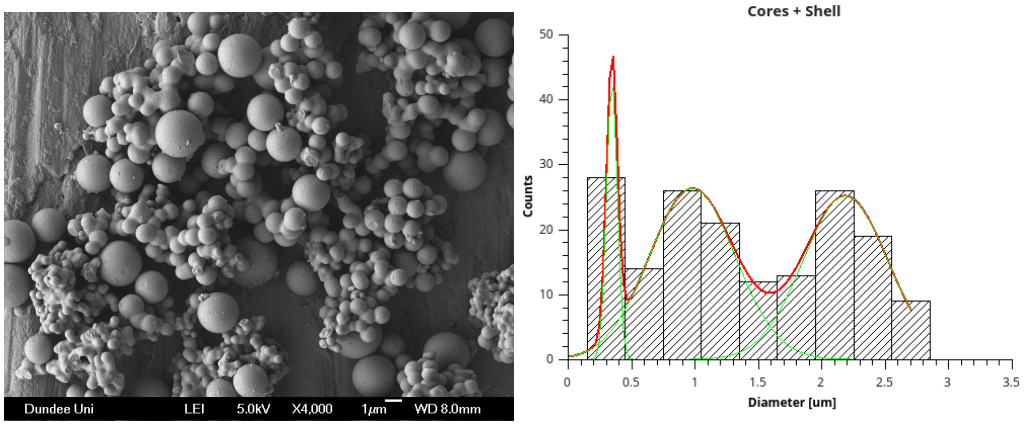

(a) (b)

Figure 2.10: χTiO_2-αTiO_2 **core-shell microspheres synthesised by m-fluidic** – (a) Example SEM image of the titania core-shell microspheres. (b) Size evaluation from SEM images; the first peak corresponds to non-coated calcinated cores, the second and third peak correspond to two different sizes of shell that have been synthesised on top of the cores.

Because the peaks at different sizes are well-resolved, the sample could be filtered with pore membranes of appropriate size, so that monodispersed samples with beads of $\sim 1\mu m$ and $\sim 2.2\mu m$ could be produced.

2.5 CONCLUSIONS

The introduction of custom-made probes for optical trapping initiated the development of a new generation of nanonewton forces optical tweezers. Antireflection coating on high refractive index material (i.e. TiO_2) was proved effective in term of forces generation, but it was difficult to reproduce and control.

With my work, I identified crucial parameters for the success of the reaction, such as the speed of injection of the cores in the solution mixture before the titania coating. At the end of my residence in Tuebingen, the adjusted protocol produced titania shells of target size, for all the reactions performed, despite the variance of the sample was not yet optimised.

Through optical simulation, I proved that adding an additional layer of silica to the core-shell χTiO_2-αTiO_2 structure solved the issue of trappability, with the variance in size resulting in a secondary problem. The silica synthesis to coat nanoporous titania, however, was poorly understood. I was able to produce a successful sample (the one used in the following chapter), but I failed to identify what parameters favour the growth of silica.

I also explored an alternative approach to the batch reaction. I proved that custom beads similar in size and material could be obtained by using a milli-fluidic synthesis. While the beads obtained through this milli-fluidic approach still lacked monodispersity, they had advantages compared to the beads processed through the batch reaction. In fact, I obtained beads of different size in one reaction (Figure 2.10) – a characteristic useful to investigate the properties of high refractive index microspheres of bigger size.

In addition, it is reported that a composite silica-titania material can be made using a similar milli-fluidic reaction [113, 114]. A silica-titania compound is worth exploring because its refractive index could be tuned by choosing different relative amounts of silica and titania: a tunable refractive index could further improve the design of coating materials. For example, it makes possible to design a particle with multiple coating layers, each with a gradually changing refractive index with the aim to improve anti-reflection. The final advantage of this reaction resides in the fact that the same chemicals are used for both the cores and the shell reactions, making the process easier to understand and

to reproduce, and more cost effective. To conclude, it is highly recommended to explore the milli-fluidics approach further. I tested the reproducibility of these reaction only for the production of cores, and more studies are needed for the shell coating.

In the next chapter, I will show how I characterised the trapping properties of the core-shell-shell beads produced by batch reaction in Tuebingen and confirmed the expected enhancement in trapping. The beads produced by milli-fluidics approach were not optically characterised because of limited time.

3

FORCE MEASUREMENTS WITH HIGH STRENGTH OPTICAL TWEEZERS

The synthesis of optical tweezers probes with high refractive index material is challenging, but I have proved in the previous chapter that it can be optimised and improved. However, there is still a question to answer: do these probes really generate high stiffness for optical tweezers?

Forces $\sim 1.2nN$ were measured by Jannasch *et al.* when employing χTiO_2 coated with αTiO_2 [25]. I have produced both χTiO_2-αTiO_2 core-shell and χTiO_2-αTiO_2-SiO_2 core-shell-sheres: do these spheres behave as it was reported in literature and do the silica coated have a real advantage on the titania core-shell ones?

To answer these questions, I have evaluated the optical tweezers stiffness for both types of probes and reported methods and results in the following sections.

3.1 STIFFNESS EVALUATION OF TITANIA CORE-SHELL MICROSPHERES

I performed the evaluation of the trap stiffness for χTiO_2-αTiO_2 core-shell beads while at the University of Tuebingen, using self-calibrating back focal plane interferometry (section 1.6) with the optical tweezers set-up described in literature [25].

SAMPLE PREPARATION I sampled 10 μl of the mixture with the αTiO_2-TiO_2 core-shell microspheres and left them at 70 $^\circ$C to evaporate the ethanol. Once the beads were dry, I resuspended them in milli-Q water with a dilution factor 10:1000. To confine the beads-water mixture, I created a channel by melting two slices of parafilm between two coverslip glass slides of thickness no.1. I injected the mixture in the channel and sealed everything with nail polish.

COLLECTION AND FITTING OF PSD I measured the displacements of each bead 10 times for a duration of 1 second, using a sampling frequency of 65536 Hz and driving the stage with an oscillation frequency of 32 Hz. I calculated the PSD for each independent measurement and then averaged all the spectra together. Finally, I fitted each spectra with a modified version of the Matlab *Tweezerscalib* [115, 116] that included the self-calibration calculations.

Table 3.1 reports the measured values for trap stiffnesses in the x- and the y-axis. An example of measured power spectrum is shown in Figure 3.1.

Bead ID	κ **[pN/(nm.W)]**	
	k_x	k_y
TC17S2-b01	3.0 ± 0.1	2.6 ± 0.1
TC17S2-b02	4.4 ± 0.2	4.6 ± 0.2
TC17S2-b03	3.7 ± 0.1	2.5 ± 0.1
TC17S2-b04	2.6 ± 0.1	4.0 ± 0.7

Table 3.1: **Trap stiffness for χTiO_2-αTiO_2 core-shell beads** – Results obtained applying the self-calibrating back focal plane interferometry method. The laser power in the trap was 12mW and the oscillation frequency 32Hz.

The values observed are in agreement with the first observations of high strength tweezers with photonically structured probes [25]. Similarly to their study, and due to the size variance in the sample, many bead were not trappable. The four beads reported were the only ones for which I was able to obtain 10 different measurements in the limited time I collaborated with the Nanoscience group in Tuebingen.

3.2 STIFFNESS EVALUATION OF TITANIA-SILICA CORE-SHELL-SHELL MICROSPHERES

I evaluated the stiffness χTiO_2-αTiO_2-TiO_2 core-shell-shell microspheres when I was back in Dundee, after the collaboration with the University of Tuebingen.

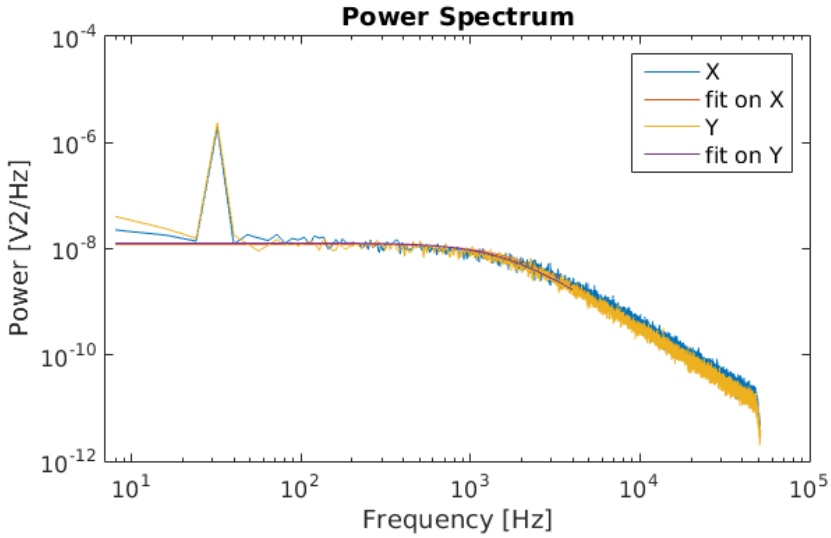

Figure 3.1: **Example of power spectrum for χTiO_2-αTiO_2 core-shell beads** – Example of power spectrum for the x- and y-axis. The peak at 32 Hz is the calibration peak. Both the curves refer to the same bead (TC17S2-b02 in Table 3.1).

EXPERIMENTAL SET-UP AND METHODS

I measured the trap stiffness with a standard set-up of optical tweezers (Figure 3.2), obtained by focusing a laser with 1.5W output power at 1064 nm (Laser Quantum Ventus 1064) by an oil-immersion microscope objective (Nikon 100x Apochromat with Numerical Aperture NA=1.45) to a diffraction-limited spot of $\sim$ 360nm.

The scattered light was collected by a long working distance objective (Mitutoyo NA=0.55 100x) onto a quadrant photodiode (QPD, Hamamatsu, G6849) to perform back-focal-plane interferometry. The signal from the QPD was collected with a National Instrument Acquisition Card (DAQ) and saved by a custom LabView software. The displacements for each bead were measured 20 times for the duration of 1 second. The power spectra were calculated for each measurements and averaged to increase the signal-to-noise ratio.

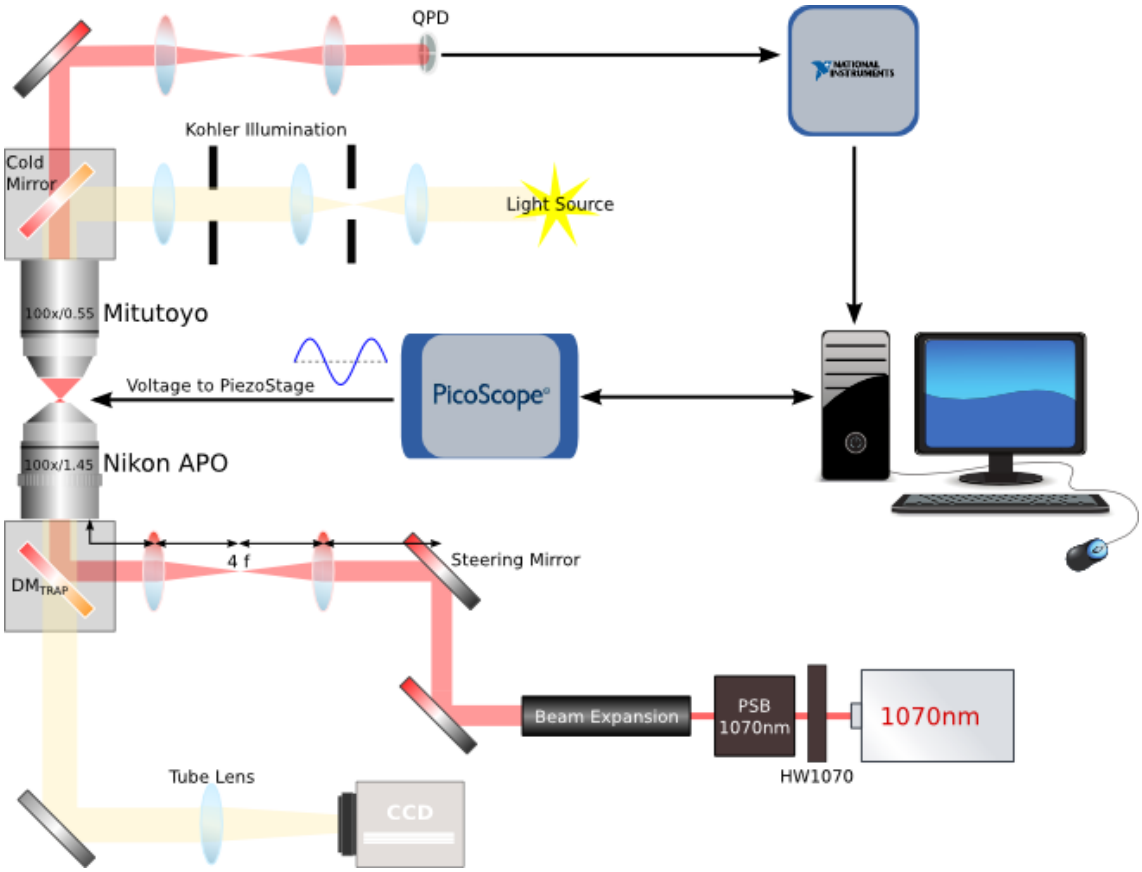

Figure 3.2: **Experimental set-up of optical tweezers used for stiffness evaluation** – A 1064 laser is expanded to a diameter $\sim 8mm$ and focused by an oil immersion microscope objective Nikon 100x Apochromat with NA=1.45. An air immersion objective redirects it onto a QPD placed in a plane conjugated with its back focal plane. The signal from the QPD is collected by a DAQ and send to the computer. The sample is illuminated in bright field with a Kohler illumination and imaged onto a CCD camera. The sample holder is moved through a Thorlab piezo-stage receiving an external input from a PicoScope.

SAMPLE PREPARATION Similarly to the sample preparation of the titania core-shell beads, I sampled 10 μl of the mixture with the χTiO_2-αTiO_2-TiO_2 core-shell-shell microspheres and left them at 70 °C to evaporate the ethanol. Once the beads were dry, I resuspended them in milli-Q water. I chose a 1:1000 dilution because the sample presented secondary nucleations of silica: in a more diluted sample, the probability to trap the second nucleation was lower. I finally placed 20μl of the beads-water mixture between two glass coverslip slides thickness no.1, separed by a vinyl spacer. The thickness of the vinyl spacer was 80μm, as measured through a profilometer.

CHOICES FOR THE SELF-CALIBRATION PARAMETERS The samples were placed on a Thorlabs MAX302/M NanoMax piezoelectric stage, controlled by a Thorlabs MDT630A 3-Axis piezo controller. The piezo controller could receive an external signal from the function generator channel of the PicoScope (5000 Series). The PicoScope acted as a function generator for the sinusoidal signal required for the self-calibration technique.

I chose an oscillation amplitude of 150 nm that would not affect the thermal spectrum: increasing amplitudes were sampled until the bead displacements distribution was distorted from a Gaussian shape, then the larger value that did not create the distortion was chosen.

The driving frequency was selected taking into account the perturbation penetration depth ξ of the shear wave into the fluid [83]:

$$\xi = \sqrt{\frac{\zeta}{\pi f_{drive}}} \tag{3.1}$$

where the ζ is the kinematic viscosity of the medium and f_{drive} is the oscillation frequency. The ratio d/ξ (where d is the height of the sample chamber) should be smaller than 1 to minimise disruption of the flow in sample. For water and a frequency of 32 Hz at room temperature, $\zeta \sim 100\mu m$. Since the vinyl spacer thickness is $80\mu m$, the sample was safe from perturbations when chosing $f_{drive} = 32$.

FITTING OF THE POWER SPECTRA I modified the *Tweezercalib* toolbox in Matlab to search for a peak at the f_{drive} provided by the user, to save the value of the spectrum at that frequency and to remove the peak so that the rest of the thermal spectrum could

be fitted by the original toolbox. I also included a feature that allows to remove other unwanted peaks generated by noise.

After the fitting, I obtained the trap stiffness by including the fitted values for the diffusion coefficient (in volts) and for the corner frequency in Equation 1.19 and Equation 1.21.

CALIBRATION TECHNIQUE VALIDATION

An older version of the set-up described in Figure 3.2 was not originally intended for self-calibration techniques. Given it was the first time I implemented this technique for this set-up, I considered it necessary to validate the reliability of the method. For this purpose, I first calibrated commercial silica beads (Figure 3.3). In fact, commercial silica beads have a monodisperse distribution in size: by measuring the calibrated spectra, I could calculate the size of these beads experimentally. If the calibration technique was valid and it was true that the size variation for the commercial beads was low, then their ratio would be close to 1.

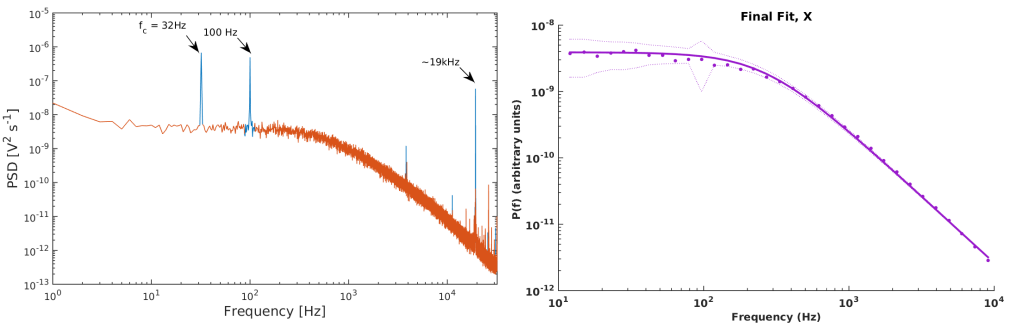

(a) (b)

Figure 3.3: **Calibration of commercial silica beads** – In (a), it is an example of power spectrum immediately after a measurement (in blue), featuring the calibration peak at 32 Hz and some parasitic peaks. These additional peaks come from room and electrical noise and they are removed prior to the fitting, leaving a cleaned spectrum ready to be used for the fitting (in orange). In (b), example of fit of the brownian background as it is calculated by the *Tweezercalib* toolbox.

When I performed this validation, I found that the ratio between the bead radii measured with the calibration technique and the ones provided by the producer were indeed close to 1, as shown in Figure 3.4. This result confirmed that I could trust the

self-calibration technique I implemented in Dundee and I could use to study beads of unknown size.

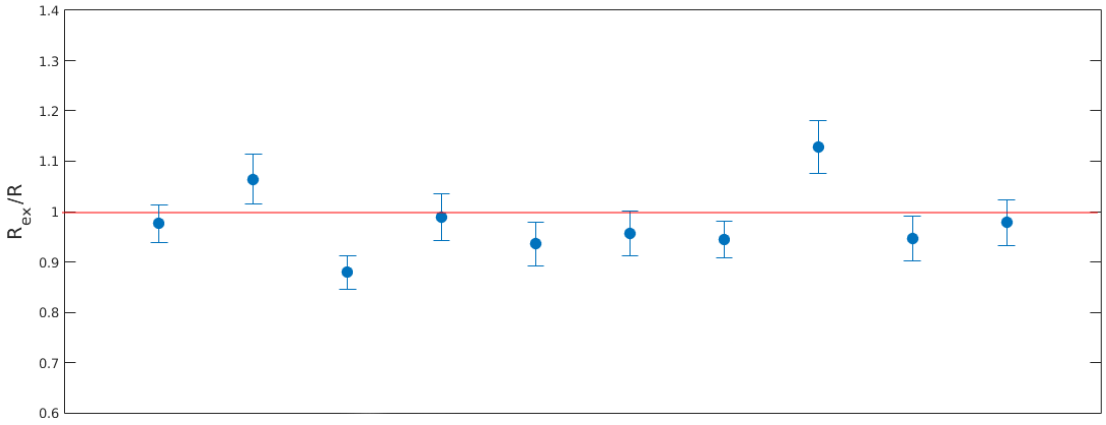

Figure 3.4: **Validation of self-calibration technique** – Ratio between the radius of the beads obtained through calibration (R_{ex}) and the one provided by the beads producer (R); the calibration technique is accured when this ratio is close to 1. The laser power in the sample was 100 mW.

For this experiment, I chose commercial silica beads with a diameter of $1.86\mu m$ from Bangs Laboratories that I prepared in the same way I prepared the samples for titania-silica beads. Thanks to the fact that the commercial silica size was the closest to the custom beads, I could later compare their measured trap stiffness. The average trap stiffness for the commercial silica beads obtained through this measurement was $0.45 \pm 0.21 pN/(nm \cdot W)$.

3.2.1 STIFFNESS EVALUATION FOR CUSTOM PROBES

Once I validated the use of the self-calibrating technique, I measured the stiffness for the custom-made χTiO_2-αTiO_2-SiO_2 beads. Their average trap stiffness was $1.15 \pm 0.35 pN/(nm \cdot W)$, nearly 2.5 times larger than the average stiffness for commercial silica beads. Table 3.2 reports the values of trap stiffness measured for the individual beads measured.

An example of spectrum for the silica coated titania beads is reported in Figure 3.5.

Bead ID	κ **[pN/(nm.W)]**		D [μm]
	k_x	k_y	
TC19S1Si2-b01	1.2 ± 0.1	1.1 ± 0.1	1.6 ± 0.2
TC19S1Si2-b02	1.3 ± 0.2	0.9 ± 0.2	1.5 ± 0.2
TC19S1Si2-b03	0.9 ± 0.1	1.0 ± 0.1	1.6 ± 0.2
TC19S1Si2-b04	1.9 ± 0.1	1.8 ± 0.1	1.4 ± 0.2
TC19S1Si2-b05	1.5 ± 0.2	1.4 ± 0.2	1.3 ± 0.2
TC19S1Si2-b06	1.2 ± 0.1	1.3 ± 0.1	1.4 ± 0.2
TC19S1Si2-b07	1.1 ± 0.1	1.0 ± 0.1	1.7 ± 0.2
TC19S1Si2-b08	1.4 ± 0.2	1.2 ± 0.2	1.3 ± 0.2
TC19S1Si2-b09	0.7 ± 0.1	0.7 ± 0.1	1.6 ± 0.3
TC19S1Si2-b10	0.8 ± 0.1	0.7 ± 0.1	1.7 ± 0.3

Table 3.2: **Trap stiffness for χTiO_2-αTiO_2-SiO_2 core-shell-shell beads** – Results of the calibration measurements. The laser power in the trap spot was 100 mW for beads b01-04, 20 mW for beads b05-08 and 3 mW for beads b09-b10.

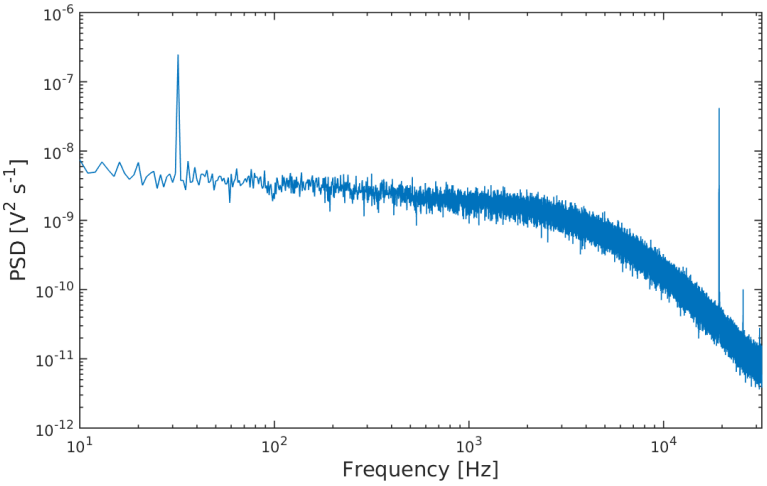

Figure 3.5: **Example of power spectrum for χTiO_2-αTiO_2-SiO_2 beads.** – Example of power spectrum for a silica coated titania bead. The peak at 32 Hz is the calibration peak. The laser power in the sample was 100mW.

3.3 CONCLUSIONS

The analisys for the trap stiffness of the photonically structured probes (synthesised according to subsection 2.3.2) shows that:

- the trap stiffness for χTiO_2-αTiO_2 core-shell beads measured with the optical tweezers set-up in Tuebingen was in good agreement with the values reported in literature that were measured with the same device [25]. I also confirmed that not all the beads could be trapped, as expected by optical simulations;
- the trap stiffness for χTiO_2-αTiO_2-SiO_2 core-shell-shell beads measured with the optical tweezers set-up in Dundee was lower than the one measured in Tuebingen. However I was able to trap more beads, despite their size variation;
- the trap stiffness measured for χTiO_2-αTiO_2-SiO_2 core-shell-shell beads was 2.5 times larger than the one for commercial silica beads measured with the same device.

Upon observing these results, I wanted to investigate why I obtained a lower trap stiffness for the silica coated spheres compared to the titania core-shell. In fact, the silica-titania core-shell-shell batch was obtained by coating with silica the same sample of titania core-shell I analysed in Tuebeingen. Therefore, one would expect to find the same trap stiffness. The main difference between the two measurements was the optical tweezers used: for the titania core-shell I employed the optical tweezers in Tuebingen, while for the silica coated beads I used the ones in Dundee.

In the original simulations, I used a numerical aperture and a filling ratio that matched the description of the Tuebingen set-up. Therefore, I run new simulations matching these parameters to the set-up in Dundee, NA = 1.40 and overfilling ratio of 1.3. The results from this new simulation showed that both filling ratio and numerical aperture are crucial for photonically structured beads: with the parameters of the Dundee set-up, the optimal size to achieve that highest trapping stiffness is shifted from the actual size of the synthesised beads. This explained why by measuring in Dundee beads that were optimised for the set-up in Tuebingen I obtained lower trap stiffness. Furthermore, the new simulation agrees with the measured values (Table 3.2).

It is worth mentioning that I failed to trap any of the χTiO_2-αTiO_2 core-shell beads when using the Dundee set-up. This proved that the additional silica coating improves

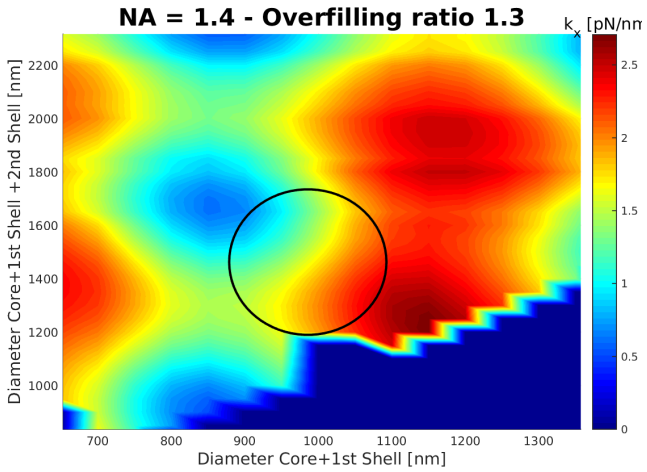

Figure 3.6: **Optical simulation of anti-reflective SiO_2 coated microspheres for the optical tweezers set-up in Dundee**, using effective NA=1.4 and overfilling ratio. – Simulated values for trap stiffness (in the y direction of bead motion) for a core size of 500nm, while varying the first shell thickness (x-axis) versus total size (y-axis). The circle highlights the sizes of the probes as synthesised; The simulated values are in good agreement with the values measured for the trap stiffness (Table 3.2).

the robustness of custom probes: if different set-ups are used, the maximum achievable force is reduced but the probes are still usable.

Finally, the custom probes outperformed commercial silica beads. I measured an average trap stiffness of 1.15 ± 0.35 pN/(nm $\cdot$ W) for beads with diameters $1.3 < D < 1.7\mu m$ (Table 3.1); this trap stiffness is 2.5 times higher than the 0.45 ± 0.21 pN/(nm $\cdot$ W) measured for commercial beads of comparable sizes (1.86μm SiO_2 beads from *Bangs Laboratories*). A similar proportion was found in literature when comparing titania core-shell bead with silica beads of similar sizes [25], confirming that the main difference resided in the used set-up rather than a different behaviour from the beads themselves.

PERSPECTIVES The improvement in the trap stiffness obtained through the use of photonically structured probes opens the possibility to explore new biological phenomena happening at nanonewton forces. However, I showed in this chapter that high trap stiffness is influenced by the set-up in use and to synthesise beads of different sizes to match one's set-up would need more insight in the chemical reactions for the production of these probes.

Furthermore, the synthesis of these probes still needs improvement regarding reproducibility and monodispersity of the sample. One approach would be to further explore the milli-fluidics methodology I introduced in the previous chapter. Long term, however, it would be exciting to combine different approaches to generate high strength photonic tweezers. Many of the techniques to increase the trap stiffness in Chapter 2 are not mutually exclusive; for example, it would be possible to combine structured scattering with larger photonically structured beads.

While it is true that a whole new set of biological phenomena would become accessible once nanoNewton-capable optical tweezers will be easier to reproduce and set-up, I will show in the next chapter that these probes can already be used for preliminary studies in biology.

4

OPTICAL TWEEZERS FOR CELL BIOLOGY

Over the years, optical tweezers have been widely applied in cellular biology. One of the very first applications by Ashkin himself was the trapping of E. Coli, red blood cells, organelles in spirogyra cells, protozoa and organelles inside protozoa [28, 30]. Besides manipulation of single cells, optical tweezers can contribute to the study of the cytoskeleton, the dyanamics of cell motion and adhesion properties of cells.

While genetic engineering represents an advantageous way to study cells –the knock-in/knockout of the genes that regulate the cytoskeleton can provide insights on its dynamics– scientists should rely on a physics approach to gain information about the forces involved in cell motion. Optical trapping is one of these physical approaches, but it is often limited by the fact that commercial optical tweezers are capable of applying forces of few hundred of picoNewton at most.

4.1 A POWERFUL TOOL FOR BIOLOGISTS

The forces involved when a cell crawls on a substrates are a good example of why biophysicists have attempted to build high strength tweezers: summing the individual contributions of the different components of the cytoskeleton results in forces of few nanonewtons [117], that can only be accessed by photonically structured probes if one wants to use optical tweezers.

To understand how optical tweezers can be employed in cellular biology, I have reviewed how they have been used in the past. Their applications can be grouped in two main categories: *manipulation of cells*, including positioning,sorting and assembling of cells; and *force measurement*, including measurements of deformability, membrane tension and adhesion.

CELL MANIPULATION The forces applied by standard optical tweezers are sufficient to confine a cell against thermal fluctuations in a medium. Cells can be held in specific

positions in order to measure their properties by other techniques, e.g. by performing spectroscopy or X-ray imaging [118]. By using this approach, different properties of bacterial species [119], lymphocytes [120] and cancer cells [121] were studied.

It is also possible to transport single cells to different locations to form cell groups [122] or to study cellular response to different environments [58]. With multiple optical traps, one could create 3D structures of cells [123, 124] and biofilms [46].

Finally, optical manipulation has been used to make quantitative observations on phenomena at the cellular level, for example the interaction between cells and extracellular vesicles [50] or the time required for cell-cell adhesion to occur [125].

MEASURING FORCES More interestingly, optical tweezers can be employed to apply/measure forces on/to cells, thus extracting information on their mechanical properties and dynamics.

For example, optical tweezers can provide information on *cell membranes*. They were used to study the elasticity of human red blood cells by directly stretching the cells with two or more trapped probes [52, 126, 127]. Elasticity of the plasma membrane and the force required to separate it from the underlying cytoskeleton was measured by tether extraction with optical tweezers [18, 106, 128]. A cell elasticity assay was also conducted by mimicking AFM studies, with a trapped microsphere applying few pN of force by indentation on a cell[129]. The range of forces for these elasticity studies lied in the range of 1-400 pN.

It is also possible to optically trap elements presents inside the cell, like lipids granules and organelles. There have been studies on displacing the cell nucleus [130] and attempts at measuring the forces to dislocate granules in the cytosol [59]. With these experiments, however, it is often required to make assumptions on the properties of the cytosol, making a direct force measurement less reliable [59].

Finally, optical tweezers could be used to study crawling mechanisms. For example, tweezers were employed to measure the traction forces of neuron cells [51] in a range of 40-150pN, or to direct thier axon growth with only few tenths of pN [55] . Adhesion

mechanisms in yeast cells [131] and fibroblast cells [49] were also studied with optical tweezers operating in the range of 1.4-100pN.

An interesting approach in this regard is the study of the ell protrusion edge by Yang *et al.* [56]. In their experiments, an optically trapped microsphere acted as a load for the leading edge of a leukemia cell moving in a chemotactic environment [45, 56]. The cell pushed the load until the force of the leading edge equaled the other forces acting on the trapped microsphere: by knowing the trap stiffness and the drag force, the author could calculate that the force of the protrusion edge was around 100-300pN [56].

All the examples of applications I have mentioned operated at a maximum of few hundred of pN, and in some cases the authors of those studies could only measure lower limits of the cell forces because they could not apply higher forces with their tweezers. Tweezers capable of nanonewton forces would overcome this limit and perform experiments involving higher forces.

4.2 CUSTOM PROBES FOR CELL BIOLOGY: SURFACE FUNCTIONALISATION

The first step towards employing photonically structured probes for biological applications is to verify that these probes can be functionalised as needed. I studied the adhesion properties of T lymphocytes, as a good case-study for the functionalisation of the custom probes.

T-CELLS

Thymus leukocytes, or T-Cells, are one of the primary types of lymphocytes and represent a crucial element of the cell-mediated immune response. The efficacy of T-Cell response is linked to their ability to adhere to endothelial cells when required. The adhesion mechanism is regulated through the interaction of lymphocyte function-associated antigen 1 (LFA-1) and intercellular adhesion molecule 1 (ICAM-1) [132, 133].

This type of cells represented a good case study to investigate the functionalisation properties of the custom silica-titania probes. In fact, I had access to a reservoir of experiments that had been performed in the group of David McGloin at the Univesrity of Dundee to compare with my new experiments. The original intent by McGloin *et al.* was

to quantify the local forces involved in single molecules adhesion events between ICAM-1 and LFA-1 with optical tweezers [134]. For this reason, they needed to functionalise the commercial silica beads used in the their experiment with ICAM-1, put them in contact with an activated lymphocyte stuck on a coverslide. They would then measure the resistance, if an adhesion event had happened, when pulling the beads away. Figure 4.1 portraits a schematics of their experiment design.

4.2.1 METHODS

Following the same experiment design as the one reported in Figure 4.1, I attempted to reproduce the results by McGloin *et al.* by using commercial silica beads and then repeated the measurements using custom χTiO_2-αTiO_2-SiO_2 probes to verify whether they could be functionlised, preferably using the same protocols used for commercial probes.

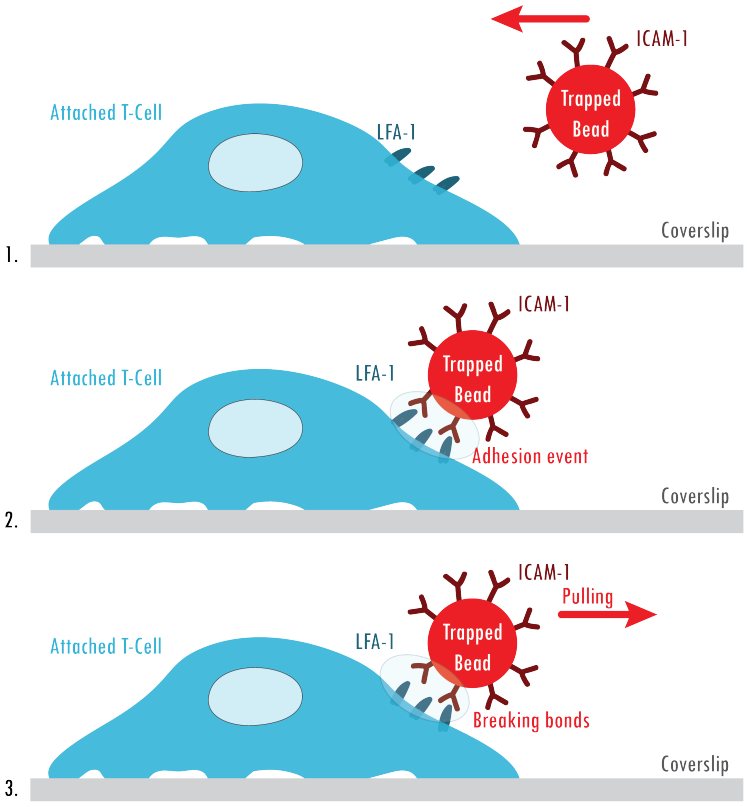

Figure 4.1: **Experiment design for T-Cells adhesion measurements** – (1) A T-Cell is attached non-specifically to the substrate and a trapped bead functionalised with ICAM-1 is moved toward the cell (red arrow). (2) the ICAM-1 bonds with LFA-1. (3) Finally the bead is pulled away (red arrow) and the force required to break the bonds between the cell and the bead is measured.

T-CELLS SAMPLE PREPARATION The T-Cells samples were prepared by Dr. Spinelli, staff member of the *Cell Signalling and Immunology* division at University of Dundee. T-Cells were extracted from the spleen of control mice. Collected splenocytes were incubated with 2C11 peptide for activation at 37° C with 5% CO_2. Interleukin 2 (IL2) and Interleukin 12 (IL12) were added to burst activation and to reproduce physiological conditions. T-Cells were washed after 1-2 days, and then re-suspended in fresh media with IL2. The cells were counted daily and kept at a concentration of 0.5 millions/ml. I used the cells on days three, four and five after activation at a concentration of 1 million/ml by depositing the suspension with T-Cells on a microscope coverslip. I waited 30min for the cells to settle down and stuck on the substrate and then started the experiments.

4.2.2 RESULTS

Functionalisation of the custom trapping probes

I extended the ICAM-1 functionalisation protocol for commercial beads to χTiO_2-αTiO_2-SiO_2 composite bead. The protocol required the beads to be washed twice in *Phosphate-Buffered Saline solution* and left in incubation at 4° C in 500μl of the Phosphate-Buffered Saline solution with added 2μg/ml ICAM-1. After collection, they were washed three times by being centrifuged at 5000 rcf for 1 min and then resuspended in fresh saline solution.

When using this protocol for the composite beads, I observed the formation of beads clusters. I overcame this problem by centrifugating them at lower speed for a longer time, i.e. 3000 rcf for 5 min: by using these parameters the clusters were reduced but the pellet formed at the end of centrifugation was softer so that some beads were lost during re-suspension.

To verify that the beads were functionalised, I brought them in contact with T-Cells and observed whether or not the beads would remain attached to the cell (see Figure 4.2). I used both ICAM-1 coated and uncoated microspheres, either commercial or photonically structured, and compared the percentage of them that adhered to the T-Cells [135].

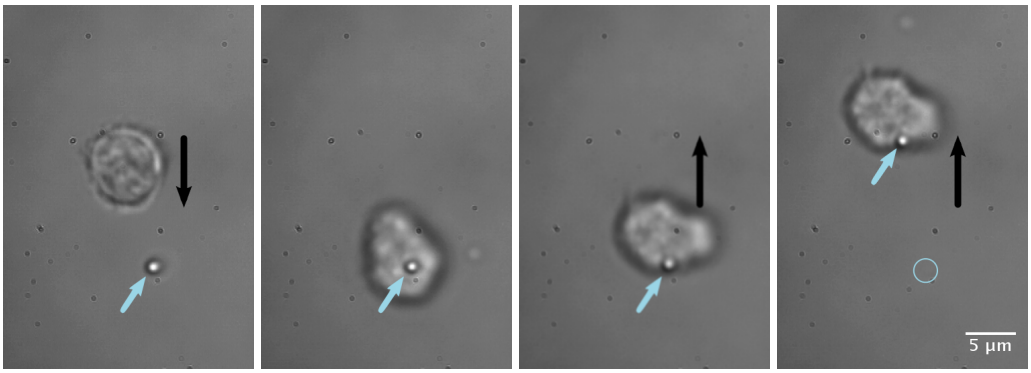

Figure 4.2: **Functionalisation of χTiO_2-αTiO_2-SiO_2 beads** – Example of the interaction between a T-Cell and a functionalised bead. The blue arrow indicates the custom bead, the black arrow indicates the direction of motion of the cell in regard to the bead. In the last panel on the right, the blue circle highlights the position of the trap, after the bead has left because attached to the cell.

I found that the photonically structured probes behaved as commercial probes (Table 4.1), suggesting that the protocols available in literature for the functionalisation of commercial probes can be easily extended to custom materials and surfaces like titania-silica composites.

	ICAM-1	**Uncoated**
Commercial beads	21.9%	<1%
χTiO_2-αTiO_2-SiO_2 **beads**	26.6%	<2%

Table 4.1: **Percentage of beads that have shown interaction with T-Cells** – As measured on 87 cells for commercial beads and 79 for custom beads.

Measuring adhesion forces

By functionalising the custom beads, they could be used to measure the forces involved in the adhesion events between ICAM-1 and LFA-1. McGloin *et al.* measured forces in the order of few pN by using commercial silica beads, and it should be possible to reproduce the experiments by using the custom probes and reducing the trapping laser power needed to achieve the same forces.

However, I did not perform force measurements as per McGloin's study: despite following the same protocol, the T-Cells showed poor non-specific adhesion on the substrate, and this was a critical requirement of the experiment. On visual inspection, less than 5% of the cells were firmly stuck on the substrate, with the remaining cells vibrating of brownian motion: I could measure only stuck cells, because floating cells were trapped by the tweezer without opposing resistance to measure the forces. Such a small percentage of cells adhering on the substrate did not constituted a representative samples for the adhesion forces of T-Cells.

I tried different techniques to increase adhesiveness of the glass coverslip, such as different concentration of poly-l-lysine coating [136] and plasma activation of the surface. With these approaches, the cells became more adherent on visual inspection but only few mW of laser power were sufficient to detach them from the substrate, making the experiments impossible to perform.

4.2.3 CONCLUSIONS AND PERSPECTIVES

Atomic force microscopy has been used to characterise and quantify ICAM-1 - integrins interaction [137, 138]. This interaction becomes particularly interesting in a shear flow environment, because the induction of stable integrin-dependent adhesiveness in T-Cells seems to require the application of shear forces [138].

The preliminary results by McGloin et al. where they have investigated the interaction in static conditions with the cells attached to the substrate represented a first attempt to measure single molecule interaction between ICAM-1 and LFA-1. However, they were limited by the amount of applicable forces available with standard commercial probes, making impossible to extend their study in shear flow. The high strength tweezers could be used for such purpose, but they would first require further characterisation.

In fact, the functionalisation would need to be confirmed, for example by immunofluorescence study of ICAM-1. In addition to checking the functionalisation, it would be required to find a working procedure to bind the T-Cells not-specifically to the glass surface, in order to perform a force measurement. Only after having completed these steps, it would be possible to proceed and design a study performed in flow environment. Because neither myself or collaborators had expertise in improving not-specific

adhesion of T-Cells, I abandoned this study in favour of the research presented in the following sections of the thesis.

However, it is worth to highlight the major result obatined from this preliminary study on the functionalisation of custom made probes for high strength trapping: the custom probes performed similarly to commercial silica beads, when they were treated with a similar protocol, suggesting a successful functionalisation. Would the functionalisation be confirmed by further studies, the custom probes could be used in a biology lab without disruption of workflow, by applying the same protocols already available for commercial trappable beads.

However, it still remained to be proved that the photonically structured custom probes could be used for force studies in cell biology and that they were more beneficial than commercial beads.

4.3 CUSTOM PROBES FOR CELL BIOLOGY: THE MOTILITY OF DICTYOSTELIUM

With the aim to measure forces with the custom probes, I designed an experiment to study the motility of *Dictyostelium discoideum*, a soil amoeba often taken as model for cell crawling dynamics.

Dictyostelium discoideum is a social amoeba that has fascinated many researchers from biology to physics and mathematics [139]. These amoeba have an interesting life cycle, partly spent as single organisms and partly as a multicellular one. In fact, they live as single cells in the soil and feed on bacteria, but under starvation they organise and aggregate in a multicellular structure. This structure, called *slug*, migrates to the soil surface where forms a fruity body intended to release spores. The spores that land in regions with favourable conditions germinate to release new single cells amoebas. Dictyostelium in their single cell phase is often used as reference for the study of cell motility.

During starvation, the cells acquire a key ability: they become able to produce, secrete and degrade 3'-5' cyclic adenosine monophosphate (cAMP) [140–142]. Thanks to this ability, the cells start responding chemotactically to cAMP gradients. In presence of a cAMP gradient, Dictyostelium cells move in the direction of increasing cAMP, extending

pseudopods predomintantly in the direction of the chemotacting signal and suppressing lateral pseudopods [142]. While this skill is fundamental during the aggregation process and their organisation in the slug [141–143], their chemotactic motion was also employed by scientist to study cell motility in a controlled way where the movement of the cells can be directed through external sources.

THE MOTILITY OF DICTYOSTELIUM DISCOIDEUM: BLEBBING The motility of Dictyostelium is characterised by at least another peculiarity other than the chemotactic motion: in specific conditions, the cell can move through *blebbing* in addition to actin polymerisation at the leading edge.

Blebbing is characterised by the detachment of a part of the cell membrane from the actin cortex, followed by its inflation to form a round protrution filled with cytosol; finally the cortex is reassembled at the site to retract the bleb. Blebbing, happening in every direction on the cell membrane, is often observed during apoptosis in other organisms, but in Dictyostelium the blebbing is directional and used for migration, a behaviour shared also by cancer and embryonic cells [144]. Directional blebbing happen when the contraction at the rear of a cell, polarised during chemotaxis, causes blebbing in the front; when the cortex is reassembled at the bleb it stabilises the new shape and attach it to the substrate, instead of retracting the bleb.

In Dictyostelium blebbing increases in presence of cAMP gradient [144]. Other conditions that favourite blebbing over pseudopods motility are low osmolarity [145], reduced substratum adhesion [146] and increased substratum stiffness [147], suggesting that blebbing might provide an advantage in the motility of cells during the formation of the slug, when those conditions are met.

The intracellular pressure generated by myosin II contraction seems to have a role in the manifestation of blebbing. When myosin II is inhibited, cells show less blebbing [144, 148]. Further evidence on the role of hydrostatic pressure for blebbing is that when motility is dominated by pseudopods extension there is a delay between the protrusion of the leading edge and the contraction of the rear of the cell ($\sim 10 - 20$ seconds), while in conditions when blebbing is favoured there are occurrences where the formation of blebs and the retraction of the cell happen simultaneously [145].

4.3.1 METHODS

EXPERIMENT DESIGN My initial objective when designing this experiment was to investigate the forces that arise at the leading edge of migrating Dictyostelium cells. Attempts to achieve a similar result were pursued by using acoustic forces [149], but the forces generated by the acoustic devices did not exceed few pN and were not sufficient to affect the cells.

To test if the custom probes I produced could provide forces sufficient to stop or delay the cells, I designed an experiment similar to the one reported by Yang *et al.* for leukemia cells [56]. Yang and collaborators opposed an optically trapped bead to a migrating cell moving toward a chemo-attractant source. Similarly, I wanted to use the custom probes as a force load for Dictyostelium cells moving in a chemotactic environment. I confined the cells' movement in polydimethylsiloxane (PDMS) microfluidic channels filled with a linear gradient of cAMP, instead of using a local chemo-attractant source. To provide the load for the Dictyostelium cells, I introduced trapped beads in the channel opposing the direction of migration of the cells (see Figure 4.3) and video-recorded the cells response. I used both χTiO_2-αTiO_2-SiO_2 beads and commercial SiO_2 bead. To measure forces, the cells need to be fully stopped by the load: the cell would stop moving when the optical tweezers force to maintain the load in place balance the force of the leading edge of the cell; if the maximum force achievable by the tweezers is not sufficient to stop a moving cell, then the experiment would only provide a lower boundary for the forces exerted by the cells. The movement of the cells in empty channels (where no load nor trapping laser is present) is used as control.

Because the cell is confined in three dimensions, it needs less adhesion to the substrate as it can exert forces perpendicular to the channel and squeeze itself forward [150, 151]. This is a benefit, as adhesion forces can be neglected in first approximation.

SAMPLE PREPARATION For the experiment, I used an axenic strain (Ax2) of Dictyostelium. I cultured the cells in shaking flask with HL_5 medium at a density of 5×10^6 cells/mL. The cells were harvested and diluted to 1×10^6 cells/mL in a KK2 buffer solution. I starved them for 12h by depositing them on agar plates over night at $18^\circ C$.

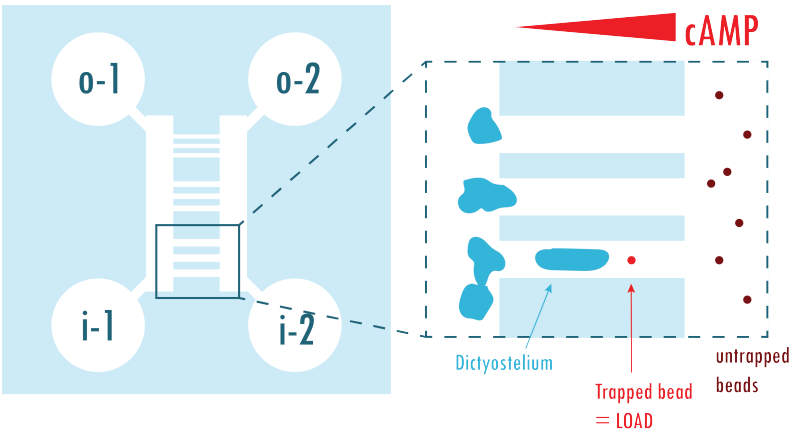

Figure 4.3: **Experiment design for Discyostelium discoideum studies** – Schematic of the PDMS chip. i-1 and o-1 are the cell inlet and outlet while i-2 and o-2 are the cAMP inlet and outlet. The chip has channels 3, 4 and 5 μm wide and $\sim$ 2.5μm high. I only used the 5μm wide channels. A trapped bead is moved into one of the channels where a crawling Dictyostelium is moving toward the cAMP gradient. The trap was kept on until the cell had successfully pushed the bead out of the trap.

Dr. Singer, from the *Cell and developmental biology* division at the University of Dundee, supervised me on the cultivation of Dictyostelium cells.

The PDMS chip containing the channels to confine the cells was made through a mold designed and produced with lithography by Dr. Yuri Belotti [152], from the *Physics* department at the University of Dundee. Prior to use, I cleaned the chip by removing dust with the aid of adhesive tape and then washed it with ethanol. Then the chip is laid on a round glass coverslip thickness no. 1, where it adheres not specifically. To open the channels, I flushed them with ethanol, while observing under the microscope that all the surfaces were being wetted. Finally, I washed the channels, the inlets and the outlets with KK2 for 3 times.

I injected the solution with the cells in the chip inlet i-1, balancing the inlet and the outlet so that there was no visible flow. I washed the beads in KK2 buffer and finally suspended them in a solution of 1μM cAMP in KK2 that I injected in the chemotaxis chip inlet i-2, balancing the inlet and the outlet so that there was no visible flow. I performed the experiment on the TIR-Ph set-up (described in chapter 6).

4.3.2 RESULTS

I trapped the beads at several powers, and observed the behaviour of Dictyostelium cells by collecting images at 250ms intervals. A first observation was that the trapped beads represented a load even a low power: Figure 4.4 shows that a cell that avoids a commercial bead trapped at 15mW instead of pushing it.

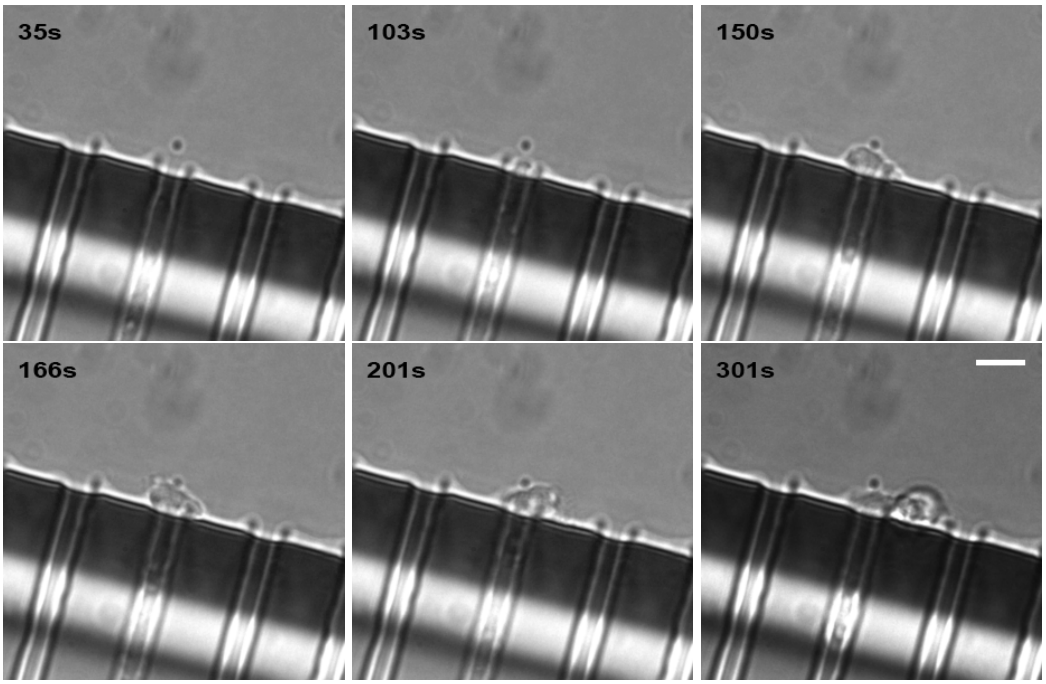

Figure 4.4: **Dictyostelium avoids loads in free space** – Dictyostelium cell exiting one of the channels with a load on its path. The load was a commercial silica bead trapped at 15mW. At t=150s and t=166s, the cell reached the load and stopped. Finally it moved to the right of the bead (at t=201s), instead of pushing the load from the centre and move forward. The video suggests that the cell is capable of perceiving even small load, and that it chose the path of minimum resistance. The scale bar is $10\mu m$.

When the cells are constrained in the channels, instead, they were forced against the load and they had to push it to move forward. Figure 4.5 show an example of a cell response against a load inside the channel.

The cells moving in the channels without traps (control cells), moved both through pseudopods and bleb-like steps. Bleb-like steps were characterised by a "jump" of the cell in 1 or 2 frames, instead of the smooth motion most common to pseudopods. Blebbing of Dictyostelium under chemotaxis was reported in literature, therefore it was unremarkable to observe bleb-like steps for the control cells. The average speeds of

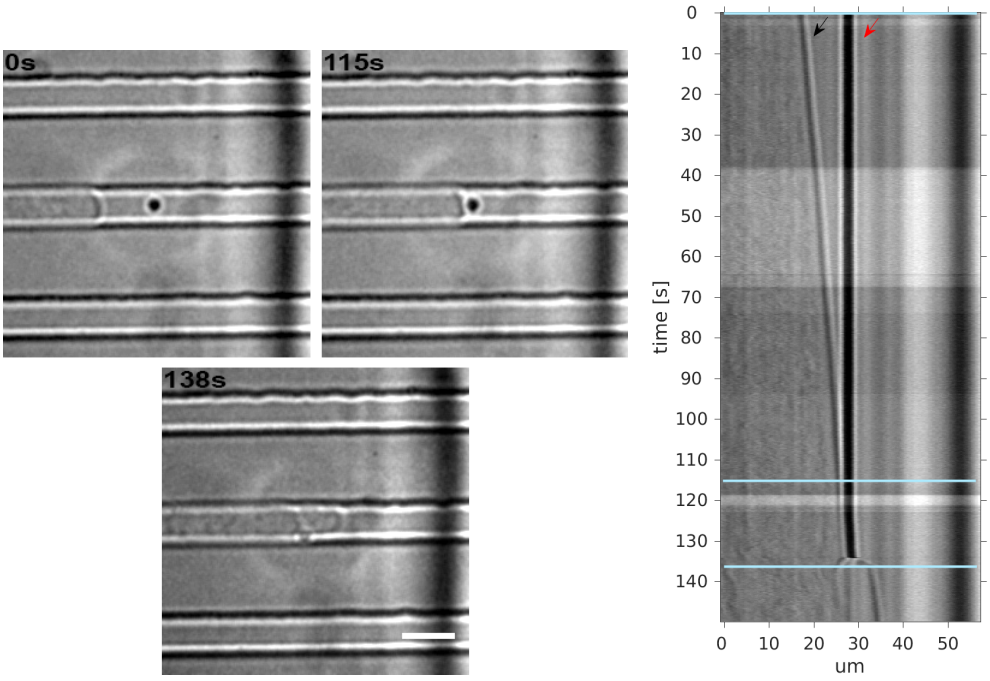

(a) (b)

Figure 4.5: **Dictyostelium against a custom bead** – Dictyostelium cell approaching a custom bead trapped at 800mW (a), and kymograph of the video from which the frames are extracted (b); The light blue lines in (b) represent the selected frames in (a); the red arrow indicates the trapped load and the black arrow indicates the leading edge of the cell. The cells did not move by bleb-like motion until it was subjected to the load. When the cell touched the load, first it started pushing it but then it was not able to overcome the force opposed by the optical tweezers through the load. The cell started moving with blebbing-like motion (t=138s) to overcome such force. The scale bar is $10\mu m$.

control cells was 0.3 $\mu m/s$, with bleb-like steps of less than 2μ and a speed of 3.4 $\mu m/s$ (Figure 4.6).

When I opposed the motion of the cells with custom and commercial beads trapped at 150mW and 800mW, the overall speed of the cells decreased. This could be due to the optical forces opposing the cells. Looking at the bleb-like steps, it was interesting to observe that the cells moved smoothly until reaching the load (instead of showing spontaneous bleb-like motion as for the case of the controls), then they slowed down and started to push the load. Finally they stopped for a few frames and they pushed the load out from the trap, i.e. they overcame the optical forces, with a large bleb-like step of more than >2 μm (see fig:dictyframes2 and Figure 4.6). This phenomenon was

particularly evident for higher trapping power and when the load was represented by custom beads.

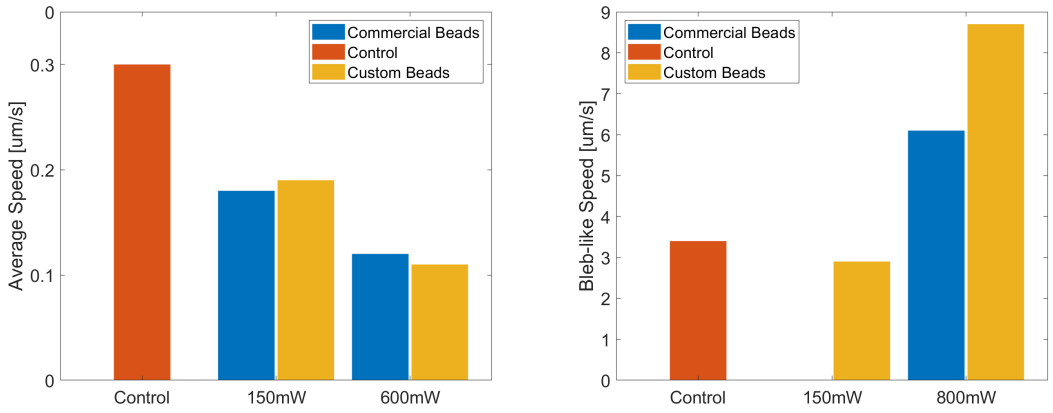

(a) (b)

Figure 4.6: **Preliminary data on Dictyostelium motility** – Measured speeds for the overall (a) and for the bleb-like (b) motion of the cells, when commercial (blue) and custom (yellow) beads were used as load. Graph (a) shows that the cells speed decreases with higher power used in the tweezers. Graph (b) shows that the speed of the bleb-like steps increased with larger loads, i.e. custom beads at higher laser power. The control data were averaged over 6 different cells, while the load data from 3 repeats on 2 different cells for both cases.

FORCE MEASUREMENTS In addition to qualitative observations, it would have been interesting to measure the force applied on the load by Dictyostelium. Unfortunately, it was impossible to use the self-calibrating method required for the force measurement for this experiments: in fact, the laser light would scatter throughout the whole PDMS chip before reaching a QPD, preventing to perform forward-scattering interferometry. To overcome this issue, I could have used backward-scattering interferometry. However, when I attempted to perform backward-scattering interferometry, I realised that the characterisation of this technique for the TIR-Ph set-up would require more time and effort than what was available to me at the time of the experiments. Preliminary efforts to set up a backward-scattering interferometry technique are reported in Appendix C. Moreover, I was never able to completely stop the cells. To increase the load and stop the cells, I gradually increased the trapping laser power in order to obtain higher forces.

I observed that the presence of the trapping laser for power >800mW caused the cells to slow down, to stop or even to revert their motion even before getting in contact with the load (Figure 4.7). The origin of this behaviour would need further investigation.

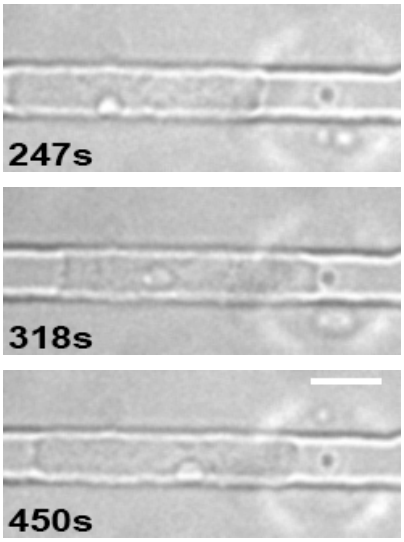

Figure 4.7: **Dictyostelium moving backwards respect to chemoattractant gradient** – Example of cell moving backwards despite the chemotaxis gradient. I observed this type of behavior only when I used trapping power >800mW. The scale bar is 10μm.

The low throughput of these experiments played a crucial role in the decision to stop the experiments. I was only able to collect a few data points over a three months experiment and the optimisation of the techniques (i.e. force measurements, investigation of effects from laser power >800mW, characterisation of the blebbing-like steps) would have required a much greater effort in term of time and resources that was available to me at the time.

4.3.3 CONCLUSION AND PERSPECTIVES

The results in Figure 4.6 are fascinating, and worth pursuing further studies. The data suggests that:

- An external load was capable of slowing down Dyctiostelium cells
- Bleb-like steps increased when Dictyostelium faced a large load
- Bleb-like steps were larger for custom beads.

These results are only suggestive and far from being definitive. However, I wanted to advance an hypothesis that could explain them. My working hypothesis is that the cells started to push the trapped bead but eventually the force opposed by the load was too high. To overcome such force, the cell used blebbling, pushing the beads away from the trap in an abrupt manner; the direction of blebbing was set by the chemotactic gradient, the occurence and magnitude of blebbing by the load. In fact, blebbing would be a consequence of the increased hydrostatic pressure inside the cell when its motion was opposed by the load.

To verify this hypothesis, future studies should aim at:

- repeating the experiments and obtain significant statistics on the observed behaviours of Dictyostelium against different loads.
- measure the forces exerted by the cells in different experimental conditions, for example through a self-calibrating interferometry technique backward-scattering configuration.
- characterisation of the bleb-like steps of the cells. Confirming that the observed motion of Dictyostelium is indeed blebbing would require further analysis. For example, this could be achieved by imaging in fluorescence microscopy the actin network: blebbing is recognizable by the rupture of the actin network at the site where the bleb occurs, and its subsequent recruitment of actin to reassemble the network at the bleb.
- verify the working hypothesis through observation of other cytoskeleton components. For example, hydrostatic pressure would be generated by an accumulation of myosin in the rear of the cell while the leading edge of the cell does not advance. By using the 488nm laser available in the set-up, it would be possible to perform fluorescence imaging of GFP-transgenic Dictyostelium.
- investigate the effects of high power lasers in the PDMS channels. It would be interesting to understand why the cells were stopping or reversing their motion when high power laser was lighted in the channel. Possible explanations include heating of the medium or degradation of the cAMP gradient in proximity fo the laser focus.

Despite the experiments were unsuccessful, I believe that these preliminary data justify further investment in this project. I observed a behaviour that has never been reported in literature – the step response when the cells push against an external load– and I argue that the use of custom probes might be beneficial in this circumstances, as they represent a larger load for the cell, enabling to access this observation at lower laser powers.

4.4 DISCUSSION

Summarising the results presented in the part I of this thesis, regarding high strength photonic tweezers, it can be highlighted that χTiO_2-αTiO_2-SiO_2 probes for optical trapping are a more robust solution to χTiO_2-αTiO_2 probes. Specifically, I showed that silica coated custom probes:

- **outperformed commercial beads** in term of trap stiffness. I measured a trap stiffness 2.5 times higher than for commercial beads of comparable size. Furthermore, they are trappable for every bead size and they can be trapped and used in different set-ups, whereas titania core-shell particles were only trappable in a small range of sizes and only in set-ups that were optimised for use of titania beads of a specific size.
- **easily integrated in bio-lab workflow**. In many biology labs, researchers employ and have optimised protocols for silica beads. I showed that the same protocols are effective for the custom beads. For example, the ICAM-1 functionalisation protocol for commercial silica beads was viable for the photonically stuctured probes with limited modification.
- **could be used to access new biological phenomena**. This preliminary study on the Dictyostelium is the first report on the response of the leading edge of Dictyostelium discoideum to an external load, and it suggests a different behaviour whether the cells were exposed to stronger or weaker traps.

While the custom probes can be improved in many ways, from the reproducibility of the chemical reactions to the monodispersity of the samples, the experiments I hereby reported are a stepping stone for future experiments aimed at measuring forces with

photonically structured probes. They have the potential to compete with other techniques operating at nN forces, such as AFM, but without their disadvantages.

Furthermore, failing to stop highly motile cells, like Dictyostelium, with custom probes trapped at 800mW is an important result: it provide evidence that further efforts should be made to increase the capability of optical tweezers even beyond few nN. A whole new set of biological phenomena would become accessible if we will be able to further advance the limits of optical tweezers.

Part II

OPTICAL MANIPULATION OF CELL JUNCTIONS IN CHICK EMBRYOS

5

CHICKEN EMBRYO DEVELOPMENT

Science fascination on the development of life is deeply rooted in our culture: the greek philosopher Aristotele first described the chick embryo development in the *Historia Animalium*[1] already in 350 b.C. [153] In fact, the chick embryo is a very convenient organism for experimental studies: scientists literally only need to "crack an egg open" to have a sample ready to study!

However, studying embryo development is far from being an easy task: thousand of cells coordinate their movement during the transformation of the tissues in the embryos, and many questions still remain unanswered. An key moment of the amniotes development is *gastrulation* – the moment at which the main three germlayers, the ectoderm, the endoderm and the mesoderm, are formed. During this phase, the tissue undergo a large amount of stress. Optical tweezers can be used to study the forces that drive this process.

5.1 GASTRULATION IN CHICK EMBRYOS

Chick embryos develop over a time of about 20-21 days after the egg is laid. During this time, the embryos undergo severe changes, that have been classified into different phases by Hamburger-Hamilton according to the embryo morphology [154]. It is interesting that, despite developing beaks and feathers, the early phases in the avian development are common with the majority of amniotes, including humans [155].

Specifically, a crucial moment of amniotes embryos is the phase of *gastrulation*. In the chicken, gastrulation happens between stages II and IV of the Hamburger-Hamilton timeline (HH2-HH4), in the first 19h since the egg was laid [154]. At the time the egg is laid, the embryo already contains more than 50000 cells, organised in two concentric

1 The most accurate translation of the Historia Animalium from greek to English was made by Prof. D'Arcy Thompson, one prominent figure at the University of Dundee. Interestingly, Prof. D'Arcy Thompson was a pioneer in the interdisciplinary sciences, often offering mathematical models for the description of zoology.

flat discs structures on the yolk and protected by the vitelline membrane [155, 156]. The inner disk takes the name of *area pellucida*; it is semi-transparent since it is formed only by two layers of cells. The two layers of cells of the area pellucida are different from each other: the upper layer, called *epiblast*, is an epithelial tissue formed by columnar cells closely packed together by adherens junctions and in contact with a complex basal lamina; the lower layer, called *hypoblast*, is formed by losely attached cells. The outer disk, instead, forms a ring called *area opaca*; it is formed by yolk-rich cells that will develop extra-embryonic structures. The cells at the interface between the area pellucida and the area opaca form the *marginal zone*. When gastrulation starts, the cells of the epiblast start ingressing the outer layer to form the hypoblast and, later, the *mesoderm* and *endoderm*. The superficial layer of cells will evolve in the *ectoderm*.

The strongest visual sign of gastrulation is the primitive streak: an elongated region of several layers of tissue formed by cells that migrate, ingress and eventually leave to reach their designated position in the body. Throughout this process, the initial isotropic symmetry of the embryo is broken, and the apical and dorsal polarities of the organisms are decided [155, 157]. The streak extends for about 12h, before regression starts [155, 158].

During the streak formation, the cells in the epiblast undergo large movements: at each side of the streak, they move in two counter-rotating flows [160]. Even before gastrulation starts and the primitive streak becomes visible, it is possible to identify the regions that would later become responsible for the elongation of the streak. In fact, two cells flows are visible a few hours before the streak itself: anterior-lateral cells replace the ones moving toward the streak from the *Koller's sickle* - a triangular shaped region located in front of the posterior marginal zone [160]. The cells occupying the Koller's sickle will become mesoderm cells.

It is still unclear what starts and drives the large scale movements of the cells during the streak formation. There are many literature studies attempting to provide an answer, suggesting explanations such as fibroblast growth factor (FGF) induced chemotaxis [161–163], increased cell division [160, 164] and cell intercalation [164, 165]. The latter is a fundamental mechanism for a tissue to change shape: two neighbouring cells shorten a common boundary creating a T junction where 4 cells share a common node; finally,

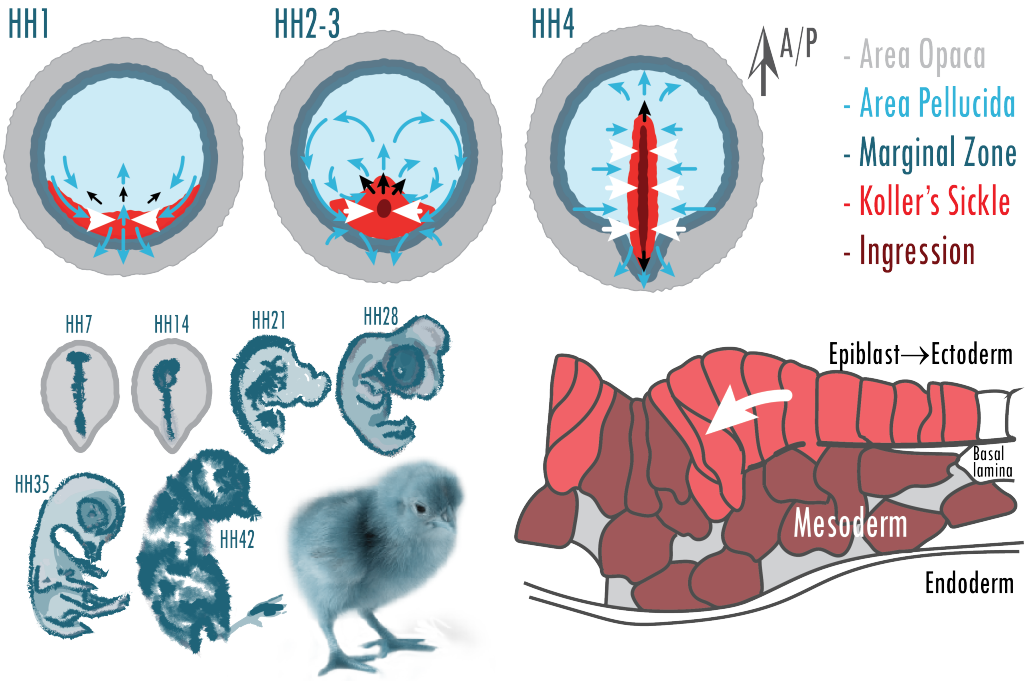

Figure 5.1: **Chick embryos gastrulation** – During stage I to IV of the Hamburger-Hamilton timeline, gastrulation takes place. HH1 – Even before visible signs of gastrulation, cells in the Koller Sickle start to move (blue arrows) thanks to active pulling forces (white arrows). The movements generate passive pushing forces (black arrows). HH2-3 – After about 5h, the Koller sickle elongates in a triangular shape. The cells move in vortex-like pattern, they start to ingress and they relocate to form the mesoderm. HH4 – The tip of the triangular region extend into the primitive streak, which elongates until it reaches about 80% of the length of the area pellucida. The cells continue to ingress through the streak. In red, a cross section of the streak area is shown. HH5-7 – The streak starts a regression movement and the first somites are formed. HH8-H45 – The embryo development is completed until the embryo hatches - A quick overview is reported in the graph. HH1-HH4 are adapted from [159] – HH7-HH42 are sketches of the Hamburger-Hamilton photos of the development stages [154] – The streak section is adapted from [155]

the two initial cells move apart while a new junction is formed perpendicularly to the direction of the initial contraction. With this process, cells that were previously distant become neighbours Figure 5.2 [165].

In Drosophila, it was reported that cell intercalation plays a fundamental role in the flows observed during development, especially during *germband* extension (germband

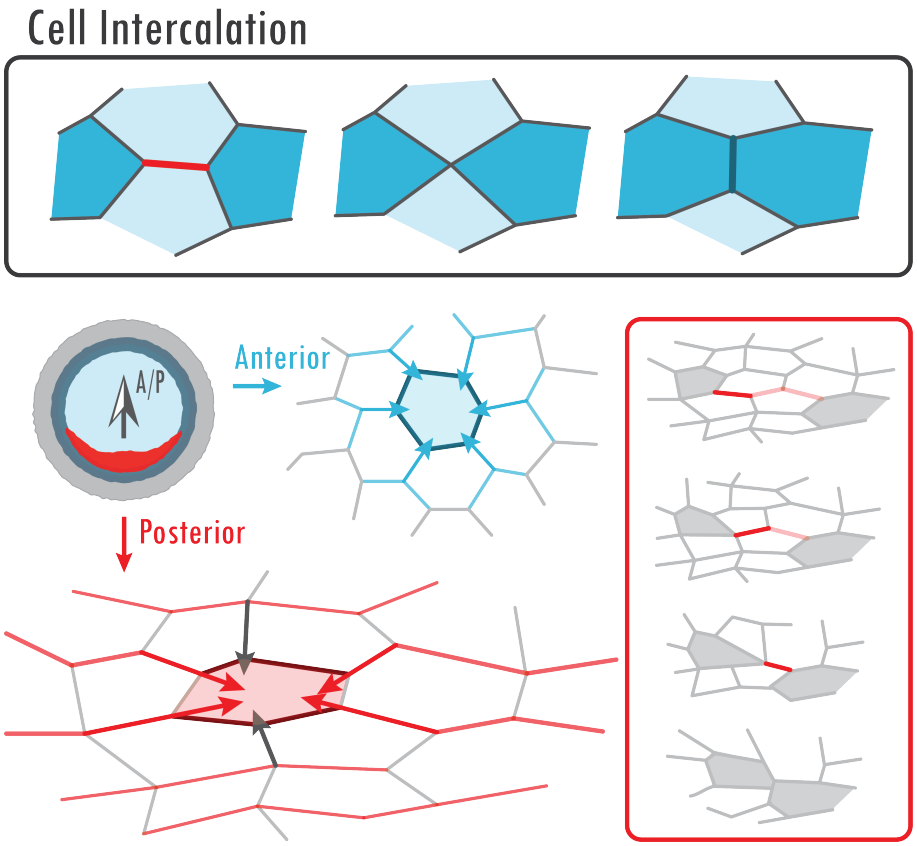

Figure 5.2: **Cell intercalation in developing embryos** – Top insert: A junctions (red) between two neighbouring cells (pale blue) is contracted into a T-Junction. A new junction is extended (dark green): the cells that were farther apart (dark blue) become neighbours. Bottom: In the anterior part of the chick embryo, the cells have an honey-comb like shape and the tension is distributed simmetrically. In the posterior area, in the Koller's Sickle, the cells are elongated, with the junctions aligned in a preferential direction, where myosin II cables have been observed [159]. The tensions are distributed anisotropically along the cables. A contracting junction increases the tension in neighbouring junctions; in turn, they recruit myosin and start contracting. This feedback mechanism contributes to the intercalations in the Koller sickle area, that results in the contraction of the posterior tissues prior the streak (red insert on the right). – Top insert is adapted from [165]; bottom and right inserts are adapted from [159]

extension in Drosophila is equivalent to streak extension in chicken). Bertet and coworkers found a preferential intercalation along the anterior/posterior (A/P) axis and suggested that myosin II was responsible for the polarized contractile forces [165].

Similarly to Drosophila, directional intercalation was observed in chick embryos [166]. For example, in the sickle region, mesendoderm cells rearrange by directional contrac-

tion of aligned junctions [159]. The junctions in the posterior area align over several cells; myosin II co-localises with these aligned junctions and organises in patterns of myosin light chain cables in the same direction in which the mesendoderm contracts [159] (see Figure 4.2). Pentabromopseudilin (PBP), an inhibitor for myosin V and myosin II, prevents the formation of these cables and the elongation of the streak [159]. Similarly, pentachloropseudilin (PCP), an inhibitor for myosin I, strongly inhibits the tissue motion, completely blocking contraction in the mesendoderm, cell intercalation and streak formation [159]. While only myosin II seems to be responsible for the supercellular aligned cables, it is not surprising that the inhibition of myosin I can produce similar results to the inhibition of myosin II. In fact, myosin I might be responsible to sense tension at the membrane-cytoskeleton interface [167].

Rozbicki *et al.* proposed a hypothesis based on these observations. Supercellular alignment of the junctions could explain long range contraction in the posterior area. When a junction contracts, the neighbour junctions experience an increase in tension and recruit myosin to counteract it. The newly recruited myosin makes the neighbour junction contract, that in turn would cause other neighbours to experience increased tension. This process is propagated sequentially through the myosin supercellular cable. Whereas these observations are being intensively studied by statistical analysis on a large scale, for example using light-sheet microscopy [168–170], a model to explain the local forces driving these coordinated movements is still lacking. A more physical approach could provide measurement and analysis of tension in cell junctions and help to develop such a model [171].

5.2 MEASURING FORCES IN TISSUES

There are several techniques that can be used to measure forces in tissues. For example, compressibility of a tissue can be measured by squeezing a piece of tissue between two parallel plates and measuring the deformation of the tissue [17, 172]. Alternatively, atomic force microscopy can provide a value for surface tension and can act as a force transducer [17, 172, 173]. However, both techniques are not ideal: they require direct contact with the tissue, which can disrupt normal development; the values are measured either on a large area (although the tip of the indenter of the cantilever is small, it usually

has effects on large range distances) or on long time-scales [172]; most importantly, these techniques rely on applying forces perpendicular to the tissues, providing less insight on the tension in-between cells.

An interesting alternative is represented by techniques that can act from "within" the system. For example, liquid droplets inserted in-between cells can be used to infer tension forces by studying the deformations on the droplets caused by the neighbours cells [17, 174]. Unfortunately, this ingenious approach is complicated and it is not ideal for monolayered epithelial tissues [172].

Another way to study the system from "within" are Förster resonance energy transfer (FRET) tension sensors. The donor and acceptor fluorophores of FRET are connected by a spring of known stiffness, so that the fluorescence intensity reveals the relative distance of the molecules and therefore how much the spring was under tension [17, 172]. But FRET signal-to-noise ratio is small, especially in living samples; also, the technique provides only an average molecular tension rather than a direct measurement of tension in the cell junctions [17, 172].

Mathematical interpretation and viscoelastic models can also be used to interpret shapes variations in tissue. For example, the fact that tissues do not tear themselves apart means that forces must be balanced: graph theory and force distribution can be used to estimate the relative ratios of forces when the tissue or the cell shape changes from a purely isotropic configuration [17, 172]. This approach was used to estimate forces in Drosophila during gastrulation [175].

Finally, optical techniques, such laser cutting and optical tweezers, can also be used to measure forces in tissue. When a high power focused laser "cut" one or more cell junctions, the velocity at which the junction retracts after the cut correlates with how much under tension the junction originally was. Similarly, we could look for anisotropic force distribution by cutting junction in different directions and observe how the tissue responds [17, 172].

Optical tweezers can also directly manipulate tissues, although it is not a trivial task. Despite optical tweezers applications in cellular biology are well established (see Chapter 4), they were seldom used at tissue level. This is partly due to the magnitude of forces than can typically be applied (up to 100s of pN for tweezers not using photoni-

cally structured beads), but also to the degradation of the tweezers stiffness inside highly scattering media. Nevertheless, the recent years have seen an increasing interest in these applications, and today's literature reports examples of optical tweezers applied inside living zebrafish [60, 176, 177] and in Drosophila embryos [61, 178, 179]. These experiments prove that using optical tweezers in vivo is feasible, but they also highlight that careful interpretation of the results is needed. For example, it might be necessary to study the scattering pattern to have a correct evaluation of the trap stiffness [60, 176].

5.2.1 OPTICAL MANIPULATION OF CELL-CELL JUNCTIONS

The applications of optical tweezers in Drosophila embryos [61, 178, 179] are particularly interesting for the investigation of forces generated during the chick embryo development. In fact, the authors of those studies used optical tweezers to trap cell-cell junctions: they estimated tension by moving the junctions with the tweezers and measuring how much they deflected from their rest position. Specifically, they observed that

- Optical tweezers can trap and manipulate cell-cell junctions directly, without the need to introduce external probes (like silica beads) in the tissue[61, 179]. However, the authors fail to ask what geometry should be considered for the evaluation of the trap stiffness? In fact, it is difficult to quantify optical forces for objects that are not spheres [2].
- The junctions showed a visco-elastic response [61, 179].
- The trap was calibrated *in vivo* [61, 179] by measuring the trap stiffness on a known probe (i.e. polystyrene beads) inserted in the tissue. This information was used to estimate the stiffness of the junction: the trapped bead was pushed against the junction; the deformation of the junction obtained when using the bead and the one obtained when trapping the junction directly were compared. The proportion found between these two deformation was used to scale the scale the trap stiffness measured on the known probe.
- Finally, they provided further evidence on the role of myosin II: they showed that the tension of Drosophila cell-cell junctions was larger for older embryos and for

2 Optical forces can be simulated also for other simple shapes, e.g. rods and ellipsoids, as well as for non perfect spheres, i.e. a sphere with a rough surface [64]

junctions aligned perpendicularly to the A/P direction; most importantly, they observed that the tension was reduced when the embryos were treated with an inhibitor for myosin II [61].

I found, however, that the technique presented a few drawbacks: for example, the calibration of the trap was not reliable, as it is unclear how the forces act on the object being trapped when cell-cell junctions are manipulated. Also, not all the results reported were statistically significant, due to the intrinsic variance in the sample.

5.2.1.1 *Optical manipulation of cell-cell junctions in chick embryo*

A similar approach to the optical manipulation used for these Drosophila studies could be employed to measure locally the forces in the posterior area of the embryo prior to the streak formation, and to help generate a model to describe the system. In the following chapters, I will show how I extended the optical manipulation of cell-cell junction to the case of chick embryos.

6

TENSION IN CHICK EMBRYOS JUNCTIONS: MATERIALS AND METHODS

A working hypothesis to explain what drives the streak formation in chick embryos was advanced by Rozbicki and Weijer. They hypothesized that myosin II induces changes in the tissue: it causes directional tension in the posterior area of the embryo that induces cell intercalation [168].

Reproducing the approach used for Drosophila [61, 179], I aimed at using optical manipulation to estract information on the chick embryo junctions along the myosin II cables. This could be achieved by observing the dynamics of a junction after it was moved a given distance from its equilibrium position with optical tweezers. Moving a trapping laser across the junction perpendicularly to the imaging plane and to the direction of the junction caused the junction to deform following the movement of the laser. The optical forces overcame the other forces acting on the junctions (i.e. the tension and the drag from the cytosol) and as a consequence the junctions deformed; the deformation, in turn, resulted in increased tension in the junction and generated a restoring force. When the junction was released from the trap, i.e. the trapping laser was turned off or the increased tension overcame the optical forces, it contracted back to its rest position. I used transgenic embryos expressing a membrane-localized GFP and fluorescence microscopy to image the deformation of the junction. For this purpose, I designed, built and optimized an optical set-up with optical tweezers integrated on an inverted microscope (Figure 6.2). The experiments were conducted together with Dr. Chuai from the *Cell and Developmental Biology* division at the University of Dundee, and specific contributions are highlighted throughout the text.

For all the measurements, the following steps were performed:

1. the region of interest in the embryo was located thanks to a low magnification branch of the optical set-up;

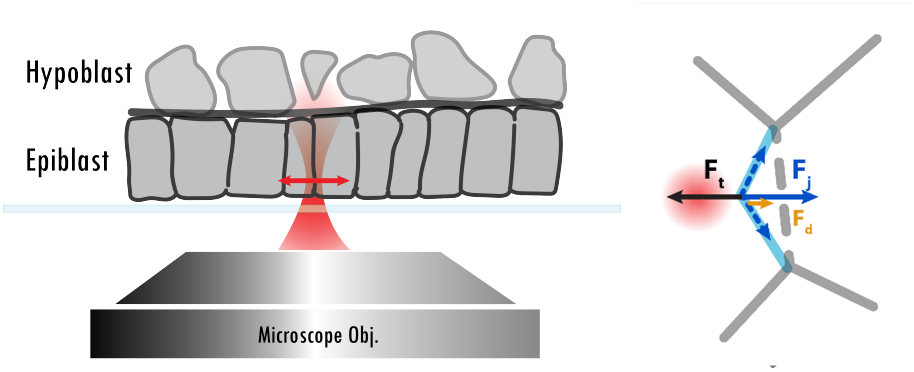

Figure 6.1: **Experiment design for the optical manipulation of cell-cell junctions in chick embryos** – Left: side view of the sample mounted with the epiblast facing the glass coverslip. The trap is moved perpendicular to the junction (red double arrow). The movement of the trap depends on the type of experiment. Right: bottom view of the sample. The trap exerts an optical force on the junction F_t (black arrow), while the tension in junctions generates an opposed force F_j (blue arrow) in the same direction of the drag in the cytosol (orange arrow, F_d). The junction is displaced (blue segment) from its rest position (dashed line). The deformation stops when the forces are balanced.

2. a suitable junction, i.e. a junction that would be perpendicular to the movement of the trap, was selected;

3. the measurements were performed while recording the video sequence with the imaging camera.

4. the video and the parameters used for the experiments, such as laser power, operational mode, travelled distance, frame rate, etc, are saved on disk by a Matlab script.

To study the deformation of the junction over time, I generated kymographs of the junctions from the recorded frames. I extracted the position of the junction from the kymograph by using a custom made algorithm based on a Seam Carving Algorithm (described in the following sections). Finally, the junctions deformations were analysed and relevant information was extracted, e.g. the maximum deformation.

6.1 THE TIR-PH SET-UP

An infrared laser (wavelength 1070nm, ytterbium doped fibre, IPG Photonics) was focused by a 100x microscope objective (Nikon CFI Apochromat TIRF, oil immersion, NA=1.49, W.D. = 0.12 mm) to generate the optical tweezers. The same microscope objective was used for imaging the embryo; a dichroic mirror (Thorlabs DMSP950) and a bandpass filter (Chroma ET750sp-2p8) were used to separate the infrared light and to eliminate the back-scatter reflections of the laser onto the camera. The trapping laser was moved by a piezo-actuated mirror (Thorlabs POLARIS-K1S2P) conjugated with the back focal plane of the objective. The set-up was set to be used both for reflective bright field imaging at low magnification and fluorescence microscopy at 100x magnification. For the low magnification imaging, a custom-made ring, composed by 8 white LEDs equidistantly mounted at a 45 degrees angle, illuminated the sample; the image was collected in reflected light by a 4x microscope objective mounted around the sample holder (Zeiss Achroplan, air immersion, NA=0.1, W.D.=11.1mm). The high magnification imaging was conducted in epifluorescence mode: the EGFP in the cell membrane of the chick embryos was excited with a 488 nm excitation laser (488 Sapphire SP, Coherent) through the 100x Nikon microscope objective; a scientific CCD camera (Hamamatsu Orca flash 4.0) imaged the sample, with the excitation and emitted fluorescence light being separated by a second dichroic mirror (Chroma ZT488rdc) and an edge filter (Semrock BLP01-488R-23.3-D) placed before the camera.

I wrote a Matlab script to hardware-trigger the piezo-actuated mirror and the camera via a data acquisition card (National Instruments data acquisition card NI PCI-6251 with connector box SCB-68A); this ensured that for every frame saved, the trap was in a known position in the sample. I performed the experiments using the laser at 750mW, measured in the image plane; the laser power was chosen by observing the embryo at different laser power and employing the highest laser power that was not visibly damaging the sample (this choice is further discussed in the following sections). Finally, the set-up was equipped with a custom-built incubator chamber to keep the embryos at 37 degrees Celsius during the experiments. In Figure 6.2, a schematic of the set-up is presented.

The set-up used for the optical manipulation of chick embryos tissues was named TIR-Ph and further details about it are reported in Appendix A. The appendix also includes the techniques used for the characterisation of the lasers and of the pixel size on the camera.

6.1.1 OPERATIONAL MODES

I programmed the set-up though Matlab so that it could to operate in two different modes: 1) the trap moves of sinusoidal motion; 2) the trap moves a fixed distance and then it is turned off. In the first case, referred to as "Sine wave" operational mode, I observed the junction following the trap with a sine wave motion with the same frequency as the applied movement of the trap but with a small phase delay. In the second case, referred to as "Pull&Release" operational mode, I observed the junctions reaching their maximum deformation and then moving back towards their original rest position after the trap was turned off, following an exponential decay that can be described with a visco-elastic model.

Through a Matlab GUI (described in Appendix B), the experimenter can decide whether to move the trap via the piezo-actuated mirror or to move the sample stage; in both cases, the relative motion is the same. Moving the mirror provides data with higher signal-to-noise and requires less processing before the analysis, but it's limited in travel distance (maximum travel distance = 2.6 μm). The stage can be moved of larger distances, but it requires more processing before the analysis, i.e. the frames need to be realigned and this can cause artifacts.

Figure 6.3 shows example of junctions being deformed by the tweezers, cartoons of the operational modes, kymographs of the junctions and tracking and analysis of their position.

Sine wave mode

With the sine wave mode, the trap moved with a sinusoidal motion across the junction for a given period of time (Figure 6.3 - green insert). I used the sine wave operational mode only at the beginning of the investigation on chick embryos junctional tension. For

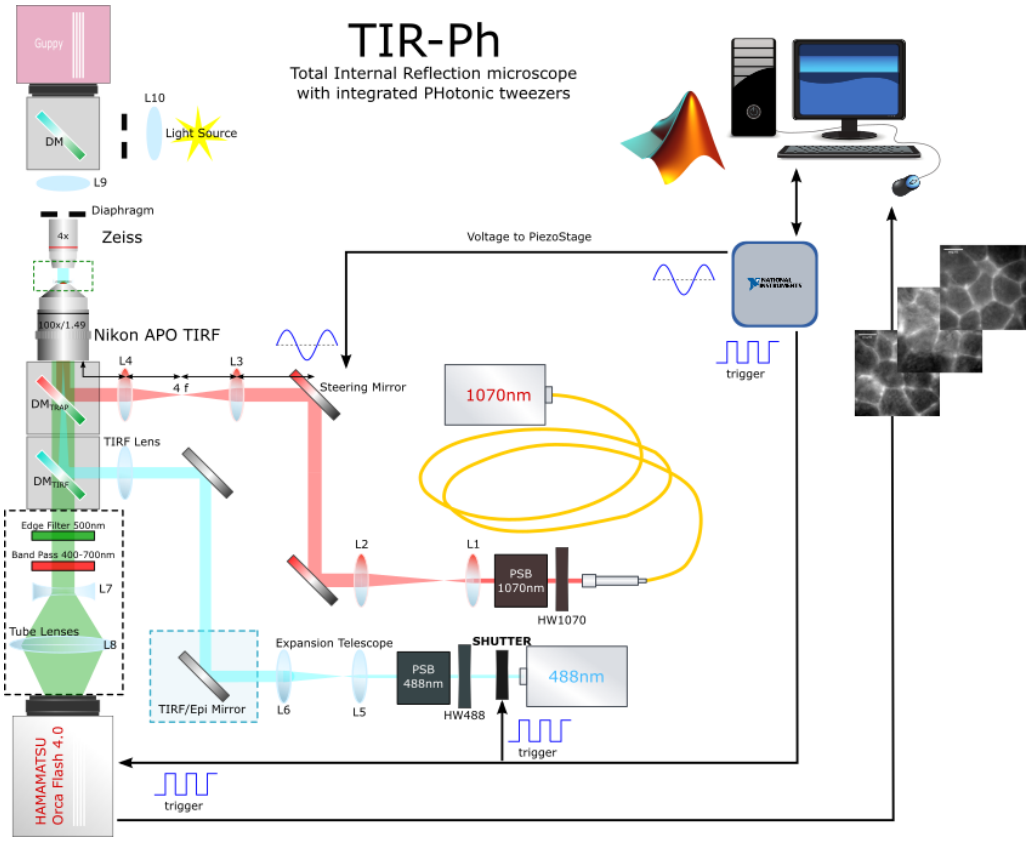

Figure 6.2: **Description of TIR-Ph set-up used for chick embryos studies** – The set-up consisted of: an optical tweezers path (red), a fluorescence laser path (blue and green) and an illumination/imaging arm. The laser was moved through a piezo-actuated steering mirror. The 100x Nikon TIRF microscope objective (N.A. 1.49) collected the laser light into the image plane. The sample was mounted on a piezo stage. A 488-nm laser (blue) was used as an exciting source for fluorescence imaging. A dichroic mirror reflected light below 500nm, while a lens focused the beam at the back focal plane of the TIRF objective. The fluorescence image (green) was collected by the objective and redirected onto the scientific camera. An edge filter at 500 nm cut the back-scattering from the exciting light and a band pass filter at 400-700nm cut the IR back-scattering from the trapping laser. An illumination arm (white) was integrated with a low magnification imaging. A custom-made circle of 8 LEDs mounted at 45-degree angle around the embryo (not in picture) illuminated the sample; this light was collected by the 4x Zeiss objective and imaged on a Guppy Camera (Allied Vision). Finally, a custom-made incubator kept the set-up at 37 degrees. Both laser shutters, the camera trigger, the piezo-controller and the LEDs lights were controlled through a National Instrument data acquisition card via Matlab GUI described in Appendix B. All the optical elements of the set-up are listed in Appendix A.

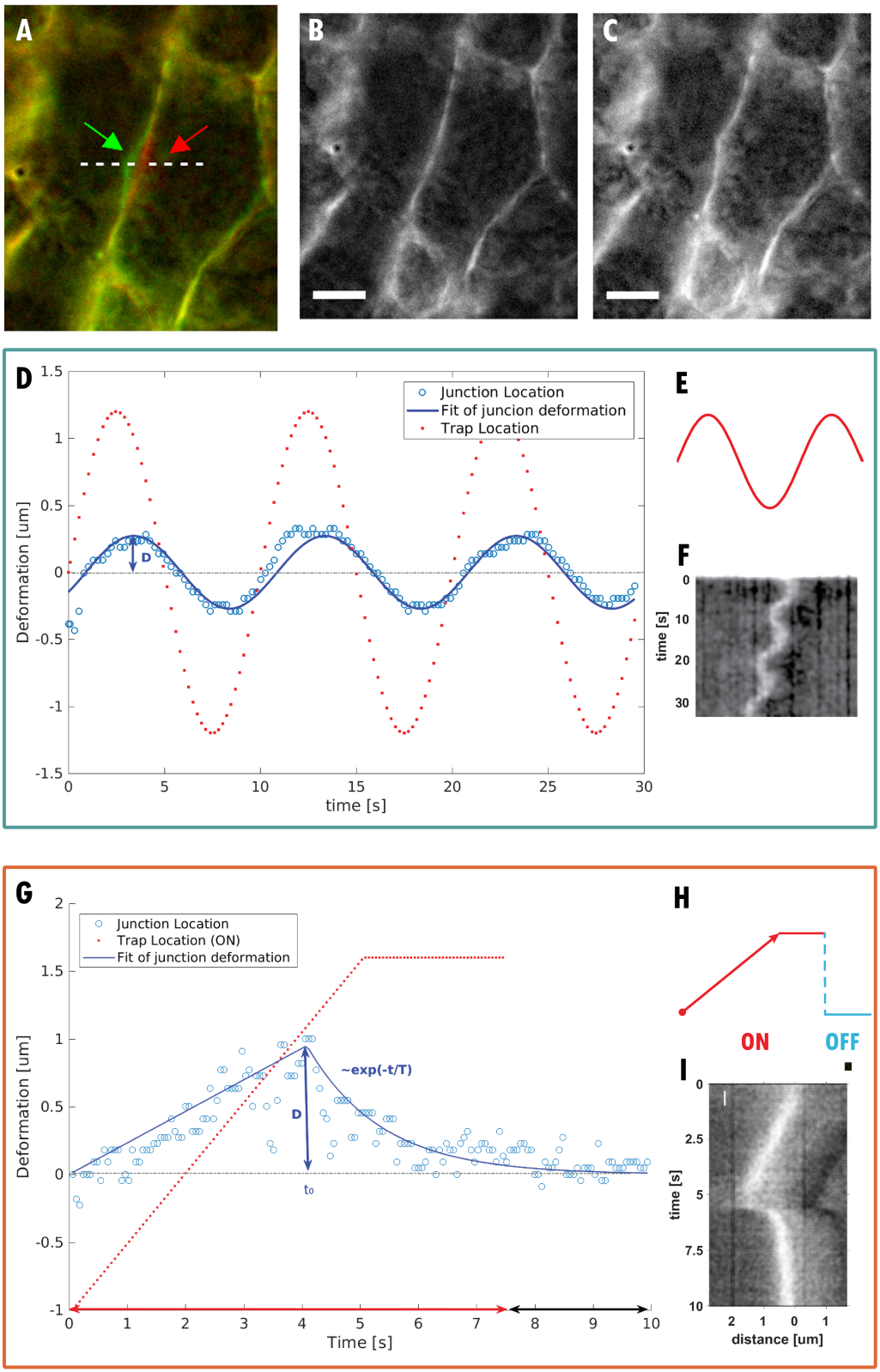

Figure 6.3: **Operational modes** –

Figure 6.3: **Operational modes**, continued – (A-C) show an example of a junction being deformed by the optical tweezers. (A) is a false color showing the superposition of (B), the first frame with the junction at rest position (red channel), and of (C), frame showing the maximum deformation achieved by this junction (green channel).
The green insert contains details about the "Sine wave" operational mode. A sinusoidal signal (E) is applied to the piezo-actuated steering mirror (or to the sample stage), moving the trap across a selected junction. The deformation of the junction follow a sinusoidal motion, as can be observed in the kymograph (F). The position of the junction over time at the location of maximum deformation is extracted and fitted with a sine wave to extract the maximum deformation (D)
The orange insert contains details about the "Pull & Release" operational mode. The trap is moved across the junction at constant speed with piezo-actuated steering mirror and then turned off (H). The junction reaches a maximum deformation and then contracts back to its rest position, as can be observed in the kymograph (I). The position of the junction over time at the location of maximum deformation is extracted and fitted with a visco-elastic model.

the early experiments, this mode was particularly convenient: in fact, over the course of a measurement the trap crosses the selected junction multiple times, allowing to collect more data. However, the analysis is more complex compared to the Pull & Release mode: longer period of acquisition made the junctions vulnerable to bleaching, reducing the signal-to-noise ratio.

For data collected through this mode, I fitted a kymograph of the deformed junction location with a sine function with the same frequency of the trap movement and obtained values for the amplitude and phase. The frame rate of the video was varied between 12 and 15 frames per second accordingly to the quality of the fluorescence signal.

Pull & Release mode

With the the Pull & Release operational mode, the trap moved 2.6μm across a selected junction. The trap moved this distance in 5 seconds, after which was left in position for 2.5 seconds and then turned off (Figure 6.3 - orange insert). During the measurement a

video of the junction was recorded and saved through Matlab at a rate of 15 frames per second.

With this type of experiment, I measured the maximum deflection D and used a viscoelastic model to determine how quickly a junction returned to its rest position.

6.2 SAMPLE PREPARATION

For the experiment, a membrane-localized GFP transgenic chicken line was used [168]. The national Avian Research Facility at the Roslin institute in Edinburgh provided the fertilised eggs. Dr. Manli prepared the embryos and grew them in early chick (EC) culture [180] and incubated them at $37^{\circ}\,\mathrm{C}$. They were used at about 3h for early experiments and at about 5 hours (or until a well-defined Koller's Sickle was visible) for experiments to verify the working hypothesis presented.

Dr. Manli mounted the embryos with the epiblast layer facing downwards on a Willco 3cm glass bottom cell culture dish and covered them with 2 ml of low viscosity light silicon oil (viscosity 5cSt, Sigma 317667) to prevent drying out. I performed the experiments within one hours of mounting the embryos.

MYOSIN INHIBITION

For one of the experiment used to verify the working hypothesis, the embryo were treated with myosin inhibitors PBP and PCP and optically manipulated before and after the treatment. Dr. Chuai prepared 5h old embryos as described above and mounted on the cell culture dish. I performed trapping experiment for 30 min. Then Dr. Chuai lifted the embryos from the glass and injected 10μmolar PBP/PCP solution of between the embryos and the bottom cover glass. After an incubation time of 20min, I repeated the trapping experiments in the same region of the embryo measured before the injection.

LOCALISATION OF THE EMBRYO

Prior to the experiments, Dr. Chaui inspected the embryos with bright field and low magnification fluorescence microscopy to localise the Koller's sickle region. She marked the location of interest on the culture plate with a permanent marker.

Together with Dr. Chuai, we subsequently mounted the embryos in the TIR-Ph set-up and observed the embryo at low magnification. We scanned the samples in the x and y directions and later composed the images with a *Fiji* plug-in (MosaicJ) (see Figure 7.6(a)). For each location recorded at low magnification, we saved a picture of the sample as imaged in fluorescence with the 100x microscope objective to get a snapshot of the different cell shapes of the embryo at different locations (see 6.4c).

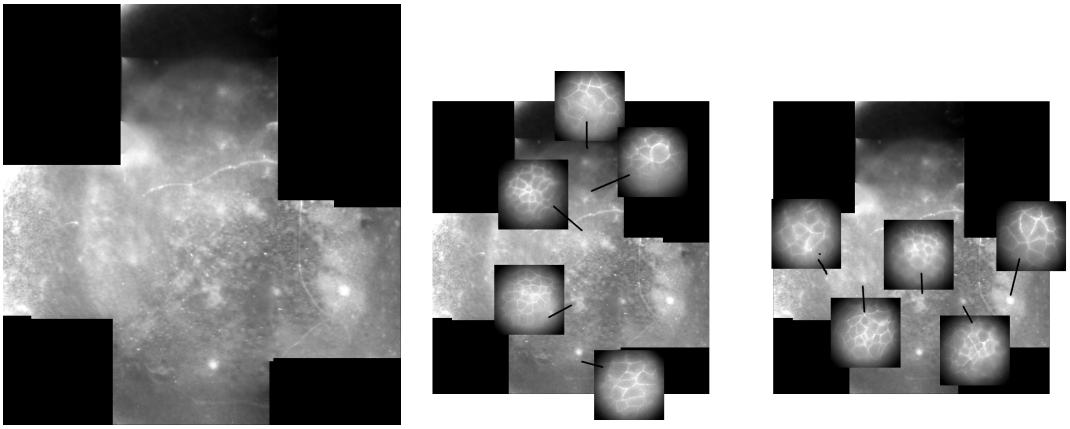

(a) (b) (c)

Figure 6.4: **Low magnification imaging of the chick embryo** – Mosaic reconstruction of chick embryo images collected by 4x MO (a), and corresponding 100x images (b-c)

6.3 ACQUISITION AND DATA ANALYSIS

The images collected through Matlab were saved as archival format video (mj2). Compared to the experiment conducted on Drosophila [61, 179], where a light sheet microscope was used, the images I collected for the chick embryo have lower signal-to-noise ratio because I used an epifluorescence microscope. With epifluorescence the sample is illuminated through many different planes, and light scattered from above and below the focal plane is collected by the camera. Because of the low signal-to-noise ratio, stan-

dard segmentation techniques, typically used for chick embryo images collected through light-sheet or confocal microscopy [166, 168], were not effective.

To overcome this issue, I defined a custom protocol to process the videos and to analysis the data:

1. each frame was filtered with a Gaussian function and the contrast of the image was stretched.

2. a kymograph for every location in the junction under study was generated. I scripted a custom kymograph function in Matlab to center the kymographs for slanted junctions.

3. the location of the junction was identified and its position in time relative to the initial rest position was saved. Typically this would be done by fitting each line of the kymograph with a Gaussian curve to obtain subpixel resolution. However, using a gaussian fitting would often fail to identify the correct location of the junction for low signal-to-noise images (as the fluorescence signal is more spread out in the image). Instead, I modified a *seam carving algorithm* and applied to the images. Seam carving algorithms are designed for content-aware resizing [181]: they look for the paths in an image which have minimal variation and remove them without distorting of the original image. The algorithm attributes a value for each pixel weighting it on the neighbouring pixels of the previous row in the image and then the path with lowest values are removed. I modified the algorithm to work for a video format, including evaluation of pixels in the previous frame together with the ones in the previous row. Finally, I saved the path with the lowest values, instead of removing it from the image. The seam carving approach outperformed the Gaussian fitting by better identifying the junction location (see Figure 6.5) and by faster execution speed, but did not provide subpixel resolution.

4. the location of the junction were converted from pixels and frame number to μm and seconds, and were fitted with the appropriate functions (sine for the *sine wave mode*, and exponential decay function as calculated by the visco-elastic model for the *Pull & Release mode*).

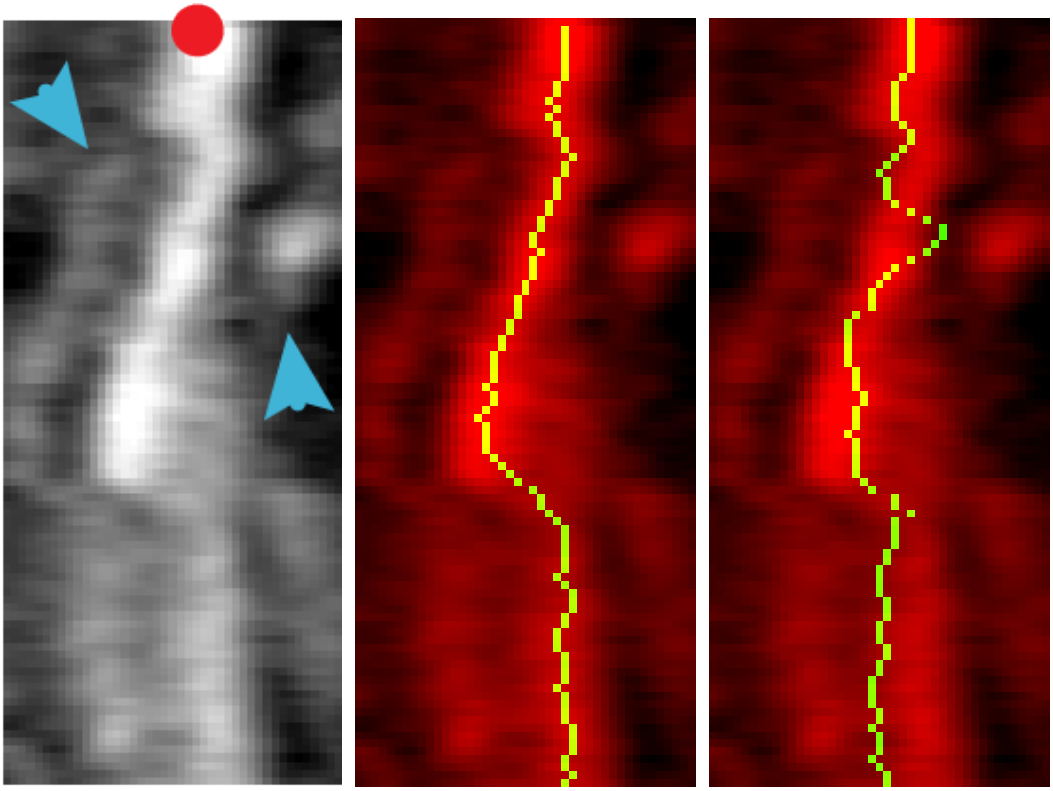

(a) Original (b) Seam Carving (c) Gaussian Fit

Figure 6.5: **Algorithms to determine the location of the junction** – (a) is a kymograph from the chick embryos data-set for the Pull & Release experiment. The red dot indicates the initial location of the junction. Addditional signal comes from two organelles in proximity of the junctions (blue arrows). The seam carving algorithm (b) outperforms the Gaussian fit (c) in determining the junction location

5. the data were aggregated and statistical analysis was performed. Specifically, I first tested the normality of the distributions by using the Anderson-Darling test (*adtest* function in matlab). Because the datasets failed the test (i.e. they are not normal), I performed significance tests with the non-parametric Wilcoxon Ranksum test (also called Mann-Whitney U test, *ranksum* function in Matlab).

6.3.1 trap stiffness characterization

There are three forces acting on an optically manipulated junction: the optical force displacing the junction, the drag force of the cytosol opposing the movement of the junction and the tension force in the junction acting to restore the junction to its rest position. A junction reaches its maximum deformation when the tension and the cytosol drag overcome the optical force; after this moment, the junction is lost from the trap and returns to its rest position.

To measure the tension in the junction, one would need to know both the optical force and the drag in the cytosol. The drag in the cytosol could be measured by performing rheology experiments: introducing fluorescence beads inside the cells and observing their Brownian motion. The optical forces, instead, need to be measured by evaluating the stiffness of the trap. I showed in Chapter 1 that the trap stiffness is affected by the shape and the refractive index of the object being trapped. In the case of trapping cell-cell junctions, none of these two parameters are known.

The authors of the studies on Drosophila worked around this issue by introducing fluorescence beads in the chick embryo. They evaluated the trap stiffness when using these bead in the cytosol and used these beads to push the junctions. They compared the maximum deformation of the junction achievable when using the beads with the one obtained directly manipulating the junction and used the proportion between this two values to scale the trap stiffness for the system tweezers-junctions from the previously measured stiffness on the beads..

Early in the process of trapping junctions in chick embryos, I realized that this method was not reliable for the chick embryos. In fact, I observed that small vesicular organelles in the proximity of the junction were following the movement of the trap, ultimately being the actual object pushing and deforming the junctions (Figure 6.6). This information invalidates the technique used for Drosophila: since the trapped vesicles vary in size from measurement to measurement, attributing the same stiffness value for all the junctions introduces an error in the estimation of the forces in the system.

A proposed solution to ensure reliable measurement of forces in cell-cell junction manipulation is to use a self-calibrating back focal plane interferometry technique to calibrate the trap stiffness. I have discussed in chapter 1, how this stiffness evaluation

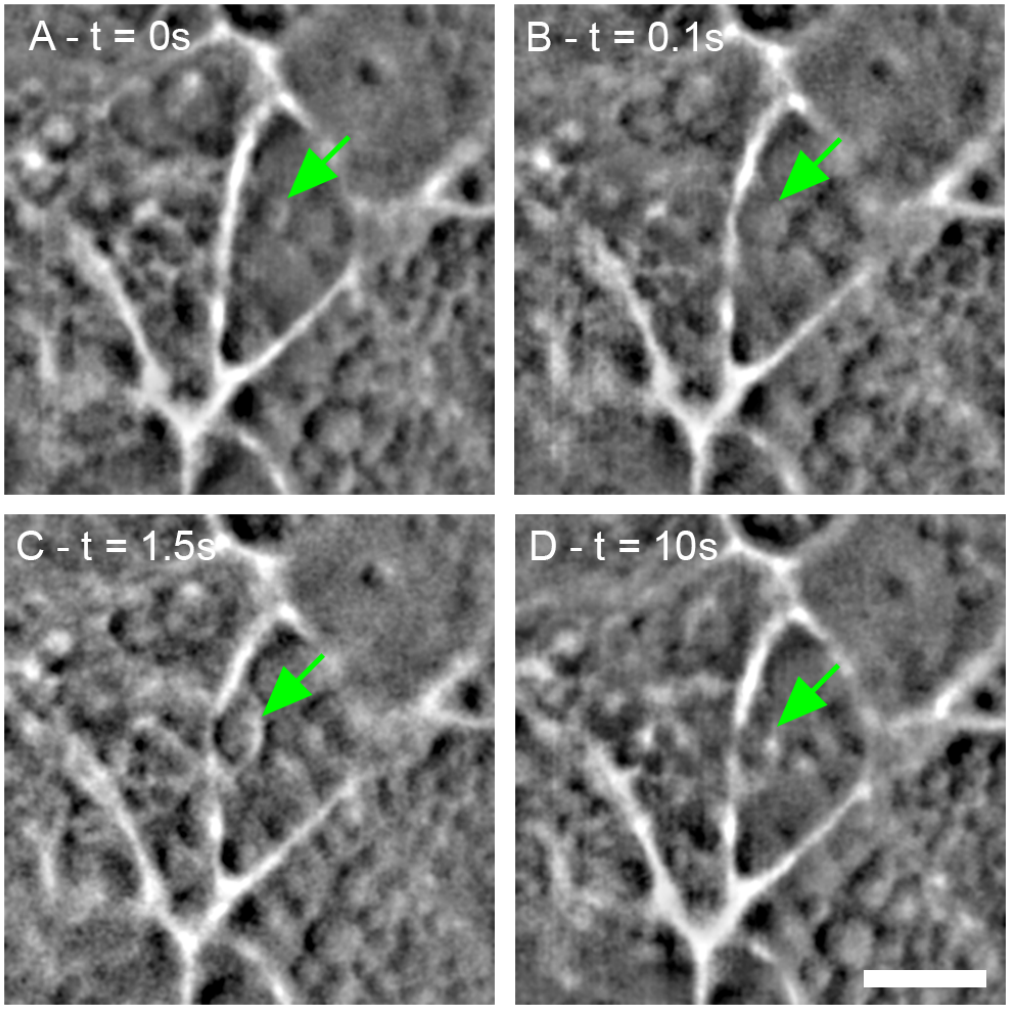

Figure 6.6: **Trapping organelles** – Sequence of Pull & Release experiment figures where an organelle (green arrow) is trapped and drives the deformation of the junction. (A) At time t=0, the trapping laser is off, and an organelle is visible in proximity of the junction. (B) Once the trap is turned on, t=0.1s, the organelle is attracted into the trap. (C) With the trap moving, the organelle pushes against the junction until it reaches the maximum deformation at t=1.5s. (D) After switching the trap off, the junction and organelle return to their rest positions, with the organelle adjacent on the junction's right side (t=10s). Scale bar indicates $5\mu m$.

approach works for the case of forward scattering interferometry, but in the chick embryos one would need to implement the technique in backward scattering because the laser interference is destroyed by scattering inside the tissue. Preliminary attempts to implement self-calibrating interferometry in backward scattering are reported in Appendix C. Unfortunately, further characterisation was needed to establish the technique so that it could be used for quantitative analysis.

For the above reasons, I did not directly measure any tension forces in the chick embryos. However, it was still possible to measure relative differences in the response of the embryo and compare the effects of different types of perturbations. Maintaining unchanged all the trap experimental parameters, such as laser power, distance travelled by the tweezers and duration of the experiment, and provided enough statistical data to account for the size variation of the vesicles in the system, I expected that higher tensions in the junctions would results in smaller deformation. I measured 40-100 junctions for each experimental condition.

6.3.2 VISCO-ELASTIC MODEL

Visco-elastic materials are characterized by manifesting both viscous and elastic response when subjected to a form of stress. An elastic material deforms when a stress is applied and immediately returns to its rest state after the stress is removed. A viscous material, instead, resists the applied stress and it deforms linearly with time. Biological materials are often described by using visco-elastic models, because when they are subjected to stress, their deformation is time-dependent but not linearly. To describe their behavior several viscoelastic models can be used, and the most common are the *Maxwell Model*, the *Kelvin-Voigt Model* and the *Standard Linear Solid Model* (SLS). These models are obtained by combining the equation for an elastic material and the equation for a viscous material under different configuration. For the Maxwell model, a purely elastic component of elastic constant E and a purely viscous component of damping coefficient η are regarded as acting in series on the system (Figure 6.7).

For the Kelvin-Voigt model, instead, a purely elastic component and a pure viscous one are considered to act in parallel (Figure 6.7). Finally, the SLS model is a compination

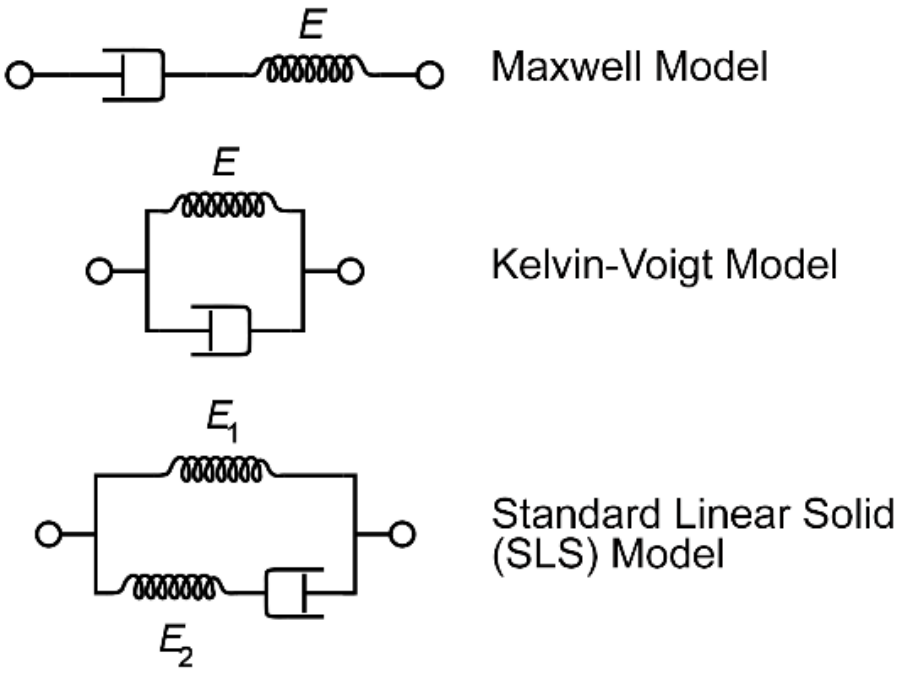

Figure 6.7: **Viscoelastic models** – Schematic representation of the Maxwell, Kelvin-Voigt and SLS models.

of the two, where a Maxwell component works in parallel with a second purely elastic component (Figure 6.7).

To describe how chick embryos junctions returned to their rest positions, I solved the differential equations for each of the models and fitted the junction with all them. I later compared the goodness of fit parameters to decide which model to use. As it can be deducted from Figure 6.8, the Maxwell model best fitted the majority of the data.

Specifically, the equations used for the Maxwell model are obtained considering that when the junction is deformed by a strain x, it is subjected to a tension force F_j that opposes the deformation to restore the junction to its original state. In term of Maxwell model equation, this means:

$$\frac{\dot{F}_j}{E} + \frac{F_j}{\eta} = \dot{x} \tag{6.1}$$

When the trapping laser is on, the optical force of the tweezers F_t is balanced by the tension force in the junction F_j and by the drag of the junction in the cytosol $\zeta\dot{x}$, where $\dot{x}$ is the velocity of the junction and ζ the cytosol damping coefficient:

$$F_j + \zeta\dot{x} = F_t \tag{6.2}$$

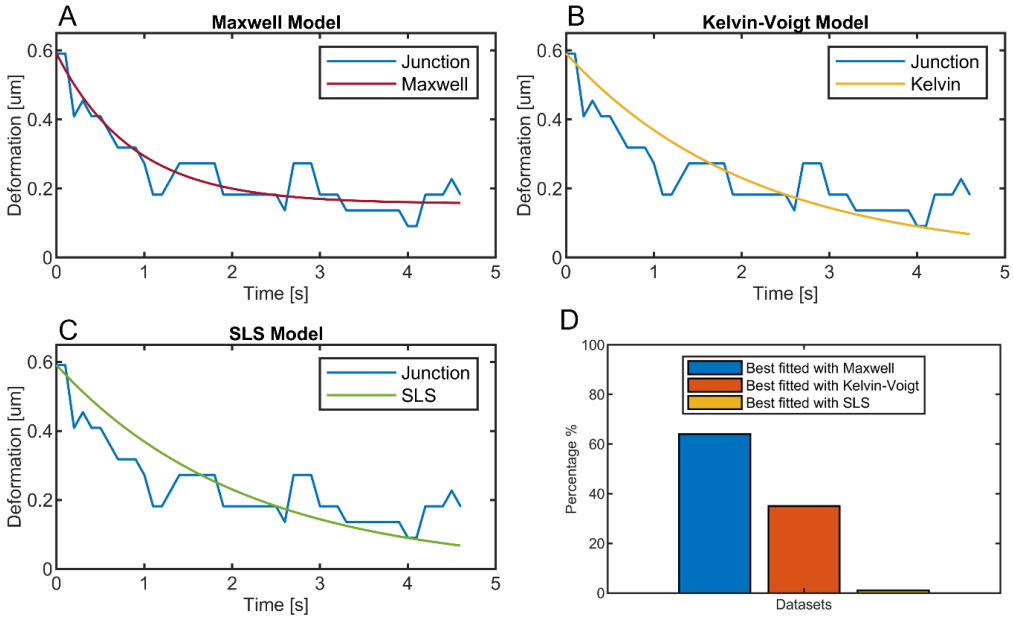

Figure 6.8: **Viscoelastic models fitting** – (A-B) Example of a junctional relaxation kinetics (blue line) fitted with Maxwell model (A), with Kelvin-Voigt model (B) and with SLS model (C). To decide the best fit, I compared the adjusted R-squared and the absolute error on the measured variables. For the junction in the example, the Maxwell fitting presented an Adjusted R-squared of 0.84 and absolute error on fitting variable of 0.07; the Kelvin-Voigt fitting presented an R-squared of 0.38 and absolute error on fitting variable of 0.57; the SLS fitting presented an R-squared of 0.35 and absolute error on fitting variable of 1E16. I concluded that the best fit was obtained by using the Maxwell model fitting. (D) By fitting datasets from the Push & Release experiments with all three models, the Maxwell model best fitted most of them. The major difference between the Maxwell and the Kelvin-Voigt model is that the first accommodates the irreversibility of the junction deformation, while the second provides a fitting that will always return to the rest position at 0. The data was based on analysis of 203 junctions in control experiments of various embryos.

This equation, combined with the Maxwell equation, could be used to calculate the tension in the junctions provided that F_t and the drag in the cytosol are known. Because during the time of the experiments, I did not successfully characterized the trap stiffness, nor I measured the damping component of the cytosol, a quantitative evaluation of the junction tension was impossible.

However, the Maxwell equation can still provide information on the kinetics of junctions. In fact, for the Pull & Release experiments, the trap is turned off after the junction was deformed. When the tweezers are off, the tension in the junction acts in order to restore it to the rest position, being balanced only by the drag in the cytosol:

$$F_j = -\zeta \dot{x} \tag{6.3}$$

Combining this equation with the definition of the tension force from Equation 6.1, I derived the differential equation that describes the dynamics of how the junctions return to their initial rest state:

$$\ddot{x} + \frac{E}{\eta}\dot{x} = -\frac{E}{\zeta}\dot{x} \tag{6.4}$$

$\frac{\eta}{E} = \tau$ and $\frac{\zeta}{E} = T$ have units of time and they represent the relaxation time of the junction and of the cytosol. The previous equation can be re-written as:

$$\ddot{x} + \frac{1}{\tau}\dot{x} = -\frac{1}{T}\dot{x} \tag{6.5}$$

The general solution to this differential equation is a single exponential curve with a relaxation time given by the combination of τ and T:

$$x(t) = \frac{c_1(\tau + T)}{\tau T} \exp\left(-\left(\frac{\tau T}{\tau + T}\right) t\right) + c_2 \tag{6.6}$$

c_1 and c_2 can be obtained by applying initial conditions. At t=0 (setting t=0 at the moment at which the junction escapes the trap), the junction is at a position x equal to its maximum deformation x_m and at t=0+ it starts moving towards its rest position with a velocity v_m that can be measured from the data. A particular solution therefore is:

$$x(t) = \frac{v_m(\tau + T)}{\tau T}\left(\exp\left(-\left(\frac{\tau T}{\tau + T}\right) t\right) + \frac{x_m \tau T}{v_m(\tau + T)} - 1\right) \tag{6.7}$$

I used Equation 6.7 to fit the experimental data of junctions moving back to their rest position with the *fit* function in Matlab and *Robust mode on*.

6.4 HIGH POWER DAMAGE IN THE EMBRYO

Finally, before moving on quantitative experiments, I wanted to evaluate what was the maximum laser power I could use without visible signs of damages in the embryo. By recording a timelapse of embryos exposed at increasing laser powers, I was able to detect visual signs of the damage that high laser power inflicted on the samples. When the embryos were subjected to laser powers $>$ 1W for a time of at least 60 seconds, the tissue deforms on a long range: the nodes between junctions are moved further apart in every directions, suggesting an overall relaxation in the tissue (see Figure 6.9). For laser power smaller than 1W, the embryo looked unaffected in the time-frame studied.

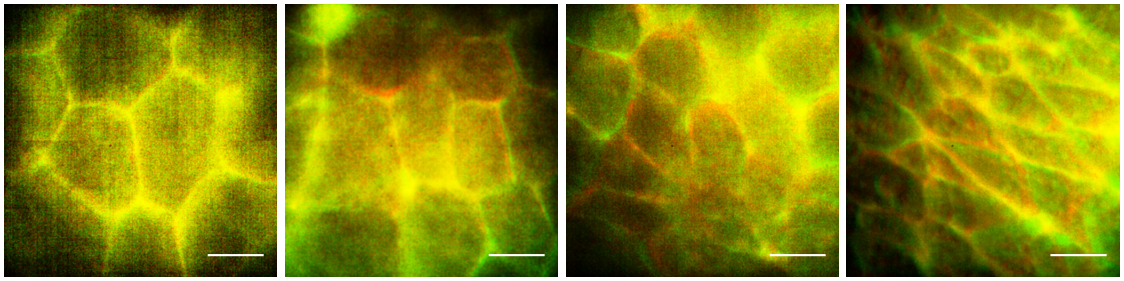

(a) 500mW (b) 1W (c) 1.5W (d) 2W

Figure 6.9: **Power damage to the embryo** – We portrayed in red the first frame and in green and blue following frames. For trapping laser powers $<$ 1 W, there were no visible signs of damage: the first frame (red) and the last frame (green) overlapped (a). For power $\geq$ 1W, there was a long range deformation in the embryo shown as a relaxation and dilation of the whole tissue (b-d) . Larger powers (not reported) bleached the sample almost instantaneously, possibly carbonating the sample. Black marks were visible at low magnification in bright field.

Additionally, I observed that when I used the "sine wave" mode, a fraction of the junctions followed the laser movement, but the amplitude of their deformation reduced over time. This behaviour was best fitted by using an exponentially decaying sine. I investigated this effect by comparing junctions subjected to sinusoidal motion with different parameters (power $<$ 1 W, power $\geq$ 1 W, duration $<$ 60s, duration $\geq$ 60s) and verified whether they would be best-fitted by a decaying sine wave (a sine wave multiplied by an exponential decay): the decay behaviour was predominantly observed after longer exposure to the laser and at higher powers (see Figure 6.10). This suggested that for higher power and longer exposures to the infrared laser, the behaviour of the junc-

tions changed. More investigation would have been required to manipulate the junction under those conditions.

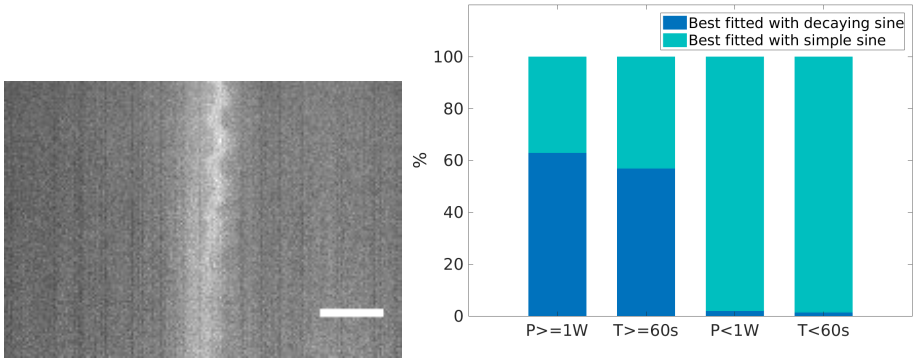

(a) (b)

Figure 6.10: **Stiffening of the junctions induced by laser power** – We show an example of kymograph of a measured junction where the deflection of the junction reduced over time (a). The junction was manipulated using 1W for 60 seconds. I fitted several junctions both with a simple sine and with a decaying sine. The decaying sine best fitted the junction deformation for higher powers and for longer measurement times (b).

Based on these findings, I chose a constant power of 750mW for the trapping laser (measured in the image plane) and a measurement cycle of 10 seconds for the Pull & Release experiments and of 30 seconds for the "Sine wave" experiments. This gave a good compromise between a measurable deflection of the tested junctions and absence of any obvious visible signs of damage.

It is, however, possible that the laser would still damage the embryo at 750mW, without any visible signs, and it is recommended to lower the laser power in future studies.

CONCLUSIONS

I successfully showed that it is possible to optically manipulate cell-cell junctions in chick embryos, thus extending the technique presented in literature for Drosophila [61, 179].

While describing the methods, I also highlighted how the tweezers trap organelles instead of the cell-cell junctions. This finding invalidates the technique used to measure tensions for the Drosophila study. In fact, the size, shape and refractive index of the

trapped object -none of which are known for organelles- determined the trap stiffness. If an organelle was the transducer of the optical force, keeping the laser power constant between experiments does not guarantee that the applied forces are constant.

To study the chick embryo samples, I also developed a new method to determine the junction location at every frame. By using a modified version of a *seam carving algorithm*, I could identify the junction with higher fidelity than by using a Gaussian fitting approach. It might be interesting to compare Gaussian fit and the used seam carving algorithm for images obtained through high resolution microscopy techniques.

In the next chapter, I will present the results obtained studying the chick embryos with the methodologies just described.

7

TENSION IN CHICK EMBRYOS JUNCTIONS: RESULTS AND DISCUSSION

Using the methods described in the previous chapter, I studied the deformation of chick embryos junctions when optically manipulated under different experimental conditions. Specifically, I wanted to determine if the presence of myosin light chains in the Koller's Sickle region of the embryo before the start of strick formation would result in increased tension in the junctions, and investigate the specific contribution of Myosin I and II.

7.1 OPTICAL MANIPULATION OF CELL-CELL JUNCTIONS

First I characterized the interaction between the junctions and the optical tweezers. I checked that the junctions were deformed by the presence of the trap, and that the measured deflections were not a results of other phenomena happening in the tissue. Therefore, I recorded the movement of the trap when the tweezers were on and when they were off and observed that without the trap I did not detect any movement of the junctions. Figure 7.1 shows an example of junction subjected to this study.

Before performing experiments to verify the working hypothesis, I also characterised the tweezers-junction interaction by changing the set-up parameters, such as laser power, trap distance and speed, and the temperature of the system.

POWER AND AMPLITUDE RESPONSE

For the study of Drosophila, it was reported that the response of the junctions saturates with increasing power and increasing amplitudes, i.e. it deviates from the linear relationship typical of Hooke's law [61]. I replicated their study for the chick embryos, using 3h old embryos where Koller's Sickle was not yet developed; I trapped junctions in random location and random orientation in the centre of the area pellucida. At the time of these experiments, the TIR-PH set-up was equipped to perform only in the "sine wave" operational mode with the stage moving. I also explored a combination of both

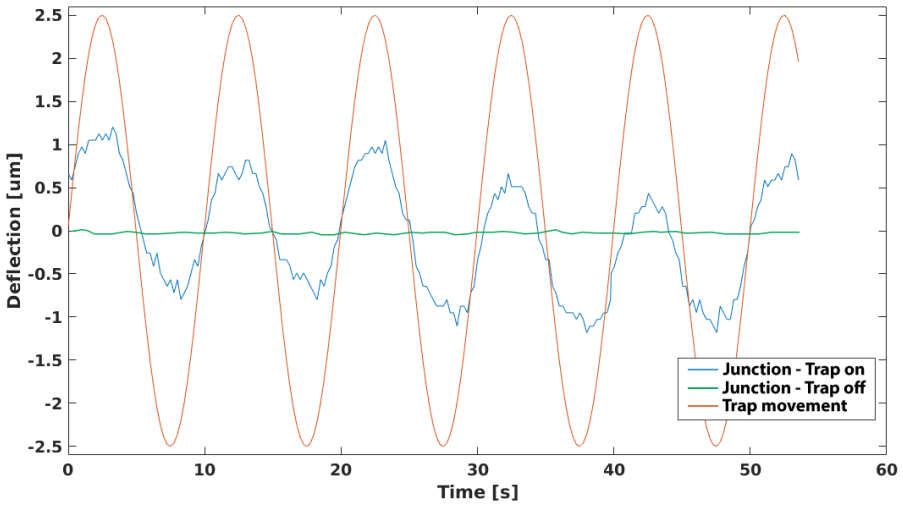

Figure 7.1: **Junction deflection** – Example of junction position being recorder in absence of the optical tweezers (green) and then in presence of optical tweezers moving with a sinusoidal motion (blue). The position of the tweezers when they were on is in red.

different powers and distances for the tweezers, to collect information about the best settings to use in later experiments. The set-up was not yet equipped with temperature control, so the measurements were performed at room temperature

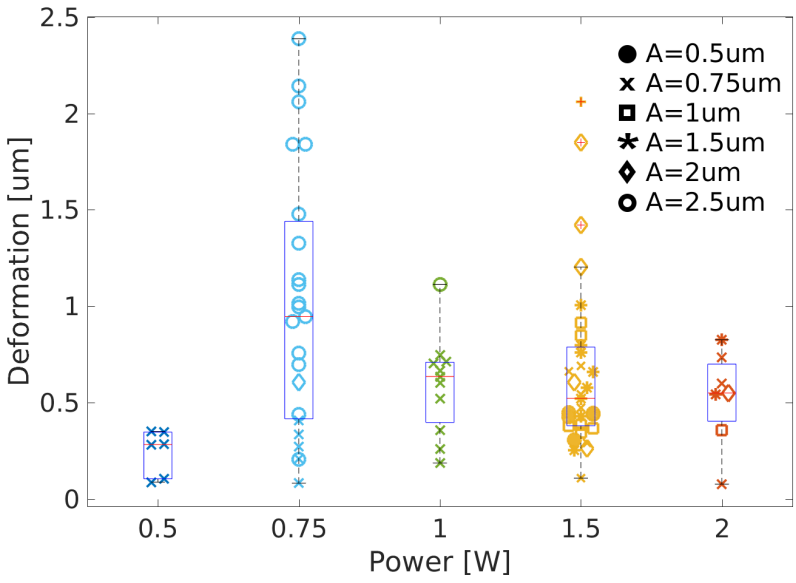

Figure 7.2: **Junction deflection VS power** – Deformations of junctions for 3h old embryos versus the trapping laser power. Different markers relate to different amplitude used for the oscillations of the tweezers. The only complete set of data was for A=0.75 μm, x marker.

While Figure 7.2 collectively does not show any trend in the relationship between laser power and junction deformation, looking at the amplitude A=0.75 μm for which all different power settings were applied, the measured deflections increased with power until 1W and then saturated. However, this observation is not significant due the low number of measurements. Furthermore, it is possible that the saturation is an effect of laser damage, as reported for laser power $\geq$ 1W (Chapter 6).

If the same data reported in Figure 7.2 are plotted against the distance moved by trap, referred to as amplitude, the measured deformation was proportional to the movement of the trap for all sine amplitude used (see Figure 7.3). This was in contrast with what reported in literature, as the relationship between junction deformation and laser amplitude was also observed to saturate for the case of Drosophila [61].

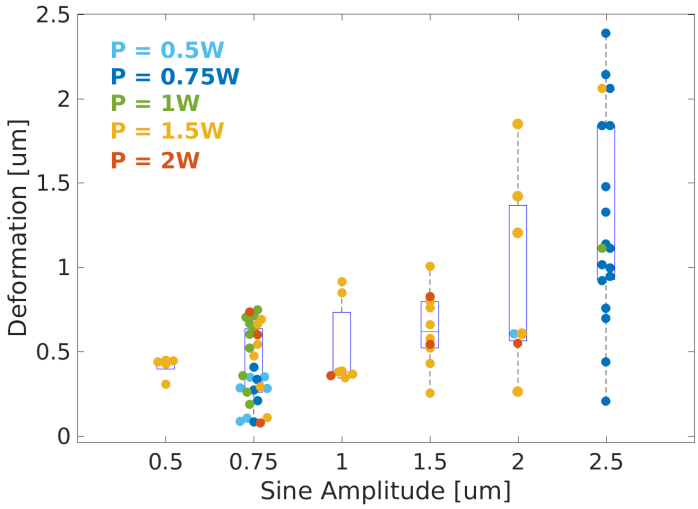

Figure 7.3: **Junction deflection VS amplitude** – Deformations of junctions for different 3h old embryos versus the amplitude of which the tweezers were moved. Different colors refer to different power of the trapping laser. The only complete set of data was for P=1.5 W (yellow color).

Finally, I would like to mention that using the stage to move the sample relative to the trap could have added artifacts in the final kymographs. In fact, before analyzing the samples, the frames needed to be re-aligned. For these reasons, the early measurements with the different powers and the different amplitudes were only used to decide the settings for later experiments and not to draw quantitative conclusions on the biology of chick embryos development.

FREQUENCY RESPONSE

The dynamics at which the junctions were deformed when the trap was moving at different speeds could provide information on the visco-elastic properties of the tissue. Therefore, I moved the trap with sine waves with different frequencies and observed the response of the junctions.

When I was performing this study, the TIR-PH set-up was equipped with the piez-actuated mirror: this improvement eliminated the risk of introducing artifacts in the analysis, but limited the maximum distance that could be traveled by the trap to 2.6μm. For this experiment, I also used 3h chick embryos where Koller's Sickle was not yet developed and I trapped junctions in random location and random orientation in the centre of the area pellucida. The obtained data are reported in Figure 7.4.

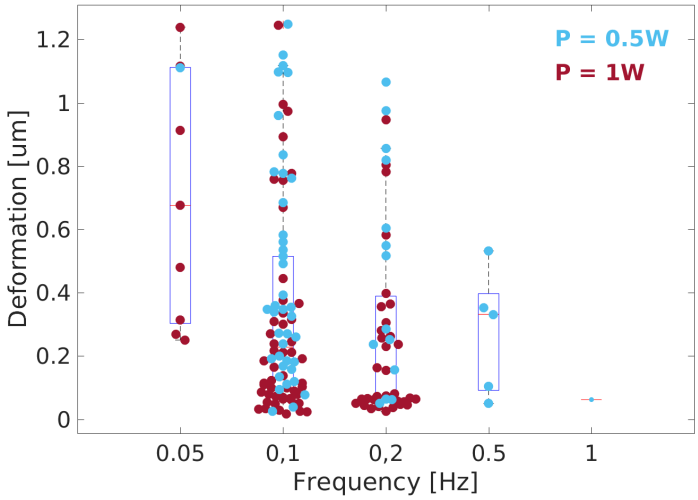

Figure 7.4: **Junction deflection VS frequency** – Deformations of junctions for different 3h old embryos versus the frequency at which the tweezers were moved. Different colors refer to different power of the trapping laser.

Figure 7.4 shows that with increasing frequency, the junction was unable to follow the trap movement as the motion is dominated by viscous behaviour. From this datasets, the "Sine wave" operational mode was set to operate at a frequency of 0.1Hz.

TEMPERATURE EFFECT ON TENSION

When I introduced a custom-made incubator to the TIR-Ph set-up, I performed a quick test to explore the effect of temperature on the embryo. For this study, I performed

Pull & Release experiments on two 3h old embryos, measuring each embryo both at 25° C and 37° C (see Figure 7.5).

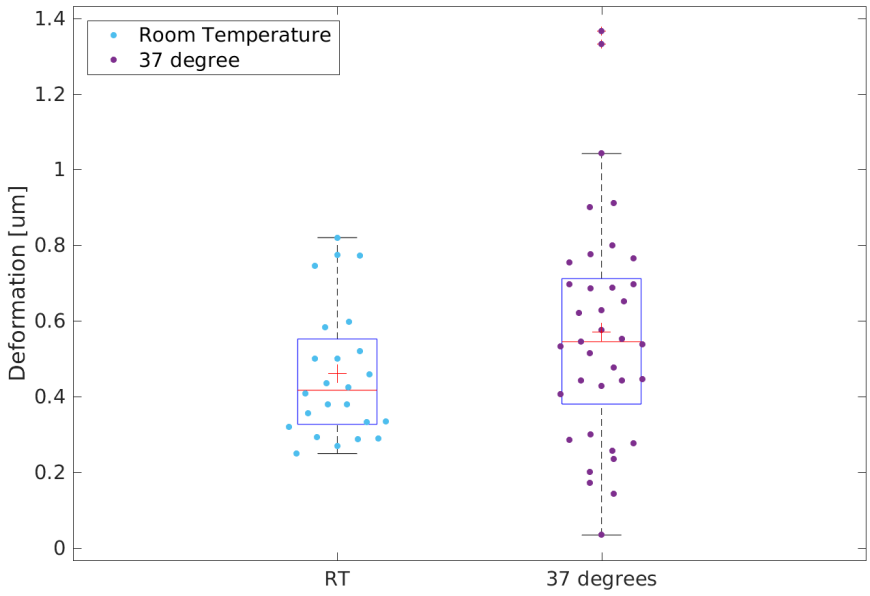

Figure 7.5: **Temperature effect on junction tension** – Aggregated data on two different samples measured at 37 degrees. I used the Pull & Release operational mode. The embryos were 3h old after incubation with no visible Koller Sickle. I measured in the centre of the area pellucida.

There was a small difference in the response of the two datasets, with the measurement taken at 37 degrees showing a larger variance and slightly bigger deformations. The difference between the two measurements, however, was not significant (p-value > 0.05). Further experiments should aim at verify if the suggested difference is a signature of *active* versus *passive* tension components. After the introduction of the incubator, I performed all the following experiment keeping the embryos at 37 degrees Celsius.

7.2 HIGH JUNCTIONAL TENSION IN MESENDODERM CELLS

Directional junctional tension perpendicularly to the A/P axis is one of the candidate mechanisms to be responsible for the elongation of the streak through cell-cell intercalation (see chapter 5 - Figure 5.2) [168]. To verify this hypothesis, I studied the deformation of the mesendoderm junctions perpendicular to the A/P axis and compared the results with junctions in different conditions. In fact, if the hypothesis that these junctions are

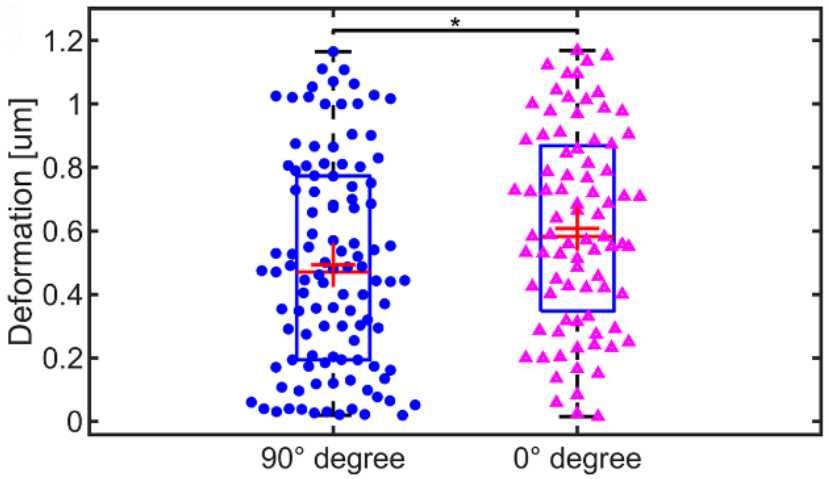

Figure 7.6: **Deformation of junctions aligned in different directions** – Boxplot and distribution of the maximum deformation of junctions as fitted from the sine wave experiments in cell junctions with different alignment respect to the A/P axis: junction perpendicular to the A/P axis, and therefore aligned to the super-cellular Myosin cables (blue filled circle, n=109 collected over 4 embryos) had a median deformation of 0.45 μm, while junctions parallel to the A/P axis (pink empty triangles, n=84 collected over 4 embryos) had a median deformation of 0.6 μm. – Significance test: * indicates a p-value < 0.05

under higher junctional tension is true, they would deform less than elsewhere in the embryo when optically manipulated.

First, I investigated if junctions perpendicular the A/P axis –and therefore aligned with the myosin cables– were more under tension than junctions oriented parallel to the A/P axis in the posterior of the embryo (in the region of the Koller's Sickle). The measurement were done on embryo 5h old, before the formation of the streak. I found that the junctions parallel to the A/P were deformed significantly more than junctions in the perpendicular direction (see Figure 7.6). When this first study was performed, the set-up was only equipped with the "Sine wave" mode with the piezo-actuated mirror. This suggests that the junctions aligned with the myosin cables were under higher tension than the others.

To further support this finding, I applied the optical tweezers to junctions aligned perpendicularly to the A/P axis in the posterior of the embryo (in the Koller's Sickle region) and to junctions with the same alignment but located in the central part of

the embryo. The junctions were measured in the centre and the posterior of the same embryos and then the results were aggregated over different repeats. I used the "Pull & Release" operational mode, making it possible to collect more data in a shorter period of time. The dataset referred to as "posterior" in Figure 7.7 include also data measured during other experiments that were taken under the same experimental conditions, i.e. same parameters of the trapping laser and same type of junctions (junctions in the posterior of the embryo aligned perpendicularly the A/P axis).

The two collected data-sets show that the maximum deformations for the cells in the posterior of the embryo was significantly smaller than the junctions in the centre of the embryo (Figure 7.7): only 0.39 μm (median, n=203, 90% Confidence Interval CI [0.13 μm, 0.65 μm]) compared to 0.58 μm (median, n=57, 90% CI [0.32 μm, 0.99 μm]). By using the Maxwell visco-elastic model described in the previous chapter, I also extracted the relaxation time for each junction. In this case, the two distribution were not significantly different, with median values of 0.7s (n=203, 90% CI [0.3s, 3.1s]) and 0.6s (n=57, 90% CI [0.2s, 2.8s]) for junctions in the posterior and the central area respectively. Thus, the observed differences in the deformation of junctions located in the central and the posterior areas of the embryos suggested that the junctional tensions in these areas were different.

Finally, I also compared the deformation of junctions of young embryos (manipulated before they manifested the Koller's Sickle) with the ones obtained from junctions measured in the posterior area of the previous experiment. For the younger embryos, I measured junctions aligned randomly as an A/P axis is indistinguishable in the 3h old embryos. The results from this experiment agreed with the previous ones: optical forces were able to cause larger deformations on the young embryos, suggesting once again that mesendoderm junctions perpendicular to the A/P axis were under more tension.

7.3 EFFECT OF MYOSIN INHIBITORS

The junctions of mesendoderm cells aligned perpendicularly to the A/P in the posterior of 5h old chick embryos were deformed less than any other junctions measured. These junctions are aligned along the direction of supercellular myosin II cables. Thus, I wanted to investigate the role of myosin I and myosin II in these junctions. It was

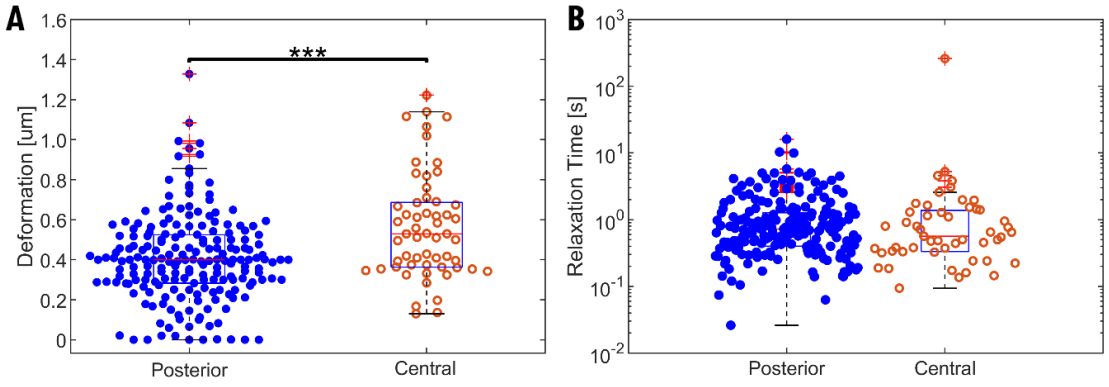

Figure 7.7: **Deformation of junctions in different areas of the embryo** – (A) Boxplot and distribution of the maximum deformation of junctions measured in the posterior (blue dots) and in the central area of the embryo (orange circles). (B) Boxplot and distribution of the relaxation times. In the posterior area, a median deformation of 0.39μm was measured, while in the central area the median deformation was 0.58μm. The measured relaxation times for this data set are 0.7 s and 0.6 s for the posterior and the central area respectively. The data for the posterior area were aggregated from 10 different embryos (n=203). The data for the central area were aggregated from 3 different embryos (n=57). *** indicates a p-value <0.001.

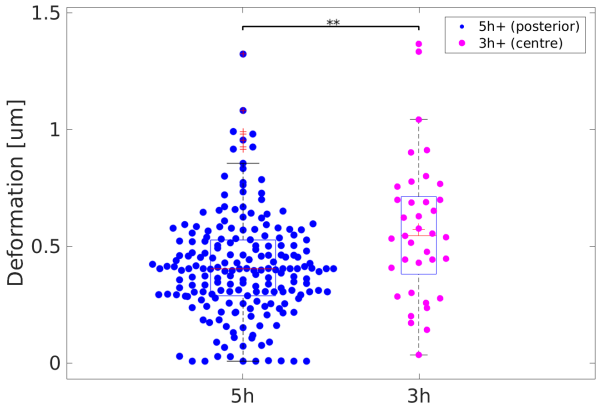

Figure 7.8: **Deformation of junctions in embryos of different ages** – Boxplot and distribution of the maximum deformation of junctions measured in the posterior of 5h old embryos (blue filled circle, n=203) and in the centre of 3h old embryos (pink circles, n=37). Median values for the deformation are 0.39μm and 0.59μm for the 5h old and the 3h old embryos respectively. The data for the 5h old embryos were aggregated from 10 different embryos ("Posterior" in Figure 7.7), while the data for the 3h old embryos were aggregated from 2 different embryos. ** indicates p-values <0.01.

reported that inhibiting myosin II with the use of pentabromopseudilin (PBP) resulted in inhibition of directional cell intercalation and streak formation; similarly inhibiting myosin I with the use of pentachloropseudilin (PCP) resulted in a strong inhibition of myosin II activity and the subsequent block of streak formation.

I wanted to study how these two specific inhibitor, PBP and PCP, affected the junction of mesendoderm cells aligned with the myosin cables. With the Pull & Release mode, I measured the deformation of the junctions before and after the introduction of a solution of 10 $\mu molar$ of PBP or PCP. The Control data for this experiment include both the data measured on embryos that were later treated with the inhibitors and data measured on the posterior of other embryos. This is the same dataset used in Figure 7.7.

I measured larger deformations after the embryos were treated with myosin I and myosin II inhibitors (Figure 7.9): the maximum deformation was 0.71μm (median, n=88, 90% CI [0.44 μm, 0.99 μm]) and 0.62μm (median, n=132, 90% CI [0.35 μm, 0.95 μm]) for the PBP and PCP treatment respectively, almost doubled from the 0.39μm (median, n=203, 90% CI [0.13 μm, 0.65 μm]) deformation of the control data.

The significant difference is confirmed in the measurement of the relaxation time, as calculated from the visco-elastic model: the data show a median of 1s for the PCP (median, n=132, 90% CI [0.4s, 3.1s]) and PBP (median, n=88, 90% CI [0.3s, 2.3s]) case compared to the 0.7s measured in the case of control junctions. This suggests a stronger contraction activity in control embryos than after they were inhibited. This results suggests that both myosin I and myosin II contribute to the increased tension in the junctions.

7.4 DISCUSSION

Optical manipulation without the introduction of external probes in a complex system such as a developing chick embryo is a interesting results. Not only have I extended this technique from Drosophila to chick embryos, but I have also measured significant differences in cell-cell junctional tension for junctions under various conditions.

It is important to comment on the observation that vesicular organelles in proximity of the junctions were trapped by the tweezers and they were ultimately the objects pushing the junctions (as reported in the previous chapter). This observation is novel to

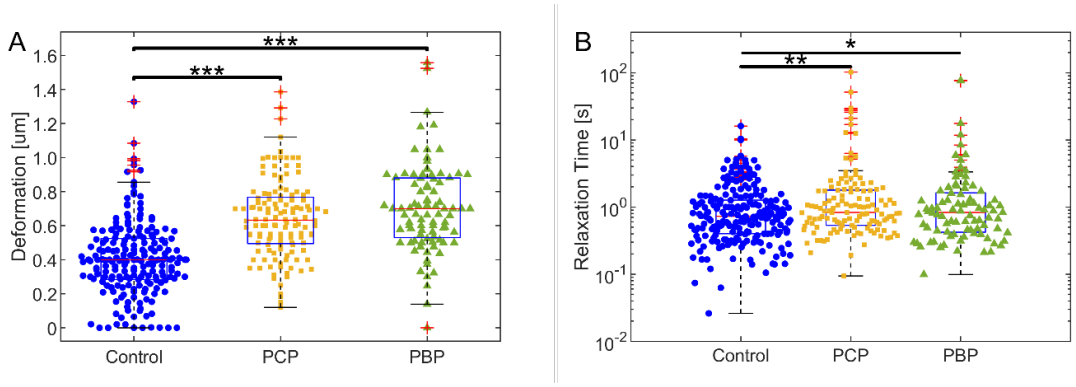

Figure 7.9: **Deformation of junctions in embryos treated with myosin inhibitors** – Boxplot and distribution of the maximum deformation (A) and of the relaxation time (B) of junctions measured in the posterior embryos before (blue dots, n=203) and after being treated with PCP (yellow squares, n=132) or PBP (green triangles, n=88). Median values for the deformations are 0.39μm, 0.62μm and 0.71μm for the control, the PCP and the PBP data sets respectively. Median values for the relaxation times are 0.7s for the control sample and 1s for both the PCP and PBP treated samples. The control data were aggregated from ten different embryos, while the data for PBP and PCP are aggregated from three different embryos each. * indicates p-values <0.05; ** indicates p-values <0.01; *** indicates p-values < 0.001.

this technique and was never reported for the case of optical manipulation in Drosophila. The main consequence of the trapping of the organelles is that the trap stiffness varied between measurement, as it depended on the size, shape and refractive index of the organelles. This made it impossible to obtain a quantitative value for the tensions in the tissue. To calibrate the optical forces, and therefore the tension i the junction, the trap stiffness could be obtained by recurring to a self-calibrating approach (as the one described in Chap. 1).

Despite the large variation of the datasets, possibly caused from trapping organelles of unknown size and shape, with enough data points it was possible to achieve significant results. As an attempt to reduce the variance and to check for additional effects, one could think of searching for a correlation between the maximum deformation of the junction and the junction's length. Figure 7.10 shows that no correlation was found between the deformation and the length of the junctions.

The significant differences found between junctions measured in different conditions are:

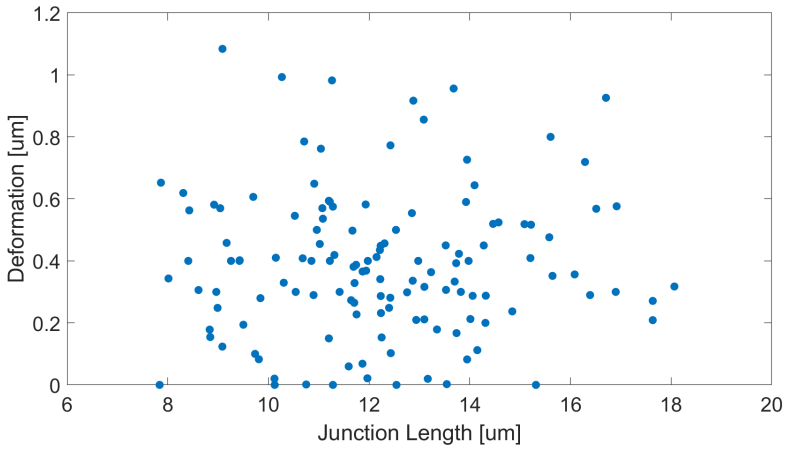

Figure 7.10: **Deformation of junction versus junction's length** – Plotting the deformation of the junctions against the junction's length show that there is not correlation.

- junctions in the posterior of the embryo aligned along the direction of myosin cables, i.e. perpendicular to the A/P axis, were deformed less than junctions aligned along the A/P axis;
- junctions in the posterior of the embryo aligned perpendicularly to the A/P axis, in the Koller's Sickle region, were deformed less than junctions in the centre of the area pellucida;
- junctions in the posterior of the embryo aligned perpendicularly to the A/P axis were deformed less than junctions in younger embryos;
- junctions in the posterior of the embryo aligned perpendicularly to the A/P axis were deformed less than similar junctions in embryos treated with myosin inhibitors, PCP and PBP; they also presented shorter relaxation times.

To interpret the results, I assumed that the maximum deformation produced by the optical tweezers for a given junction is inversely proportional to its stiffness. Similarly the faster the junctions return to their rest position, the higher the stiffness. By this assumption, the results reported support the original hypothesis that myosin acculumation in the intercellular cables induce directional intercalation by increased tension.

The inhibitor experiments confirmed that myosin II activity is a major determinant of junctional tension. Furthermore, inhibition of myosin I activity results in a large

decrease in junctional tension, consistent with its reported effect on myosin II cable formation [168].

Looking at the visco-elastic model, other important conclusion can be drawn: the fact that the data in all experiments were on aggregate best fitted with a Maxwell viscoelastic model informs that the duration of the perturbation might affect the irreversibility of the junction deformation. The Maxwell model, compared to the other two models evaluated, best described the case in which the junctions returns to a different position close to the initial rest position but not exactly the same. In the case of Drosophila, a similar irreversibility of the deformation was observed; it was also found that such irreversibility depended on the duration of the perturbation [179]. An irreversibility index I can be defined from the ratio between the position of the junction extracted at infinite time (as extracted from the Maxwell equations) and the maximum deformation (Figure 7.11(a)).

For the case of the "Pull & Release" experiment, the junctions reached a maximum deformation when the optical forces were balanced by the tension of the junction themselves. If the tension was low, then the junctions would remained trapped until the tweezers were trapped off. But if the tension was higher enough to overcome the optical forces, the junction could "escape" the tweezers and return to the original state while the optical tweezers were still on. Thanks to this effect, I could correlate, similarly to how was done in the Drosophila study, the irreversibility of the junctions versus the time at which they escaped the tweezers. Figure 7.11 shows that when the junctions escaped the tweezers in the first 5 seconds, irreversibility effects were minimal, and they only became noticeable when the junctions followed the trap for longer. But the application of the myosin inhibitor triggered this irreversibility viscous behaviour even after smaller perturbation times: thus, it is possible that myosin lower the viscous time constant of the junctions.

The study of the relaxation time as extracted from the fitting through the visco-elastic model can also provide interesting insights on the chick embryo development. The relaxation time I have reported, $t_{relax} = \frac{\tau T}{T+\tau}$, derives from the viscoelastic properties of the junctions themselves, T, and of the cytosol opposing to their motion, τ. Because the cytosol remained unchanged during all the experiments, it is safe to assume that the difference in relaxation times were due to differences in the viscoelastic properties

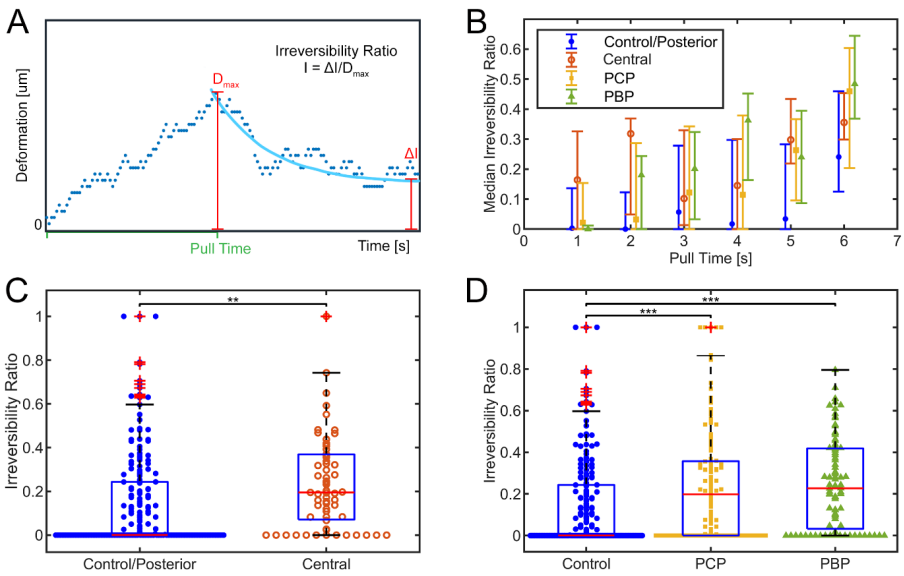

Figure 7.11: **Irreversibility in deformed junctions** – (A) Definition of irreversibility index I: the ratio between the position of the junction after being pulled at infinite time ΔI (as measured through the Maxwell model) and the maximum deformation of the junction (red lines), (B) Median Irreversibility ratio as function of pulling time. The data were aggregated for intervals of 1 second (Pull time is indicated in green in subfigure A). Error bars represent the 25 and 75 percentiles. (C-D) Boxplot and distribution of the irreversibility ratio of controls (blue filled circles, n=203) compared with that of junctions measured in the central area of the embryo (C, empty circles, n=57) and compared with that measured in embryos treated with Myosin inhibitors PCP (D, yellow squares, n=132) or PBP (green triangles, n=88. ** indicates p-values <0.01; *** indicates p-values < 0.001.

of the junctions. No substantial difference was found in the case of the relaxation time of junctions in the posterior area of the embryo versus junctions in the centre of the embryo, suggesting that this technique is incapable to detect small differences in the dynamics of the junctions.

7.4.1 PROSPECTIVES AND FUTURE EXPERIMENTS

The presented results contribute to a better understanding of the chick embryos developments, but more studies are fundamental to support these findings and further improve the theory of gastrulation.

For example, I failed to show that local changes in tension would results in additional accumulation of myosin as expected from the hypothesis of induced directional intercalation that I wanted to verify with this study. To observe the myosin accumulation, one would need to perturb the system on a longer time-scale (several minutes) while monitoring of the myosin activity in-vivo. Given appropriate conditions in the samples, longer observation times could reveal if a myosin accumulation results in induced contraction of neighbours junctions, and eventually in intercalation.

Performing experiments on longer time-scales would be beneficial also to confirm the study on the irreversibility effects of the perturbations. In Drosophila, it was shown that the irreversibility was depended on the actin network of the cytoskeleton [179], and it would interesting to study similar effects on the chick embryos.

Future investigations should focus on the determination of the trap stiffness, to obtain absolute value of the junction tensions. This involves analysing the organelles being trapped; it would be interesting to understand what type of vesicles they are and to extract information on their average size, shape and refractive index. Once the tweezers' stiffness is know, the tensions could be measured by fitting the data with the Maxwell model with a parameter for the drag in the cytosol. An independent measurement of the viscous properties of the cytosol, that can be obtained by measuring the Brownian motion of a bead injected in the embryo cells, would support verifying the values measured for the tensions.

Finally, the technique could also be used to map the embryos in different location and at different developmental stages.

While the technique can be improved as described, this study was a fundamental step to establish optical manipulation in chick embryo. Optical tweezers, together with oil droplet, FRET and laser cutting, can be used to extract information on the physics of tissue even with complex biology such as the development of chick embryos. Paired with statistical methods based on the observation of long range phenomena, e.g. observation through light-sheet microscopy, the optical manipulation of cells in living embryos can contribute to answer questions about gastrulation and development in general.

Part III

CONCLUSION

8

CONCLUSIONS

The idea that sciences are interconnected is rooted in our cultural heritage, and yet the education and research landscape nowadays is very fragmented. Scientists tend to explore a very specific subject, diving deep in the field of their research but rarely extending their expertise in different topics. However the latest years have seen a trend of the research community to move towards interdisciplinary sciences and towards the idea of a more interconnected knowledge.

Optical tweezers are one of the many example where physics has met with life sciences to answer complex questions. This thesis described the technique and its potentials (Chapter 1), how optical tweezers could be improved (Chapter 2-3) and some key applications in biology, especially at cellular (Chapter 4) and tissue level (Chapter 5-7).

HIGH STRENGTH PHOTONIC TWEEZERS

The range of forces for conventional optical tweezers is quite large, spanning from tenths to hundreds of pN, but in cellular biology forces often overcome the nN. Therefore, I worked to obtain high strength optical tweezers with the aim to achieve nN forces. I employed photonically structured microspheres, that I synthesised and improved. I also suggested proof-of-concept studies to highlight their advantage in biological applications, from how easy they can be functionalised (presented for the case of T-Cells) to how they could access new type of observations (suggested with the experiments on Dictyostelium).

OPTICAL MANIPULATION OF CELL JUNCTIONS IN CHICK EMBRYOS

An interesting branch of biology where optical tweezers have been rarely used is the study of tissues. With the study on junctional tension in chick embryos, I demonstrated that the tweezers can optically manipulate components inside living tissues without the

need of introducing external probes. Furthermore, I contributed to establish the use of optical tweezers for chick embryos, to define a successful procedure for the analysis of the results and to collect the first significant data for this type of samples.

With the work presented on this thesis, I believe that I have pushed the boundaries of optical trapping and I have presented landmark experiments useful for future applications of the technique. And yet, I have only scratched the surface of the possible biology applications that have opened along this journey. But perhaps this is the way of science: *"one never notices what has been done; one can only see what remains to be done." (cit. Marie Sklodowska Curie [182])*

A

SET-UP CHARACTERISATION AND COMPONENTS

LASER CHARACTERISATION

The characterisation of the trapping system consists of:

- Characterisation of the laser shape, to guarantee a Gaussian shape (mode TEM_{00})
- Characterisation of the power stability of the laser
- Characterisation of the polarising beam splitter (PBS)
- Characterisation of the transmission properties of the optical elements in the system
- Calibration of the camera

First the IR laser has been characterised using a Thorlabs power meter (PM100D). In Figure A.1, the average data from the knife edge measurement are reported and fitted with an error function; the first derivative of the data is presented on the right and fitted with a Gaussian. An average diameter of 5.76 $\pm$ 0.04mm is measured. The power stability of the laser was measured monitoring the output power variation during a period of one hour, with the same power meter. The relative change in power does not exceed 0.9% of the measured power.

The knife edge measurement was performed for the 488nm laser too. The graph is omitted for brevity. The knife edge showed a laser diameter of 0.78 $\pm$ 0.01 mm.

Using the same power meter, the PBSs have been characterised, measuring the transmitted and the reflected power each rotation of 5 degree of the half wavelength (HW)
.

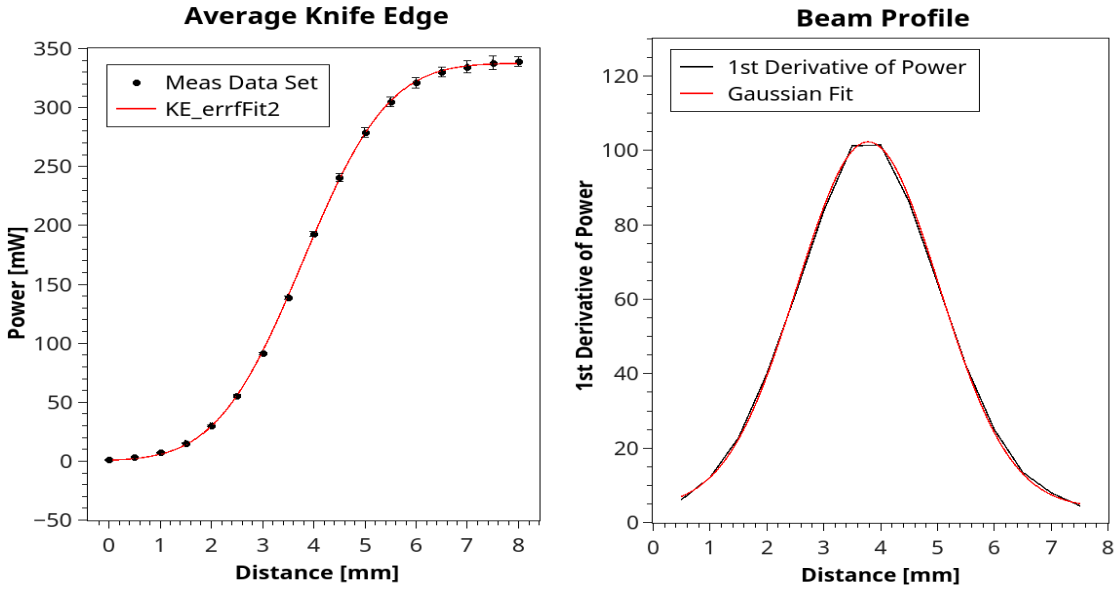

(a) (b)

Figure A.1: **Knife edge result for 1070nm laser** – Result of the Knife Edge measurement for the 1070nm laser fitted with a custom written Error Function (left) and its derivative fitted with a Gaussian (right).

CAMERA CALIBRATION

A calibration of the camera pixel was obtained making use of a 1mm grid printed on glass with 10μm minimal division from Thorlabs (shown in Figure A.2). A conversion 1μm:21.3pixels is found.

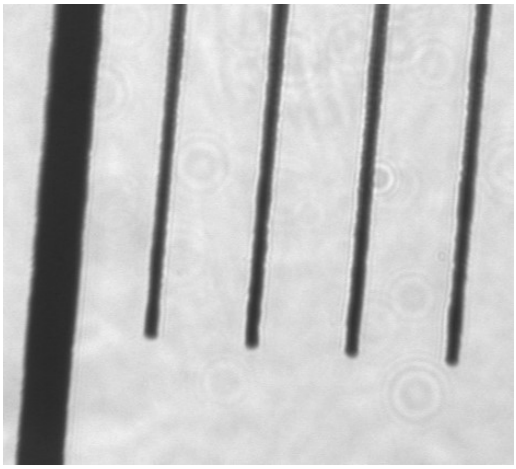

Figure A.2: **Camera calibration grid** – Image of the scale used for the camera calibration. Given that each division measures 10μm, it is found that 1 um is equal to $\sim$21.3px.

LIST OF TIR-PH COMPONENTSWe report a list of the most important components of the TIR-Ph set-up - see Figure 6.2 for reference:

Lasers

1070NM IPG Photonics ytterbium doped fibre laser emitting in the infrared (IR) with a 1070nm wavelength. Tuneable power up to 10W.

488NM 488nm Coherent Sapphire laser with fixed output power of 200mW.

Optical elements

OBJ. 100X	Nikon CFI Apochromat TIRF 100XC Oil, NA=1.49, W.D.=0.12 mm
OBJ. 4X	Zeiss Achroplan 4x, air immersion, NA=0.1, W.D.=11.1mm
L1	LA7255-C (Thorlabs) - Plano-convex, AR Coating 1050-1700nm, F= 75mm
L2	LA4380-C (Thorlabs) - Plano-convex, AR Coating 1050-1700nm, F= 100mm
L3	LA4102-C (Thorlabs) - Plano-convex, AR Coating 1050-1700nm, F= 200mm
L4	LA4380-C (Thorlabs) - Plano-convex, AR Coating 1050-1700nm, F= 100mm
L5	LA4148-A (Thorlabs) - Plano-convex, AR Coating 350-700nm, F= 50mm
L6	LA4102-A (Thorlabs) - Plano-convex, AR Coating 350-700nm, F= 200mm
L7	LC1582-A (Thorlabs) - Plano-concave, AR Coating 350-700nm, F= -75mm
L8	LA1050-A (Thorlabs) - Plano-convex, AR Coating 350-700nm, F= 100mm
L9	LA1131-A (Thorlabs) - Plano-convex, AR Coating 350-700nm, F= 50mm
L10	LA1509-A (Thorlabs) - Plano-convex, AR Coating 350-700nm, F= 100mm
TIRF LENS	LA4874-A (Thorlabs) - Focal length 150mm
DM_{trap}	DMSP950 (Thorlabs) - 950nm cut-off
DM_{tirf}	ZT488rdc (Chroma) - transmit above 498nm
DM	DMLP490 (Thorlabs) - 490nm cut-off
BANDPASS	ET750sp-2p8 (Chroma) - 750 cut-off

EDGEFILTER BLP01-488R-23.3-D (Semrock) - transmits above 500nm

PBS 1070NM CCM1-PBS25-1064 (Thorlabs)

HW1070 WPH05M-1064 - halfwave plate at 1064nn

PBS 488NM CCM1-PBS251 (Thorlabs)

HW488 AHWP05M-600 (Thorlabs) - achromatic halfwave plate 400-800nm

IR MIRRORS BB1-E03 (Thorlabs) - Dielectric mirrors, 750-1100 coating

AG MIRRORS PF10-03-P01 (Thorlabs) - Protected silver mirrors

Optomechanical elements

SAMPLE STAGE MDT630B (Thorlabs) - Thorlabs MAX302/M NanoMax Stage, 3 Differential Micrometers + Piezo Controller

STEERING MIRROR MOUNT POLARIS-K1S2P (Thorlabs) - Polaris Kinematic Mirror Mount, 2 Piezoelectric Adjusters

MIRROR MOUNTS KCB1C (Thorlabs) - Right-Angle Kinematic Mirror Mounts for cage system

TIRF/EPI MIRROR STAGE MT1 (Thorlabs) - Single Axis Translation Stage with Standard Micrometer

TIRF LENS MOUNT CXY1 (Thorlabs) - 30mm Cage XY Translation Mount

DIAPHRAGMS SM2D25D (Thorlabs) - Ring-Actuated Iris Diaphragm

4X MO MOUNT SM1Z (Thorlabs) - 30mm Cage Z-Axis Translation Mount

BAND PASS MOUNT CFH2 (Thorlabs) - 30mm Cage Removable Light-Tight Filter Holder

B

MATLAB GUI FOR TIR-PH SETUP

Figure B.1: **Matlab GUI** – Screenshot of the GUI used to control the system

a *Laser on*: starts the trapping laser in preview mode. This is useful to position the laser on the green cross at the centre of the screen before the measurements.

b *Experiment Type*: selects the operational mode between Pull & Release mode and Sine wave mode.

c *Moving*: selects between the piezo stage or the piezo actuated mirror. The GUI updates the conversion factor for calculating the distance of which to move the trap.

d *Preview Window*: Live image from the 100x camera. When the preview is active, the 488nm laser for the fluorescence is set to ON while the trapping laser is set to OFF (unless otherwise selected through (a). The green cross indicates the initial trap position.

e *Capture*: saves a frame from the preview as a matlab file *date-time-capture.mat*.

f *Measurement Parameters*: select the parameters of the experiment

- Exposure: changes the exposure time of the camera, and the rate of the trap movement (rate = 1/(2x time of exposure))
- Distance: the distance in micron to move the trap
- Direction: the direction in which the stage/mirror is moving
- Freq: only available for Sine wave experiment, it defines the frequency of the sine wave
- Meas Time: in Pull & Release mode, it indicates how much time the trap employs to move the distance selected. Therefore, it modify the speed at which the trap is moving. In Sine wave mode, it indicates the total time of the measurement
- cycles: the number of times you want the trap to move the desired distance (new function - not used for this thesis)
- Pause time: how much time to wait in between cycles. During this time, the laser is shut off, and no frames are being collected (new function - not used for this thesis)

g *Meas. Info*: for the user to save notes and info about the measurement. These fields DO NOT affect the measurements themselves.

h *Preview*: starts or stops the Preview Window.

i Start: starts the measurement accordingly to the Measurement Parameters. During the measurement the trapping laser is set to ON automatically, without the need to select (a). During the measurement all the buttons are disabled. At the end of the measurements, two files are saved: *date-time-embryo.mat* and *date-time-embryo.mj*; the first one contains all the measurements parameters and measurements informations, while the second contains the video of the embryo being pulled.

j quit: closes the program and clears the memory.

C

BACKWARD-SCATTERING BACK FOCAL PLANE INTERFEROMETRY IN VIVO

I attempted to perform backward-scattering back focal plane interferometry with the TIR-Ph set-up, in order to calibrate the optical tweezers trapping organelles inside the chick embryos. Here I present these early attempts. Despite the fact that I did not complete these measurements, they can contribute to the success of future studies.

I modified the TIR-Ph system as per Figure C.2.

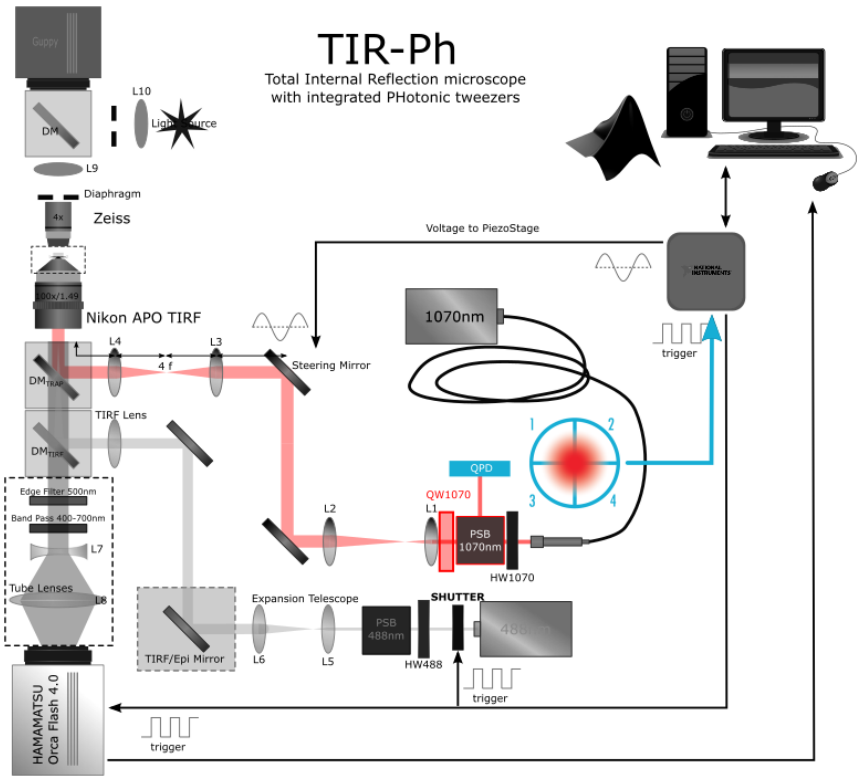

Figure C.1: **TIR-Ph set-up + QPD** – TIR-Ph set-up after the introduction of a QPD. We also introduced a quarter wavelength plates, as suggested in [82].

BEADS MEASUREMENTS

First I tried to measure power spectra on commercial silica beads. Unfortunately, I did not obtain good power spectra. Examples of 500nm beads, measured both in backward and in forward scattering are reported [1].

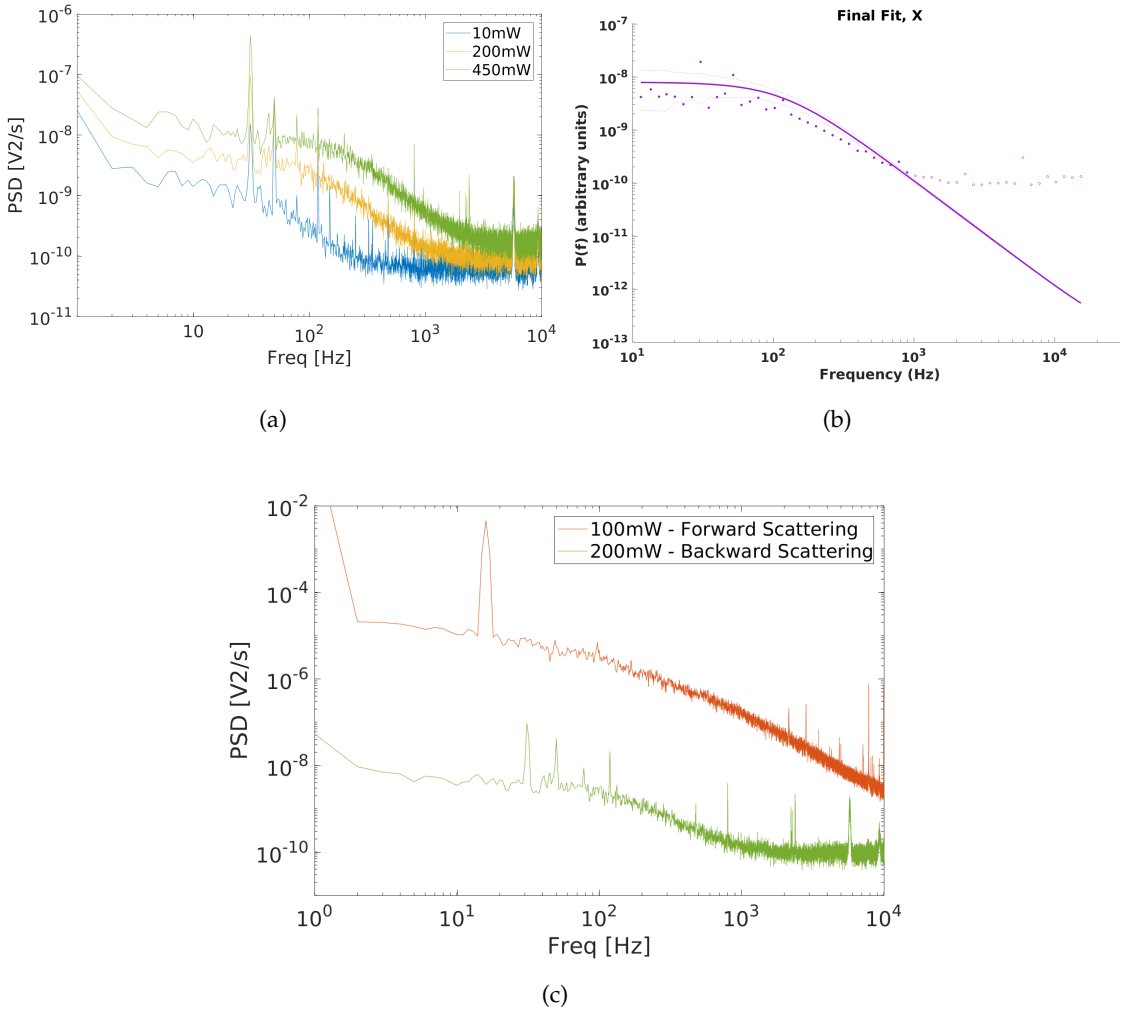

(a) (b)

(c)

Figure C.2: **Backward scattering - 500nm beads** – (a) Example of power spectra of 500nm silica beads collected in backward-scattering, at different trapping laser power. (b) The fit with the Matlab *Tweezercalib* toolbox failed, because the spectra do not have a Lorenztian shape. (c) Comparing the spectra bead measured in forward-scattering (a) with the ones measured in backward-scattering, it can be observes that the two spectra differ of several orders of magnitude. In fact, the signal collected by the QPD in backward-scattering was very small.

1 The forward-scattering measurements were performed by Dr. Davis in different optical tweezers set-up, but using a QPD of the same model

The results in Figure C.2 suggests that the QPD was not at the right conjugate plane. Additional efforts should be made in order to fix this problem. However, as mentioned in chapter 1, the spectra become more complicated in backward-scattering. This fact could have also impacted on the quality of the spectra.

ORGANELLES IN CELLS - POWER SPECTRA MEASUREMENTS

In order to interpret the spectra of organelles inside chick embryos cells, I collected power spectra of organelles inside Madin-Darby canine kidney (MDCK) cells [2]. In fact, the spectra of organelles in single cells could also be collected in forward-scattering for comparison [3]. Example of spectra are reported in Figure C.3.

The spectra of organelles measured in forward-scattering inside cells are similar to the spectra of organelles measured in backward-scattering, despite the difference observed for the case of 500nm beads. However spectra from different organelles are quite different from one another so it is difficult to drag conclusions without further studies (see Figure C.4).

ORGANELLES IN EMBRYO - POWER SPECTRA MEASUREMENTS

For the measurement of organelles inside chick embryos' cells, forward-scattering interferometry could not be performed, so backward-scattering was used instead. The shape of the spectrum makes it impossible to perform any calibration on the tweezers stiffness (see Figure C.5).

Finally, I would like to show the raw signal from the QPD when an organelles was moved against the junction (see Figure C.6). The signal intensity varied in a reproducible manner when moving in specific locations/directions in the sample. This suggests that, by improving this approach, it would be possible to correlate the signal from the QPD with the deflection measured by the junction.

2 The cells were kindly provided by Dr. Rabl

3 The forward-scattering measurements were performed by Dr. Davis in different optical tweezers set-up, but using a QPD of the same model

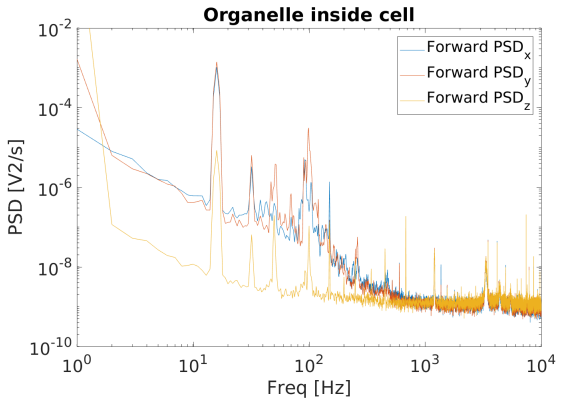

(a)

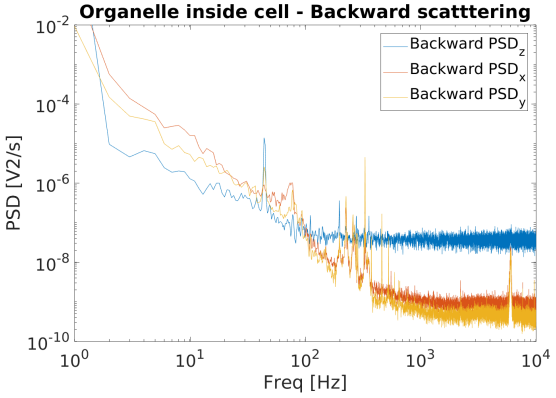

(b)

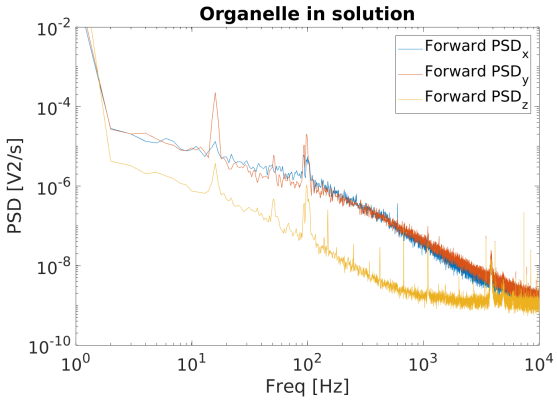

(c)

Figure C.3: **Organelles trapped in cells and in solution** – (a) Example of power spectrum of an organelle inside a cell, measured in forward-scattering interferometry. (b) Example of power spectrum of an organelle inside a cell, measured in backward-scattering interferometry. (c)Example of power spectrum of an organelle found floating in the medium outside the cell, measured in forward-scattering.

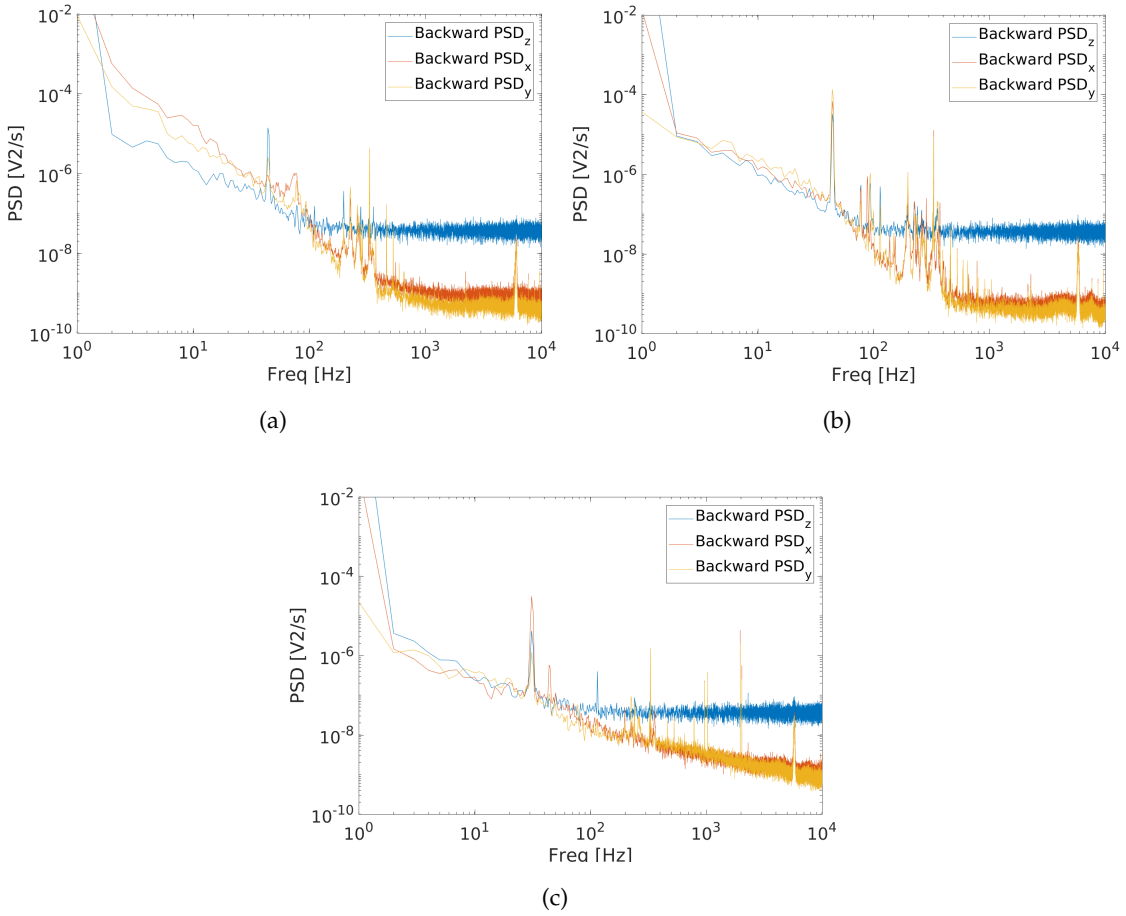

Figure C.4: **Organelles trapped in cells - backward-scattering** – (a-c) Examples of power spectra of organelles trapped inside a cell, measured in backward-scattering interferometry. I attempted the self-calibration technique with oscillation frequency 32Hz (first peak in the power spectra). It is interesting to notice that (b) has a higher peak than (a), suggesting that it is oscillating more with the movement of the stage. Therefore it is possible that the organelle in (b) is bound to some element of the cytoskeleton, and for this reason we cannot trap it as well as the organelle in (a). Finally, in (c) we can see a spectrum with a very different shape, quite similar to the spectra we measured for organelles in the chick embryos.

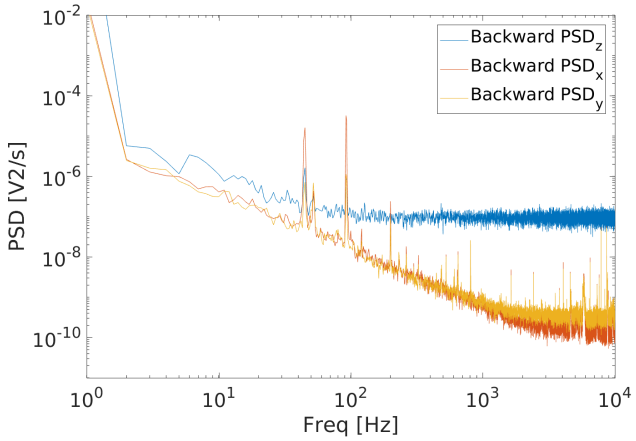

Figure C.5: **Organelles trapped in a chick embryo - backward-scattering** – Examples of power spectrum of an organelle trapped inside a chick embryo cell, measured in backward-scattering interferometry.

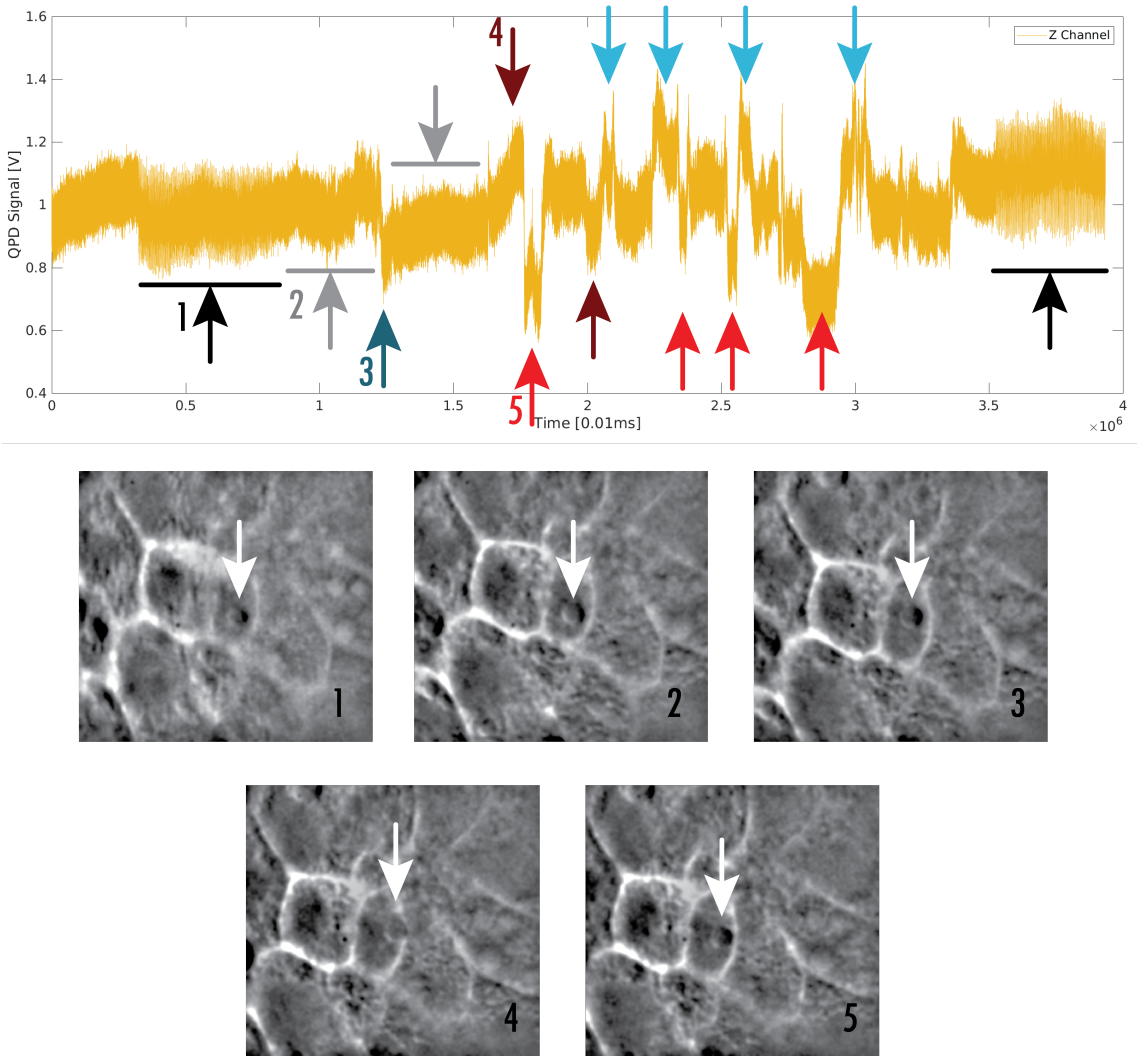

Figure C.6: **Organelles trapped in a chick embryo - QPD tracking** – Raw voltage signal from QPD for the z- axis (top). Black arrows indicate when I applied the 32Hz oscillation of the self-calibrating method for the stiffness measurement; gray arrows indicate examples of when I did not move the stage; dark green arrow indicates when I moved the stage down to centre the organelle respect to the junction; dark brown arrows indicate the organelle pushing against the junctions; red arrows indicate when I crossed the junction moving left to right; finally, blue arrows indicates when I crossed the junction moving right to left. At the bottom there are frames from the video of the tracking of the top graph: white arrows highlight the position of the organelle. The frames are numbered: each number refer to a specific moment in the QPD signal, as indicated in the top graph.

BIBLIOGRAPHY

[1] Arthur Ashkin, J. M. Dziedzic, J. E. Bjorkholm, and Steven Chu. Observation of a single-beam gradient force optical trap for dielectric particles. *Optics Letters*, 11(5):288, may 1986.

[2] Cecile O Mejean, Andrew W Schaefer, Eleanor a Millman, Paul Forscher, and Eric R Dufresne. Multiplexed force measurements on live cells with holographic optical tweezers. *Optics express*, 17(8):6209–6217, 2009.

[3] K. Volke-Sepulveda, V. Garcés-Chávez, S. Chávez-Cerda, J. Arlt, and K. Dholakia. Orbital angular momentum of a high-order Bessel light beam. *Journal of Optics B: Quantum and Semiclassical Optics*, 4(2), 2002.

[4] V. Garcés-Chávez, D. McGloin, M. J. Padgett, W. Dultz, H. Schmitzer, and K. Dholakia. Observation of the Transfer of the Local Angular Momentum Density of a Multiringed Light Beam to an Optically Trapped Particle. *Physical Review Letters*, 91(9), 2003.

[5] N. B. Simpson, K. Dholakia, L. Allen, and M. J. Padgett. Mechanical equivalence of spin and orbital angular momentum of light: an optical spanner. *Optics Letters*, 22(1):52, 1997.

[6] Karel Svoboda and Steven M. Block. Optical trapping of metallic Rayleigh particles. *Optics Letters*, 19(13):930, jul 1994.

[7] Pamela T. Korda, Gabriel C. Spalding, and David G. Grier. Evolution of a colloidal critical state in an optical pinning potential landscape. *Physical Review B - Condensed Matter and Materials Physics*, 66(2):245041–245047, 2002.

[8] M M Burns, J M Fournier, and J A Golovchenko. Optical matter: crystallization and binding in intense optical fields. *Science (New York, N.Y.)*, 249(4970):749–54, 1990.

[9] N. K. Metzger, R. F. Marchington, M. Mazilu, R. L. Smith, K. Dholakia, and E. M. Wright. Measurement of the restoring forces acting on two optically bound particles from normal mode correlations. *Physical Review Letters*, 98(6), 2007.

[10] Richard W Bowman and Miles J Padgett. Optical trapping and binding. *Reports on progress in physics. Physical Society (Great Britain)*, 76(2):026401, feb 2013.

[11] T. L. Gustavson, A. P. Chikkatur, A. E. Leanhardt, A. Gorlitz, S. Gupta, D. E. Pritchard, and W. Ketterle. Transport of Bose-Einstein Condensates with Optical Tweezers. aug 2001.

[12] Richard Van Noorden. Interdisciplinary research by the numbers. *Nature*, 525(7569):306–307, 2015.

[13] Jaime Castillo, Maria Dimaki, and Winnie Edith Svendsen. Manipulation of biological samples using micro and nano techniques. *Integr. Biol.*, 1(1):30–42, 2009.

[14] Hu Zhang and Kuo-kang K.-K. Liu. Optical tweezers for single cells. *Journal of the Royal Society, Interface / the Royal Society*, 5(24):671–690, jul 2008.

[15] Thomas T. Perkins. Optical traps for single molecule biophysics: a primer. *Laser & Photonics Review*, 3(1-2):203–220, feb 2009.

[16] Keir C. Neuman and Attila Nagy. Single-molecule force spectroscopy: optical tweezers, magnetic tweezers and atomic force microscopy. *Nature Methods*, 5(6):491–505, 2008.

[17] K. Sugimura, P.-F. Lenne, and F. Graner. Measuring forces and stresses in situ in living tissues. *Development*, 143(2):186–196, jan 2016.

[18] Alba Diz-Muñoz, Daniel a. Fletcher, and Orion D. Weiner. Use the force: Membrane tension as an organizer of cell shape and motility. *Trends in Cell Biology*, 23(2):47–53, 2013.

[19] Feng Guo, Yuliang Xie, Sixing Li, James Lata, Liqiang Ren, Zhangming Mao, Baiyang Ren, Mengxi Wu, Adem Ozcelik, and Tony Jun Huang. Reusable acoustic tweezers for disposable devices. *Lab Chip*, 15(24):4517–4523, 2015.

[20] Jungwoo Lee, Shia Yen Teh, Abraham Lee, Hyung Ham Kim, Changyang Lee, and K. Kirk Shung. Single beam acoustic trapping. *Applied Physics Letters*, 95(7), 2009.

[21] Yongqiang Qiu, Han Wang, Christine E M Demore, David a. Hughes, Peter Glynne-Jones, Sylvia Gebhardt, Aleksandrs Bolhovitins, Romans Poltarjonoks, Cornelis J. Weijer, Andreas Schönecker, Martyn Hill, and Sandy Cochran. *Acoustic devices for particle and cell manipulation and sensing.*, volume 14. mdpi, jan 2014.

[22] Junru Wu. Acoustical tweezers. *The Journal of the Acoustical Society of America*, 89(5):2140–2143, 1991.

[23] Philip J. Kitson, Mali H. Rosnes, Victor Sans, Vincenza Dragone, and Leroy Cronin. Configurable 3D-Printed millifluidic and microfluidic 'lab on a chip' reactionware devices. *Lab on a Chip*, 12(18):3267, 2012.

[24] Keir C. Neuman and Steven M. Block. Optical trapping. *The Review of scientific instruments*, 75(9):2787–809, sep 2004.

[25] Anita Jannasch, Ahmet Faik Demirörs, Peter D. J. van Oostrum, Alfons van Blaaderen, and Erik Schäffer. Nanonewton optical force trap employing anti-reflection coated, high-refractive-index titania microspheres. *Nature Photonics*, 6(7):469–473, jun 2012.

[26] Arthur Ashkin. Acceleration and trapping of particles by radiation pressure. *Physical review letters*, 1970.

[27] Arthur Ashkin and J. M. Dziedzic. Optical Levitation by Radiation Pressure. *Applied Physics Letters*, 19(8):283–285, oct 1971.

[28] Arthur Ashkin, J. M. Dziedzic, and T Yamane. Optical trapping and manipulation of single cells using infrared laser beams. *Nature*, 330(6150):769–71, jan 1987.

[29] Arthur Ashkin, K Schütze, J. M. Dziedzic, U Euteneuer, and M Schliwa. Force generation of organelle transport measured in vivo by an infrared laser trap., 1990.

[30] Arthur Ashkin. The study of cells by optical trapping and manipulation of living cells using infrared laser beams, 1991.

[31] Miriam W Allersma, Frederick Gittes, J Michael, Russell J Stewart, and Christoph F. Schmidt. Two-Dimensional Tracking of ncd Motility by Back Focal Plane Interferometry. *Biophysical journal*, 74(February):1074–1085, 1998.

[32] Pradeep Barak, Ashim Rai, Priyanka Rai, and Roop Mallik. Quantitative optical trapping on single organelles in cell extract. *Nature methods*, 10(1):68–70, 2013.

[33] Benjamin H. Blehm and Paul R. Selvin. Single-molecule fluorescence and in vivo optical traps: How multiple dyneins and kinesins interact. *Chemical Reviews*, 114(6):3335–3352, 2014.

[34] Jeffrey T. Finer, Robert M. Simmons, and James A. Spudich. Single myosin molecule mechanics: piconewton forces and nanometre steps. *Nature*, 368(6467):113–119, 1994.

[35] Karel Svoboda, Christoph F. Schmidt, Bruce J. Schnapp, and Steven M. Block. Direct observation of kinesin stepping by optical trapping interferometry. *Nature*, 365(6448):721–727, 1993.

[36] J. E. Molloy, J. E. Burns, J. Kendrick-Jones, R. T. Tregear, and D. C S White. Movement and force produced by a single myosin head. *Nature*, 378(6553):209–212, nov 1995.

[37] Arnau Farré, Astrid van der Horst, Gerhard a. Blab, Benjamin P B Downing, and Nancy R. Forde. Stretching single DNA molecules to demonstrate high-force capabilities of holographic optical tweezers. *Journal of Biophotonics*, 3(4):224–233, 2010.

[38] Furqan M Fazal and Steven M. Block. Optical tweezers study life under tension. *Nature Photonics*, 5(6):318–321, 2011.

[39] Daniel P. Cherney, Travis E. Bridges, and Joel M. Harris. Optical trapping of unilamellar phospholipid vesicles: Investigation of the effect of optical forces on the lipid membrane shape by confocal-Raman microscopy. *Analytical Chemistry*, 76(17):4920–4928, 2004.

[40] Pei Yu Chiou, Aaron T. Ohta, and Ming C. Wu. Massively parallel manipulation of single cells and microparticles using optical images. *Nature*, 436(7049):370–372, 2005.

[41] Nicholas Hyun, Charlie Chandsawangbhuwana, Qingyuan Zhu, Linda Z. Shi, Collin Yang-Wong, and Michael W Berns. Effects of viscosity on sperm motility studied with optical tweezers. *Journal of Biomedical Optics*, 17(2):025005, 2012.

[42] Ashis Banerjee, Sagar Chowdhury, and Satyandra K. Gupta. Optical Tweezers: Autonomous Robots for the Manipulation of Biological Cells. *IEEE Robotics & Automation Magazine*, 21(3):81–88, sep 2014.

[43] Sagar Chowdhury, Petr Svec, Chenlu Wang, Wolfgang Losert, and Satyandra K. Gupta. Gripper synthesis for indirect manipulation of cells using holographic optical tweezers. *Proceedings - IEEE International Conference on Robotics and Automation*, pages 2749–2754, 2012.

[44] Sagar Chowdhury, Atul Thakur, Chenlu Wang, Petr Svec, Wolfgang Losert, and Satyandra K. Gupta. Automated indirect manipulation of irregular shaped cells with Optical Tweezers for studying collective cell migration. *Proceedings - IEEE International Conference on Robotics and Automation*, pages 2789–2794, 2013.

[45] Xue Gou, Xiaolin Wang, Hao Yang, Xiao Yan, Yong Wang, Tarek M Fahmy, and Dong Sun. Dynamic control of cell migration using optical tweezers and microfluidic channel. *2012 12th IEEE Conference on Nanotechnology (IEEE-NANO)*, pages 1 – 5, 2012.

[46] Jaime B. Hutchison, Christopher a. Rodesney, Karishma S. Kaushik, Henry H. Le, Daniel a. Hurwitz, Yasuhiko Irie, and Vernita D. Gordon. Single-cell control of initial spatial structure in biofilm development using laser trapping. *Langmuir*, 30(15):4522–4530, 2014.

[47] Zhiwen Kang, Jiajie Chen, Shu-Yuen Wu, Kun Chen, Siu-Kai Kong, Ken-Tye Yong, and Ho-Pui Ho. Trapping and assembling of particles and live cells on large-scale random gold nano-island substrates. *Scientific Reports*, 5:9978, 2015.

[48] Laurent Blanchoin, Rajaa Boujemaa-Paterski, Cécile Sykes, and Julie Plastino. Actin dynamics, architecture, and mechanics in cell motility. *Physiological reviews*, 94(1):235–63, 2014.

[49] Rok Podlipec and Janez Štrancar. Cell-Scaffold Adhesion Dynamics Measured in First Seconds Predicts Cell Growth on Days Scale - Optical Tweezers Study. *ACS Applied Materials & Interfaces*, page 150312113303001, 2015.

[50] Ilaria Prada, Ladan Amin, Roberto Furlan, Giuseppe Legname, Claudia Verderio, and Dan Cojoc. A new approach to follow a single extracellular vesicle-cell interaction using optical tweezers. *BioTechniques*, 60(1):35–41, 2016.

[51] Melanie Schwingel and Martin Bastmeyer. Force Mapping during the Formation and Maturation of Cell Adhesion Sites with Multiple Optical Tweezers. *PLoS ONE*, 8(1), 2013.

[52] J Sleep, D Wilson, Robert M. Simmons, and W Gratzer. Elasticity of the red cell membrane and its relation to hemolytic disorders: an optical tweezers study. *Biophysical journal*, 77(6):3085–3095, 1999.

[53] Eric Stellamanns, Sravanti Uppaluri, Axel Hochstetter, Niko Heddergott, Markus Engstler, and Thomas Pfohl. Optical trapping reveals propulsion forces, power generation and motility efficiency of the unicellular parasites Trypanosoma brucei brucei. *Scientific Reports*, 4:6515, oct 2014.

[54] Gregor Thalhammer, R Steiger, S Bernet, and M Ritsch-Marte. Optical macro-tweezers: trapping of highly motile micro-organisms. *Journal of Optics*, 13(4):044024, apr 2011.

[55] Tao Wu, Timo A. Nieminen, Samarendra Mohanty, Jill Miotke, Ronald L. Meyer, Halina Rubinsztein-Dunlop, and Michael W Berns. A photon-driven micromotor can direct nerve fibre growth. *Nature Photonics*, 6(1):62–67, dec 2011.

[56] Hao Yang, Xue Gou, Yong Wang, and Dong Sun. Study on Cell Motility Mechanism Using a Cell Manipulation System with Optical Tweezers. *IEEE*, pages 91–94, 2013.

[57] Jessica Ferraro-Gideon, Rozhan Sheykhani, Qingyuan Zhu, Michelle L Duquette, Michael W Berns, and Arthur Forer. Measurements of forces produced by the mitotic spindle using optical tweezers. *Molecular biology of the cell*, 24(9):1375–86, 2013.

[58] E. Eriksson, J. Scrimgeour, A. Granéli, K. Ramser, R. Wellander, J. Enger, D. Hanstorp, and M. Goksör. Optical manipulation and microfluidics for studies of single cell dynamics. *Journal of Optics A: Pure and Applied Optics*, 9(8):S113–S121, aug 2007.

[59] Leonardo Sacconi, Iva Marija Tolić-Nørrelykke, Chiara Stringari, Renzo Antolini, and Francesco S. Pavone. Optical micromanipulations inside yeast cells. *Applied optics*, 44(11):2001–7, 2005.

[60] Itia A. Favre-Bulle, Alexander B. Stilgoe, Halina Rubinsztein-Dunlop, and Ethan K. Scott. Optical trapping of otoliths drives vestibular behaviours in larval zebrafish. *Nature Communications*, 8(1), 2017.

[61] Kapil Bambardekar, Raphaël Clément, Olivier Blanc, Claire Chardès, and Pierre-François Lenne. Direct laser manipulation reveals the mechanics of cell contacts in vivo. *Proceedings of the National Academy of Sciences*, 112(5):1416–1421, 2015.

[62] Arthur Ashkin. Forces of a single-beam gradient laser trap on a dielectric sphere in the ray optics regime. *Biophysical Journal*, 61(2):569–582, 1992.

[63] Arthur Ashkin. History of optical trapping and manipulation of small-neutral particle, atoms, and molecules. *IEEE Journal on Selected Topics in Quantum Electronics*, 6(6):841–856, 2000.

[64] Philip Jones, Onofrio Marago, and Giovanni Volpe. *Optical Tweezers*. Cambridge University Press, Cambridge, 2015.

[65] Gustav Mie. Contributions to the optics of turbid media, particularly of colloidal metal solutions, 1908.

[66] Michael I. Mishchenko, Larry D. Travis, and Andrew A. Lacis. *Scattering, Absoption, and Emission of Light by Small Particles*. NASA, 2005.

[67] Timo A. Nieminen, Vincent L.Y. Loke, Alexander B. Stilgoe, G Knoner, Norman R. Heckenberg, Halina Rubinsztein-dunlop, A M Bra, Gregor Knöner, and Agata M Brańczyk. Optical tweezers computational toolbox. *Journal of Optics A: Pure and Applied Optics*, 9(8):S196–S203, aug 2007.

[68] E. M. Purcell. Life at low Reynolds number. *American Journal of Physics*, 45(1):3–11, 1977.

[69] Bernard Knaepen and René Moreau. Magnetohydrodynamic Turbulence at Low Magnetic Reynolds Number. *Annual Review of Fluid Mechanics*, 40(1):25–45, jan 2008.

[70] Woei Ming Lee, Peter J Reece, Robert F Marchington, Nikolaus K Metzger, and Kishan Dholakia. Construction and calibration of an optical trap on a fluorescence optical microscope. *Nature protocols*, 2(12):3226–38, jan 2007.

[71] Joshua W Shaevitz. *A Practical Guide to Optical Trapping*. 2006.

[72] Joseph W. Goodman. Introduction to Fourier Optics, Third Edition, 2004.

[73] Mohammed Mahamdeh, Citlali Pérez Campos, and Erik Schäffer. Under-filling trapping objectives optimizes the use of the available laser power in optical tweezers. *Optics express*, 19(12):11759–11768, 2011.

[74] Volker Bormuth, Anita Jannasch, Marcel Ander, Carlos M van Kats, Alfons van Blaaderen, Jonathon Howard, Erik Schäffer, Carlos M Van Kats, and Alfons Van Blaaderen. Optical trapping of coated microspheres. *Optic Express*, 16(18):423–427, 2008.

[75] Norman R Heckenberg Ying Hu Timo A. Nieminen and Halina Rubinsztein-Dunlop. Antireflection coating for improved optical trapping. *J Appl. Phys*, 103, 2008.

[76] Steven B. Smith, Yujia Cui, and Carlos Bustamante. Optical-trap force transducer that operates by direct measurement of light momentum. *Methods in Enzymology*, 361(1994):134–162, 2003.

[77] Winfried Denk and Watt W Webb. Optical measurement of picometer displacements of transparent microscopic objects. *Applied Optics*, 29(16):2382, jun 1990.

[78] L P Ghislain and Watt W Webb. Scanning-force microscope based on an optical trap. *Optics letters*, 18(19):1678–1680, 1993.

[79] Frederick Gittes and Christoph F. Schmidt. Interference model for back-focal-plane displacement detection in optical tweezers. *Optics Letters*, 23(1):7, jan 1998.

[80] Giovanni Volpe, Gregory Kozyreff, and Dmitri Petrov. Backscattering position detection for photonic force microscopy. *Journal of Applied Physics*, 102(8):084701, oct 2007.

[81] Yi-Jr Su and Long Hsu. Comparison of backward-scattered detection and forward-scattered detection for measuring optical force in optical tweezers. *Proceedings of Spie*, 7762:77623D–1–7, 2010.

[82] J. H. G. Huisstede, K. O. van der Werf, M. L. Bennink, and V. Subramaniam. Force detection in optical tweezers using backscattered light. *Optics express*, 13(4):1113–1123, feb 2005.

[83] Simon F. Tolić-Nørrelykke, Erik Schäffer, Jonathon Howard, Francesco S. Pavone, Frank Jülicher, and Henrik Flyvbjerg. Calibration of optical tweezers with positional detection in the back focal plane. *Review of Scientific Instruments*, 77(10):103101, mar 2006.

[84] S Nader S Reihani and Lene B Oddershede. Optimizing immersion media refractive index improves optical trapping by compensating spherical aberrations. *Opt. Lett.*, 32(14):1998–2000, jul 2007.

[85] T Ota, T Sugiura, S Kawata, Martin J Booth, M A A Neil, R Juskaitis, and T Wilson. Enhancement of laser trapping force by spherical aberration correction using a deformable mirror. *Japanese Journal of Applied Physics Part 2-Letters*, 42(6B):L701–L703, 2003.

[86] N. B. Simpson, David McGloin, Kishan Dholakia, L. Allen, and Miles J Padgett. Optical tweezers with increased axial trapping efficiency. *Journal of Modern Optics*, 45(9):1943–1949, sep 1998.

[87] Michael A Taylor, Muhammad Waleed, Alexander B. Stilgoe, Halina Rubinsztein-dunlop, and Warwick P Bowen. Enhanced optical trapping via structured scattering. *Nat. Photon.*, 9(October):669–674, 2015.

[88] Yuichi Kozawa and Shunichi Sato. Optical trapping of micrometer-sized dielectric particles by cylindrical vector beams. *Optics Express*, 18(10):10828, may 2010.

[89] Ahmet Faik Demirörs, Anita Jannasch, Peter D. J. Van Oostrum, Erik Schäffer, Arnout Imhof, and Alfons Van Blaaderen. Seeded growth of titania colloids with refractive index tunability and fluorophore-free luminescence. *Langmuir*, 27(703821):1626–1634, 2011.

[90] Valentina Ferro, A. Sonnberger, Mohammad Kazem Abdosamadi, C. McDonald, Erik Schäffer, and David McGloin. Improved antireflection coated microspheres for biological applications of optical tweezers. In *Proceedings of SPIE - The International Society for Optical Engineering*, volume 9922, 2016.

[91] Xuchuan Jiang, Thurston Herricks, and Younan Xia. Monodispersed spherical colloids of titania: Synthesis, characterization, and crystallization. *Advanced Materials*, 15(14):1205–1209, 2003.

[92] Anita Jannasch, Mohammad Kazem Abdosamadi, Avin Ramaiya, Suman De, Valentina Ferro, Aaron Sonnberger, and Erik Schäffer. Custom-Made Microspheres for Optical Tweezers. In Arne Gennerich, editor, *Methods in Molecular Biology*, volume 1486, pages 137–155. Springer, 2017.

[93] S. Eiden-Assmann, J. Widoniak, and G. Maret. Synthesis and Characterization of Hollow and Non-Hollow Monodisperse Colloidal TiO 2 Particles. *Journal of Dispersion Science and Technology*, 25(10):535–545, 2005.

[94] A. Sonnberger. *Silica Coating of Anti-Reflective Titania Microspheres for Optical Tweezers*. PhD thesis, University of Tuebingen, 2014.

[95] Werner Stöber, Arthur Fink, and Ernst Bohn. Controlled growth of monodisperse silica spheres in the micron size range. *Journal of Colloid and Interface Science*, 26(1):62–69, 1968.

[96] Muhamad Zamri Yahaya, Mohd Zulkifly Abdullah, and Ahmad Azmin Mohamad. Centrifuge and storage precipitation of TiO2 nanoparticles by the sol-gel method. *Journal of Alloys and Compounds*, 651(July 2016):557–564, 2015.

[97] Hans Arora, Caroline Doty, Ye Yuan, John Boyle, Katarina Petras, Bryan Rabatic, Tatjana Paunesku, and Gayle Woloschak. Titanium Dioxide Nanocomposites. In *Nanotechnologies for the Life Sciences*, volume 8, pages 1–52. Wiley-VCH Verlag GmbH & Co. KGaA, Weinheim, Germany, feb 2012.

[98] Dmitry V. Bavykin, Jens M. Friedrich, and Frank C. Walsh. Protonated titanates and TiO2 nanostructured materials: Synthesis, properties, and applications. *Advanced Materials*, 18:2807–2824, 2006.

[99] O. Carp, C. L. Huisman, and A. Reller. Photoinduced reactivity of titanium dioxide. *Progress in Solid State Chemistry*, 32:33–177, 2004.

[100] Michael Dahl, Yiding Liu, and Yadong Yin. Composite Titanium Dioxide Nanomaterials. *Chemical reviews*, 2014.

[101] Cheng Wang, Zhao-Xiang Deng, Guohui Zhang, Shoushan Fan, and Yadong Li. Synthesis of nanocrystalline TiO2 in alcohols. *Powder Technology*, 125:39–44, 2002.

[102] Ulrike Diebold. The surface science of titanium dioxide. *Surface Science Reports*, 48(x):53–229, 2003.

[103] Akira Fujishima, Xintong Zhang, and Donald a. Tryk. TiO2 photocatalysis and related surface phenomena. *Surface Science Reports*, 63:515–582, 2008.

[104] K. Madhusudan Reddy, C.V. Gopal Reddy, and S.V. Manorama. Preparation, Characterization, and Spectral Studies on Nanocrystalline Anatase TiO2. *Journal of Solid State Chemistry*, 158:180–186, 2001.

[105] Naofumi Uekawa, Jyunichi Kajiwara, Kazuyuki Kakegawa, and Yoshinori Sasaki. Low temperature synthesis and characterization of porous anatase TiO2 nanoparticles. *Journal of colloid and interface science*, 250:285–290, 2002.

[106] Yadong Li, T. J. White, and S. H. Lim. Low-temperature synthesis and microstructural control of titania nano-particles. *Journal of Solid State Chemistry*, 177:1372–1381, 2004.

[107] Amy L Linsebigler, Amy L Linsebigler, John T Yates Jr, Guangquan Lu, Guangquan Lu, and John T Yates. Photocatalysis on TiO2 Surfaces: Principles, Mechanisms, and Selected Results. *Chemical Reviews*, 95:735–758, 1995.

[108] Tadao Sugimoto, Xingping Zhou, and Atsushi Muramatsu. Synthesis of uniform anatase TiO2 nanoparticles by gel-sol method: 3. Formation process and size control. *Journal of Colloid and Interface Science*, 259:43–52, 2003.

[109] Kota Shiba and Makoto Ogawa. Microfluidic syntheses of well-defined sub-micron nanoporous titania spherical particles. *Chemical Communications*, 44(44):6851, nov 2009.

[110] Kota Shiba, Ken Onaka, and Makoto Ogawa. Preparation of mono-dispersed titanium oxide-octadecylamine hybrid spherical particles in the submicron size range. *RSC Advances*, 2(4):1343, 2012.

[111] Mou Pal, J. García Serrano, P. Santiago, and U. Pal. Size-controlled synthesis of spherical TiO2 nanoparticles: Morphology, crystallization, and phase transition. *Journal of Physical Chemistry C*, 111:96–102, 2007.

[112] Hui Zhang, Deqian Li, Gaosong Shao, and Zhongyong Yuan. A simple method to prepare titania nanomaterials of core-shell structure, hollow nanospheres and mesoporous nanoparticles. *Science in China, Series B: Chemistry*, 52(20673060):1498–1503, 2009.

[113] Kota Shiba, Soh Sato, and Makoto Ogawa. Preparation of well-defined titania-silica spherical particles. *Journal of Materials Chemistry*, 22(19):9963, 2012.

[114] Kota Shiba, Toshiaki Takei, and Makoto Ogawa. Mesoporous silica coated silica-titania spherical particles: from impregnation to core-shell formation. *Dalton Trans.*, 45(46):18742–18749, 2016.

[115] Iva Marija Tolić-Nørrelykke, Kirstine Berg-Sørensen, and Henrik Flyvbjerg. MatLab program for precision calibration of optical tweezers. *Computer Physics Communications*, 159(3):225–240, 2004.

[116] Poul Martin Hansen, Iva Marija Tolić-Nørrelykke, Henrik Flyvbjerg, and Kirstine Berg-Sørensen. tweezercalib 2.1: Faster version of MatLab package for precise calibration of optical tweezers. *Computer Physics Communications*, 175(8):572–573, oct 2006.

[117] Revathi Ananthakrishnan and Allen Ehrlicher. The Forces Behind Cell Movement. *International Journal of Biochemistry and Cell Biology*, 3(5):303–317, 2007.

[118] Eva Vergucht, Toon Brans, Filip Beunis, Jan Garrevoet, Maarten De Rijcke, Stephen Bauters, David Deruytter, Michiel Vandegehuchte, Ine Van Nieuwenhove, Colin Janssen, Manfred Burghammer, and Laszlo Vincze. In vivo X-ray elemental imaging of single cell model organisms manipulated by laser-based optical tweezers. *Scientific Reports*, 5:9049, 2015.

[119] C Xie, J Mace, M A Dinno, Y Q Li, W Tang, R J Newton, and P J Gemperline. Identification of single bacterial cells in aqueous solution using confocal laser tweezers Raman spectroscopy. *Analytical Chemistry*, 77(14):4390–4397, 2005.

[120] James W. Chan, Douglas S. Taylor, Theodore Zwerdling, Stephen M. Lane, Ko Ihara, and Thomas Huser. Micro-raman spectroscopy detects individual neoplastic and normal hematopoietic cells. *Biophysical Journal*, 90(2):648–656, 2006.

[121] Feng Zheng, Yejun Qin, and Kun Chen. Sensitivity map of laser tweezers Raman spectroscopy for single-cell analysis of colorectal cancer. *Journal of Biomedical Optics*, 12(3):034002, 2007.

[122] E Townes-Anderson, R S St Jules, D M Sherry, J Lichtenberger, and M Hassanain. Micromanipulation of retinal neurons by optical tweezers. *Mol Vis*, 4:12, 1998.

[123] Pamela Jordan, Jonathan Leach, Miles Padgett, Paul Blackburn, Neil Isaacs, Mattias Goksör, Dag Hanstorp, Amanda Wright, John Girkin, and Jonathan Cooper. Creating permanent 3D arrangements of isolated cells using holographic optical tweezers. *Lab on a Chip*, 5(11):1224, 2005.

[124] G. M. Akselrod, W. Timp, U. Mirsaidov, Q. Zhao, C. Li, R. Timp, K. Timp, P. Matsudaira, and Greg L. Timp. Laser-guided assembly of heterotypic three-dimensional living cell microarrays. *Biophysical Journal*, 91(9):3465–3473, 2006.

[125] M. Pradhan, S. Pathak, D. Mathur, and U. Ladiwala. Optically trapping tumor cells to assess differentiation and prognosis of cancers. *Biomedical Optics Express*, 7(3):943, mar 2016.

[126] G Lenormand, S Hénon, A Richert, J Siméon, and F Gallet. Direct measurement of the area expansion and shear moduli of the human red blood cell membrane skeleton. *Biophysical journal*, 81(1):43–56, jul 2001.

[127] C.T. Lim, M. Dao, S. Suresh, C.H. Sow, and K.T. Chew. Large deformation of living cells using laser traps. *Acta Materialia*, 52(7):1837–1845, apr 2004.

[128] Wei Huang, Bahman Anvari, Jorge H Torres, Richard G LeBaron, and Kyriacos A Athanasiou. Temporal effects of cell adhesion on mechanical characteristics of the single chondrocyte. *Journal of Orthopaedic Research*, 21(1):88–95, jan 2003.

[129] Muhammad S. Yousafzai, Fatou Ndoye, Giovanna Coceano, Joseph Niemela, Serena Bonin, Giacinto Scoles, and Dan Cojoc. Substrate-dependent cell elasticity measured by optical tweezers indentation. *Optics and Lasers in Engineering*, pages 1–7, 2015.

[130] Iva Marija Tolić-Nørrelykke, Leonardo Sacconi, Chiara Stringari, Isabel Raabe, and Francesco S. Pavone. Nuclear and division-plane positioning revealed by optical micromanipulation. *Current Biology*, 15(13):1212–1216, 2005.

[131] Mickael Castelain, Paul G. Rouxhet, Frederic Pignon, Albert Magnin, and Jean-Michel Piau. Single-cell adhesion probed in-situ using optical tweezers: A case study with Saccharomyces cerevisiae. *Journal of Applied Physics*, 111(11):114701, 2012.

[132] Steven D Marlin and Timothy A Springer. Purified intercellular adhesion molecule-1 (ICAM-1) is a ligand for lymphocyte function-associated antigen 1 (LFA-1). *Cell*, 51(5):813–9, 1987.

[133] Michael L. Dustin and Timothy A Springer. Mechanisms for Lymphocyte Adhesion to Cultured Endothelial Cells. *Cell*, 107(July):321–331, 1988.

[134] Craig McDonald, S. C. Fagerholm, and David McGloin. E ect of kindlin-3 binding site mutation on LFA-1- ICAM-1 bond strength.

[135] Valentina Ferro and David McGloin. Demonstration of high strength tweezers based on reflection coated beads. prototype, University of Dundee, 2016.

[136] G Rainaldi, a Calcabrini, and M T Santini. Positively charged polymer polylysine-induced cell adhesion molecule redistribution in K562 cells. *Journal of materials science. Materials in medicine*, 9(12):755–60, 1998.

[137] Ewa P. Wojcikiewicz, Midhat H. Abdulreda, Xiaohui Zhang, and Vincent T. Moy. Force Spectroscopy of LFA-1 and Its Ligands, ICAM-1 and ICAM-2. *Biomacromolecules*, 7(11):3188–3195, nov 2006.

[138] Hwee San Lek, Vicky L. Morrison, Michael Conneely, Paul a. Campbell, David McGloin, Stefanie Kliche, Colin Watts, Alan Prescott, and Susanna C. Fagerholm.

The Spontaneously Adhesive Leukocyte Function-associated Antigen-1 (LFA-1) Integrin in Effector T Cells Mediates Rapid Actin- and Calmodulin-dependent Adhesion Strengthening to Ligand under Shear Flow. *Journal of Biological Chemistry*, 288(21):14698–14708, may 2013.

[139] a J Durston. Dictyostelium: The Mathematician's Organism. *Current genomics*, 14(6):355–60, sep 2013.

[140] F Siegert and Cornelis J. Weijer. Three-dimensional scroll waves organize Dictyostelium slugs. *Proceedings of the National Academy of Sciences of the United States of America*, 89(14):6433–6437, 1992.

[141] Cornelis J. Weijer. Morphogenetic cell movement in Dictyostelium. *Seminars in Cell and Developmental Biology*, 10(6):609–619, 1999.

[142] Cornelis J. Weijer. Dictyostelium morphogenesis. *Current Opinion in Genetics and Development*, 14(4):392–398, 2004.

[143] Cornelis J Weijer and Jeffrey G Williams. Dictyostelium : Cell Sorting and Patterning. In *Encyclopedia of Life Sciences*, pages 1–12. John Wiley & Sons, Ltd, Chichester, UK, dec 2009.

[144] Paul D. Langridge and Robert R. Kay. Blebbing of Dictyostelium cells in response to chemoattractant. *Experimental Cell Research*, 312(11):2009–2017, 2006.

[145] Kunito Yoshida. Dissection of amoeboid movement into two mechanically distinct modes. *Journal of Cell Science*, 119(18):3833–3844, aug 2006.

[146] Oliver T. Fackler and Robert Grosse. Cell motility through plasma membrane blebbing. *The Journal of Cell Biology*, 181(6):879–884, jun 2008.

[147] Evgeny Zatulovskiy, Richard Tyson, Till Bretschneider, and Robert R. Kay. Bleb-driven chemotaxis of Dictyostelium cells. *Journal of Cell Biology*, 204(6):1027–1044, 2014.

[148] Guillaume T. Charras, Chi K. Hu, Margaret Coughlin, and Timothy J. Mitchison. Reassembly of contractile actin cortex in cell blebs. *Journal of Cell Biology*, 175(3):477–490, 2006.

[149] David a. Hughes, Cornelis J. Weijer, Yongqiang Qiu, Christine E M Demore, and Sandy Cochran. Investigating the motility of Dictyostelium discodeum using high frequency ultrasound as a method of manipulation. *IEEE International Ultrasonics Symposium, IUS*, pages 2002–2005, 2012.

[150] Guillaume T. Charras and Ewa Paluch. Blebs lead the way: how to migrate without lamellipodia. *Nature Reviews Molecular Cell Biology*, 9(9):730–736, sep 2008.

[151] Stephen E. Malawista, Anne Boisfleury De Chevance, and Laurence A. Boxer. Random locomotion and chemotaxis of human blood polymorphonuclear leukocytes from a patient with Leukocyte Adhesion Deficiency-1: Normal displacement in close quarters via chimneying. *Cell Motility and the Cytoskeleton*, 46(3):183–189, 2000.

[152] Yuri Belotti. *Microfluidic methods for investigating cell migration and cell mechanics*. PhD thesis, University of Dundee, 2016.

[153] Aristotele and D'Arcy Wentworth (translator) Thompson. The Internet Classics Archive | The History of Animals by Aristotle.

[154] Viktor Hamburger and Howard Hamilton. Series of normal stages in the development of the chick embryo. *Developmental Dynamics*, 88(1):231–272, 1993.

[155] Ruth Bellairs. The primitive streak. *Anatomy and Embryology*, 174(1):1–14, apr 1986.

[156] M. G. Davey and C. Tickle. The chicken as a model for embryonic development. *Cytogenetic and Genome Research*, 117(1-4):231–239, 2007.

[157] Rita R. Ferreira and Julien Vermot. The balancing roles of mechanical forces during left-right patterning and asymmetric morphogenesis. *Mechanisms of Development*, 144:71–80, 2017.

[158] R F Bachvarova, I Skromne, and C D Stern. Induction of primitive streak and Hensen's node by the posterior marginal zone in the early chick embryo. *Development (Cambridge, England)*, 125(17):3521–3534, 1998.

[159] Emil Rozbicki, Manli Chuai, Antti I. Karjalainen, Feifei Song, Helen M. Sang, René Martin, Hans-Joachim Joachim Knölker, Michael P. Macdonald, and Cornelis J.

Weijer. Myosin-II-mediated cell shape changes and cell intercalation contribute to primitive streak formation. *Nature Cell Biology*, 17(4):397–408, 2015.

[160] Cheng Cui, Xuesong Yang, Manli Chuai, James A. Glazier, and Cornelis J. Weijer. Analysis of tissue flow patterns during primitive streak formation in the chick embryo. *Developmental Biology*, 284(1):37–47, aug 2005.

[161] Brian Ciruna and Janet Rossant. FGF Signaling Regulates Mesoderm Cell Fate Specification and Morphogenetic Movement at the Primitive Streak. *Developmental Cell*, 1(1):37–49, 2001.

[162] Xuesong Yang, Dirk Dormann, Andrea E. Münsterberg, and Cornelis J. Weijer. Cell movement patterns during gastrulation in the chick are controlled by positive and negative chemotaxis mediated by FGF4 and FGF8. *Developmental Cell*, 3(3):425–437, 2002.

[163] Dirk Dormann and Cornelis J. Weijer. Chemotactic cell movement during development. *Current Opinion in Genetics and Development*, 13(4):358–364, 2003.

[164] Joao Firmino, Didier Rocancourt, Mehdi Saadaoui, Chloe Moreau, and Jerome Gros. Cell Division Drives Epithelial Cell Rearrangements during Gastrulation in Chick. *Developmental Cell*, 36(3):249–261, 2016.

[165] Claire Bertet, Lawrence Sulak, and Thomas Lecuit. Myosin-dependent junction remodelling controls planar cell intercalation and axis elongation. *Nature*, 429(6992):667–671, jun 2004.

[166] Manli Chuai and Cornelis J. Weijer. The Mechanisms Underlying Primitive Streak Formation in the Chick Embryo. In *Current Topics in Developmental Biology*, volume 81, pages 135–156. 2008.

[167] Joseph M. Laakso, John H. Lewis, Henry Shuman, and E. Michael Ostap. Myosin I can act as a molecular force sensor. *Science*, 321(5885):133–136, 2008.

[168] Emil Rozbicki, Manli Chuai, Antti I. Karjalainen, Feifei Song, Helen M. Sang, René Martin, Hans Joachim Knölker, Michael P. Macdonald, and Cornelis J. Weijer. Myosin-II-mediated cell shape changes and cell intercalation contribute to primitive streak formation. *Nature Cell Biology*, 17(4):397–408, 2015.

[169] Philipp J. Keller, Annette D. Schmidt, Joachim Wittbrodt, and Ernst H.K. Stelzer. Reconstruction of Zebrafish Early Embryonic Development by Scanned Light Sheet Microscopy. *Science*, 322(5904):1065–1069, nov 2008.

[170] Jan Huisken. Slicing embryos gently with laser light sheets. *BioEssays*, 34(5):406–411, 2012.

[171] V. Fleury. Can physics help to explain embryonic development? An overview. *Orthopaedics and Traumatology: Surgery and Research*, 99(6 SUPPL):S356–S365, 2013.

[172] Otger Campàs. A toolbox to explore the mechanics of living embryonic tissues. *Seminars in Cell & Developmental Biology*, 55(1):119–130, jul 2016.

[173] Nicolas R. Chevalier, Elodie Gazguez, Sylvie Dufour, and Vincent Fleury. Measuring the micromechanical properties of embryonic tissues. *Methods*, 94:120–128, 2016.

[174] Otger Campàs, Tadanori Mammoto, Sean Hasso, Ralph A. Sperling, Daniel O'connell, Ashley G. Bischof, Richard Maas, David A. Weitz, L. Mahadevan, and Donald E. Ingber. Quantifying cell-generated mechanical forces within living embryonic tissues. *Nature Methods*, 11(2):183–189, 2014.

[175] Shuji Ishihara and Kaoru Sugimura. Bayesian inference of force dynamics during morphogenesis. *Journal of Theoretical Biology*, 313:201–211, 2012.

[176] Itia A. Favre-Bulle, Daryl Preece, Timo A. Nieminen, Lucy A. Heap, Ethan K. Scott, and Halina Rubinsztein-Dunlop. Scattering of sculpted light in intact brain tissue, with implications for optogenetics. *Scientific Reports*, 5:1–9, 2015.

[177] Patrick Lie Johansen, Federico Fenaroli, Lasse Evensen, Gareth Griffiths, and Gerbrand Koster. Optical micromanipulation of nanoparticles and cells inside living zebrafish. *Nature Communications*, 7:1–8, 2016.

[178] Pierre-francois Lenne, Sylvie Dufour, and Atef Asnacios. Applying Optical Tweezers in Vivo : a Biophysical Study of Mechanical Forces in Drosophila Melanogaster. 2015.

[179] Raphaël Clément, Benoît Dehapiot, Claudio Collinet, Thomas Lecuit, and Pierre François Lenne. Viscoelastic Dissipation Stabilizes Cell Shape Changes during Tissue Morphogenesis. *Current Biology*, 27(20):3132–3142.e4, 2017.

[180] Susan C. Chapman, Jérôme Collignon, Gary C. Schoenwolf, and Andrew Lumsden. Improved method for chick whole-embryo culture using a filter paper carrier. *Developmental Dynamics*, 220(3):284–289, 2001.

[181] Shai Avidan and Ariel Shamir. Seam carving for content-aware image resizing. *ACM Transactions on Graphics*, 26(3):10, 2007.

[182] Eve Curie and Vincent Sheean. *Madame Curie: A Biography By Eve Curie (Illustrated)*. 1937.